

Máster en Matemática Industrial

Academic year 2019 – 2020

Master's thesis

Acoustic characterization of absorbing materials using dynamic mode decomposition techniques

Gonzalo Carazo Barbero

Defense date: 21 July 2020
Academic supervisor: Andrés Prieto
Company: ITMATI, Microflown Technologies
Company supervisor: Ashwin Nayak





Funded by the European Union's Horizon 2020 research and innovation programme under the Marie Skłodowska-Curie Grant Agreement No. 765374.

Contents

1	Introduction	1
2	Companies Involved	2
2.1	ITMATI	2
2.2	Microflown Technologies	2
2.3	ROMSOC	3
3	Preliminary Analysis	5
3.1	Motivation of the Physical Setting	5
3.2	Methods	6
3.3	Software	7
4	Models	9
4.1	Fluid Models	9
4.1.1	Fluid Model with Rigid Boundaries	9
4.1.2	Fluid Model with Rigid-Transparent Boundaries	10
4.2	Rigid Porous Models	11
4.2.1	Fluid-Porous Coupled Model with Rigid Boundaries	12
4.2.2	Fluid-Porous Coupled Model with Rigid-Transparent Boundaries	14
4.3	Poro-elastic Models	16
4.3.1	Umnova's Low Frequency Approximation on Porous Media	16
4.3.2	Umnova's Low Frequency Approximation on Fluid-Porous Coupled Media with Speaker-Rigid Boundaries	18
5	Discretization Algorithms	20
5.1	Finite Element Method	20
5.2	Newmark-Beta Method	23
6	Reduced Order Methods	25
6.1	Singular Value Decomposition	25
6.2	Dynamic Mode Decomposition	26
7	Validation	28
7.1	Error Control Through Space and Time Step Size	28
7.2	Exact Result Using d'Alembert's Solution	30
7.2.1	Fluid Model with Rigid Boundaries	30
7.2.2	Fluid Model with Rigid-Transparent Boundaries	30
7.3	Exact Result Using Harmonic Solution	31
7.3.1	Fluid Model with Rigid Boundaries	31
7.3.2	Fluid Model with Rigid-Transparent Boundaries	34
7.3.3	Fluid-Porous Coupled Model with Rigid Boundaries	35
7.3.4	Fluid-Porous Coupled Model with Rigid-Transparent Boundaries	36
7.4	Umnova's Low Frequency Approximation Comparison	38
8	Numerical Results	40
8.1	Harmonic Reconstruction	40
8.2	Harmonic Predictions	42
8.2.1	Effects of the Number of Snapshots Given	43
8.2.2	Effects of the Discretization Size	44
8.3	DMD vs. HODMD	47
8.4	Periodic Impulses	48

8.4.1	Effects of the DMD Rank	50
8.5	Non-Periodic Impulses	53
8.6	Simulation Mixing	55
8.7	Comparison to SVD	57
8.8	Shifted DMD	59

9	Conclusions	61
----------	--------------------	-----------

1 Introduction

In general, the simulation of physical phenomena through numerical methods tends to be a computationally intensive task, but this is particularly true in the field of acoustics. Due to the fast changing derivatives and the innately second order formulation, a fine mesh needs to be used, and in order for the time discretization to be well behaved, a small time step needs to be chosen as well. In addition to this, the testing of acoustic propagation in a single domain is rarely of interest, since most applications involve the design of acoustic barriers or transmitters, which means that most problems solved in the field involve couplings. One of the coupled mediums is usually a fluid, and it is common for the other to be a porous material since they are the most effective sound absorbers.

It is in fact because of this absorption that the porous models can get very complex. Time convolutions are usually needed for the modeling of high frequency noise, which makes the simulation process very costly. It becomes apparent that a reduced order method that is able to cut the computation time down is a worthwhile tool to have. Among the reduced order methods (ROMs) the chosen one is a method that is able to make predictions into the future from a reduced amount of snapshots.

Dynamic Mode Decomposition (DMD) is a technique developed in 2010 by Peter Schmid [47]. It is based on a Singular Value Decomposition (SVD) into which dynamics are added, making it able to not only reconstruct available data using a reduced order representation, but also able to expand the dimensionality in the time dimension in order to make predictions about the future. This means that a simulation spanning a shorter time can be run and the remaining sector of the time domain can be predicted by DMD, which adds up to a significantly faster process.

DMD is a data-driven method, which means that no information about the dynamic model is needed, only a series of snapshots are used. It has been used in the fluid dynamics community, where it originated, and a number of fields including video processing [21, 14], epidemiology [41] and neuroscience [5]. A number of acoustic models are developed in this work, and then, they are used to test the capabilities of DMD in acoustic problems and to find its limitations.

The motivation of this problem arises from a collaboration between the Technological Institute for Industrial Mathematics (ITMATI) and Microflown Technologies through the ROMSOC project. Together they started a project that became Ashwin Nayak's PhD thesis, in which the objective is to design a multilayer windshield for an acoustic probe by modeling the acoustic field both inside and outside of the windshield considering acoustic and other physical phenomena such as fluid, thermal and poro-elastic effects in an unbounded domain. The present master thesis project reduces Nayak's problem to a 1D simplified problem and attempts to develop a method that could be, in the future, generalized to his problem and reduce the computation time needed.

2 Companies Involved

Several companies are involved, directly or indirectly, in this project. Although the problem is posed solely by ITMATI, the motivations of this project lie on a PhD thesis that involves both ITMATI and Microflow Technologies in a partnership that came to fruition through the European ROMSOC project. For this reason, all three institutions will be presented.

2.1 ITMATI

The Technological Institute for Industrial Mathematics (ITMATI) [24] is an organization founded by the three public Galician universities, namely University of A Coruña (UDC), University of Santiago de Compostela (USC), and University of Vigo (UVigo). Its main goal is to further the research and development of mathematical technology applied to an industrial setting. In order to meet this goal it is frequent that ITMATI collaborates with companies in the production sector, often public companies. ITMATI is composed of 41 affiliated researchers associated to either of the three universities mentioned before, 7 collaborator researchers, and 23 people of their own staff, which includes 18 researchers, a manager, 4 technicians and an administrative assistant [25].

2.2 Microflow Technologies

Microflow Technologies [33] is a company founded in 1998 in University of Twente, in the Netherlands, by Hans-Elias de Bree and Alex Koers, and it was created after de Bree developed a particle velocity sensor in 1994. Microflow is a company that specializes in sensors and acoustic measuring devices based on MEMS (micro-electro-mechanical systems). They began their industrialization in 2001, and by 2003 they introduced the Microflow sensor, the first, and to date the only, sensor capable of measuring the velocity of an acoustic wave, since conventional microphones measure the fluid's pressure [32]. Combining these two types of sensors they created the first device able to measure both the velocity and the pressure of an acoustic wave, meaning that they are able to determine with ease and precision the source of a sound, and with the help of an auxiliary software, also provided by Microflow Technologies, create a 3D map of the sources and escape points of noise (Fig. 1). This allows for a more efficient acoustic confinement in applications such as motor vehicles and industrial processes.

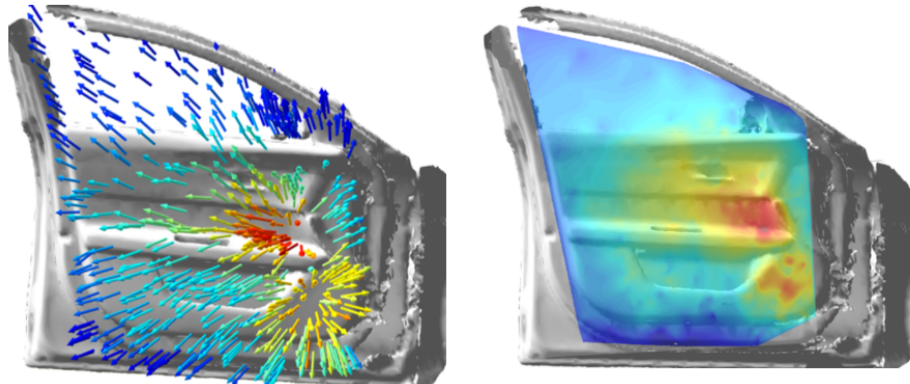


Figure 1: 3D map of the velocity and intensity of sound in a car door created by Scan&Paint 3D and Microflow sensors [33].

The sensor is composed of two very thin platinum strings, placed one next to the other (Fig. 2). First the strings are warmed by passing electrical current through them, and then, by measuring and comparing

the temperature from each of them, it is possible to determine the direction and even the velocity of the air surrounding them, and therefore, the acoustic wave's velocity. The temperature is measured by observing the change in electrical resistivity through the wire. It is possible to determine the particle (acoustic) velocity of the air by measuring the temperature of the wire, because when an air current passes through the first string it becomes colder as air takes part of the heat away. This means that by the time the air reaches the second wire, it is warmer and it is therefore unable to extract as much heat. This produces a gradient in temperature from one string to the next, which provides enough information to determine the air particle velocity [34].

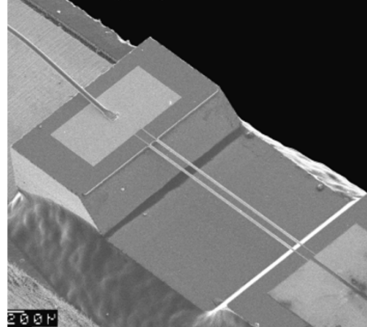


Figure 2: Microflown MEMS sensor [34].

As it can be expected from the explanation of the working principles, one of such sensors is only able to determine the particle velocity of the sound wave in one axis, so the probes that only include one of these plus a conventional microphone to measure pressure are known as Intensity Probes PU, while probes that include three Microflown sensors and a conventional microphone are able to determine the particle velocity in three-dimensional space and are known as Intensity Probes 3D or USP. Microflown Technologies also offers variants of these probes that only measure velocities (not pressures) or even custom solutions for particular applications.



Figure 3: Some of the probes produced by Microflown Technologies. From left to right: USP Regular, PU Regular, PU Mini y PU Voyager [34].

In following years they have developed other systems and software packages that complement their sensors, which include, for example, a sound localization software called Scan&Paint 3D, or contained measuring units such as Voyager.

2.3 ROMSOC

As mentioned in the introduction, this problem arises from the inclusion of ITMATI and Microflown Technologies in the ROMSOC project (Reduced Order Modeling, Simulation and Optimization of Coupled Systems) [46], which is a project funded by the European Commission that joins academic institutions such as ITMATI, and industrial companies such as Microflown Technologies. Its main goal is very in line with that of ITMATI, which consists in supporting the industry from a mathematical perspective, but as

a difference, ROMSOC chooses to do so in particular through reduced order methods applied to coupled systems.

The project spans four years and joins 15 academic institutions and 11 companies in the PhD thesis of 11 early stage researchers. The challenges taken upon are multidisciplinary in nature and international. They promote the collaboration between involved sectors, among other things, by making the researchers divide their working time equally in academic institutions and industrial companies.

3 Preliminary Analysis

In this chapter the motivations that lead the development of this project will be explored, as well as the approach taken when solving it and the tools used in order to achieve this.

3.1 Motivation of the Physical Setting

Since this project sprouts from Ashwin Nayak's PhD thesis (currently, a work in progress), an introduction to his project will open this section. The Microflown sensor is based on MEMS technology, which means that the magnitudes used, for example measuring the change in resistance in the wires, are very small and any perturbation is able to alter the measurement. It is therefore important that only the signal that needs to be measured reaches the sensor. The exposure to winds and natural air currents would change the temperature in the wire, and the system would interpret it as a sound wave even though it is not. For this reason, Ashwin Nayak was tasked with the design of a multilayer windshield that ensures accurate readings. He will need to model the acoustic field both inside and outside the windshield and couple in the problem other physical phenomena such as fluid, thermal and poro-elastic effects in an unbounded domain.

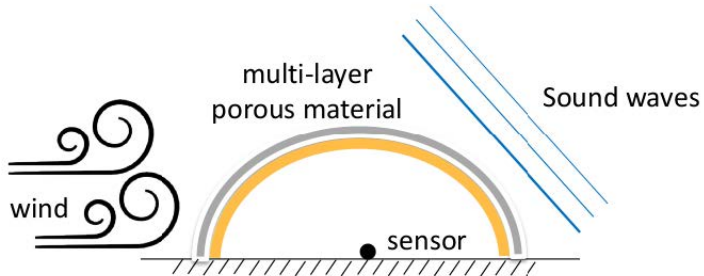


Figure 4: Schematic diagram of Nayak's PhD proposal.

The goal of the present master project is to explore the use of a reduced order model (ROM) that is able to simulate a fluid-porous media coupling that can be later applied to more sophisticated models involving airflow. However, due to the complexity of the original problem of interest, a one-dimensional variant of the coupled problem without flow will be implemented. With the objective of making the project more useful and applicable, and as a way to justify the dimensionality chosen, the simulation of an impedance-Kundt tube was proposed, which is able to test different materials through a parametric sweep of the material's properties. This allows to find an adequate material for the windshield, as well as providing an accurate and fast model that could be generalized to three-dimensional scenarios.

Experimentally, an impedance-Kundt tube can be used in a number of different physical configurations and using several measuring techniques. All measurements are performed on the fluid domain, since including a microphone in the test sample would disrupt the measurement. Conventionally, two microphones are used, one is used as a reference and the other is used to actually record the wave [8, 9]. This was necessary since at least two measuring points are needed in order to record the wave (acoustic) velocity with pressure microphones. However, using the Microflown sensor, a single probe can be used in order to extract the same information [53]. Yet another option available, is to mount the microphone on a moving structure, so that the same microphone is able to take measurements at any point along the tube [16, 48]. This last technique is typically used in experiments dealing with standing waves.

The objective of the different placements is to get quality reading in different situations, and from them being able to determine the acoustic characteristics of the test sample. However, the project is focused on running a numerical simulation, so no microphones are needed since all the measurements are available in the entire domain, even within the sample without having to deal with the risk of spoiling the experiment due to a bad microphone placement or by disrupting the wave. The measuring techniques illustrated in

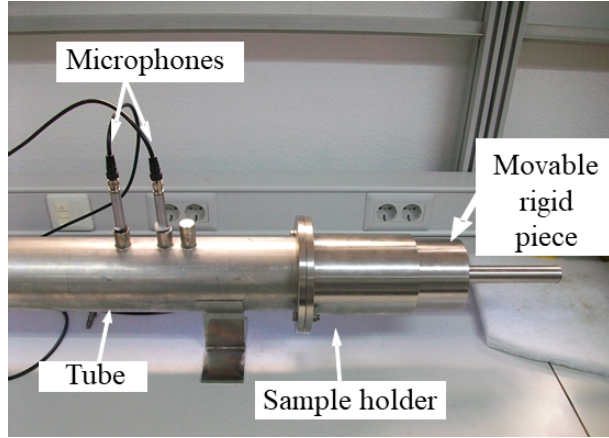


Figure 5: Example of an impedance-Kundt tube [6].

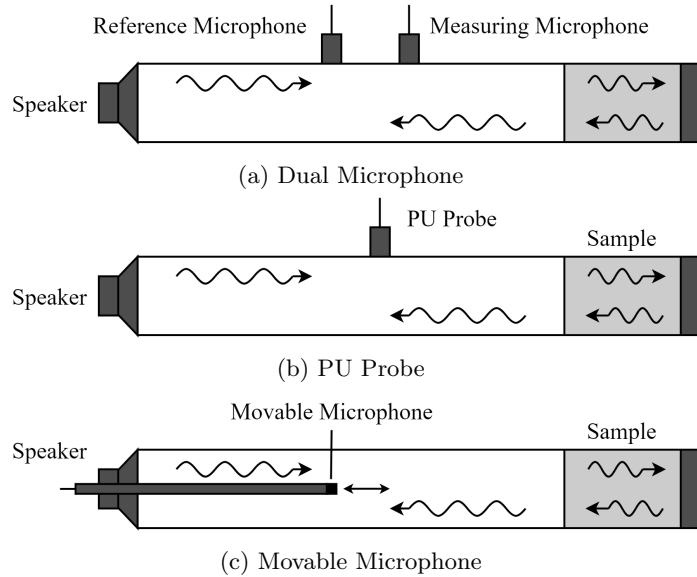


Figure 6: Experimental measuring techniques in an impedance-Kundt tube.

Fig. 6 all use the same physical configuration, where a rigid plate closes the tube at the rightmost edge and the sample is placed against it. Another configuration was used in this project too, one that is also commonly used experimentally. This second configuration does not include the backing rigid plate and instead the end of the tube is left open for waves to be radiated.

3.2 Methods

The project is divided in three phases: a) implementation of a 1D model with fluid-porous media coupling, using linear models in the temporal domain; b) implementation of a ROM in order to reduce the computational cost of solving the model developed in the previous phase; and c) analysis and testing of material acoustic properties using different physical configurations.

It is common in acoustic problems to study the frequency domain since this simplifies greatly the complexity of the equations used and ensures the model behaves properly during the resolution process. However, such models fall short in that they are unable to reliably predict the acoustic transmission

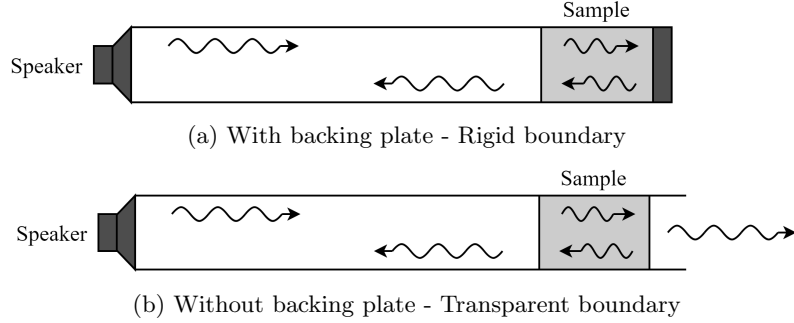


Figure 7: Physical configurations used for the impedance-Kundt tube.

when short-duration impulse responses are needed, since frequency models rely on the wave's periodicity to make predictions, while a short-duration impulse lacks any kind of periodicity.

This problem is commonplace in the industry, specially when modeling collisions, sudden changes in pressure (such as hydraulic shock in pipes) or the ultrasound pulses that are used for material testing. To get around the limitations, normally a fluid-equivalent model is used, which provides a linear model that is capable of correctly predicting short-duration impulses and at the same time providing good approximations for the acoustic impedance of the material in a wide range of frequencies. This is important because the Microflown sensor is able to capture signals ranging 20 Hz to 10 kHz [34]. Once complete, this model lays the foundation for the next phases, which focus on improving the efficiency and maintaining the quality of the solution and the testing of materials. It also represents a good addition to the ROMSOC project.

The biggest drawback of an acoustic model in the time domain, and specially of those that include a porous media, is that in order to get proper results at high frequencies it is necessary to implement convolutions in time for each element of the PDE, which results in a great amount of computation time needed. It is therefore of utmost importance to reduce the computation time to be practical, also aiming not to sacrifice too much accuracy in the process. This is possible through the use of ROMs. In particular Dynamic Mode Decomposition (DMD) [47] is selected because, unlike other methods such as principal component analysis (PCA) [27], this is a method that is intrinsically temporal and tends to reduce the computation time greatly keeping the accuracy.

In the last phase of the project, which is again based upon previous work, the models and methods developed are used to test different porous materials in different physical configurations. Since the goal of the project is to find a material that can be used at some point in production, in any other case only standardized materials would be tested. However in this case porous materials such as foams are being used, and in practice, the production of such materials can be adjusted and designed to meet the specific criteria needed. This can be done by modifying the rate at which the filler gas is injected, changing the temperature profile, the base material or even through the introduction of impurities that change the physical behavior of the foam. For this reason it is reasonable to justify a parametric sweep with a low computational cost (using ROMs), which provides the parameters of a perfect material, and from this result in production it will be possible to manufacture the ideal windshield making no sacrifices.

3.3 Software

The implementation of the models and algorithms have been coded in Python using two different packages to make the implementation more straightforward. FEniCS package was used for the finite element method, and PyDMD, another Python library, was used to implement the DMD method.

FEniCS Project [17] is an open source package specially designed for the resolution of PDEs. It allows for an easy transition between the mathematical model (in particular the variational formulation of the model) and the algorithm. It provides interfaces both in Python and C++, but the first one is used since

it is better aligned with the project’s objectives and the rest of the tools used. Its Python implementation was chosen in particular because this language provides a more superficial and generalized approach than the alternative, so it is easier to use.

PyDMD [13] is another open source Python package. It is an implementation of the DMD method that, given a few snapshots of a solution, is able to reconstruct the solution in the range given and even extrapolate further in time. Since the main DMD method was first introduced in 2010 [47] many variants of the method have been developed. Each of the variants expand the capabilities of the DMD in a certain way. For instance, multiresolution dynamic mode decomposition (mrDMD) [28] allows for the decomposition of the system by the integration of different time-scale components. Or higher order dynamic mode decomposition (HODMD) [30], which allows its use in problems with a great amount of modes at different frequencies. PyDMD includes many of these variants, including the two already mentioned, compressed dynamic mode decomposition (cDMD) [15], forward-backward dynamic mode decomposition (fbDMD) [12], and dynamic mode decomposition with control (DMDc) [40]. In particular, the standard version of DMD was used, as well as HODMD.

Another Python library was briefly employed in order to implement SVD. In particular, TruncatedSVD from the `sklearn.decomposition` package from scikit-learn was used [49]. Other supporting software was used, but it was not critical to the success of the project. It includes software such as ParaView, which allowed for the visualization of the approximated discrete solutions and their troubleshooting, Docker, in order to run the code in a Windows machine, and even MATLAB in a very limited way.

4 Models

In the course of this project a number of models of increasing complexity have been developed. The step-wise progress from one model to the next has allowed to slowly build upon previous findings and to perform tests in order to make sure that each step was not misguided. Because of this, the simplest possible model available for acoustic waves in the time domain was the first: the wave equation where both boundaries are rigid. Then, one of the boundaries was made transparent in order to be able to simulate the impedance tube in its open configuration. Later, part of the domain was changed to a very simple model of a rigid porous media, since the main goal of impedance tubes is to measure the acoustic characteristics of such materials. Until then all models relied on the initial conditions in order to have perturbations, so the next step was to add a speaker in the closed end. Taking the speaker into account, it was possible to simulate regular simple experiments as performed in the laboratory. The final step was to take this model one step further and improve on the complexity of the porous model. To this end, the final porous model was based on the fluid-equivalent model developed by Umnova [52]. In the following pages a description of each model is developed on detail. All the time-dependent mathematical models described above will be stated in a bounded time interval $[0, T]$, where T is a positive constant. This time interval will contain all the transient phenomena of interest.

4.1 Fluid Models

In this section only the models in which the only domain is fluid will be included. They are the simplest and they served as a starting point in the development of the rest. By themselves, they are not very useful, since in practice no experiment would be done on an empty impedance tube, but they allow to perform some tests (which will be discussed in the validation chapter) that show that the model is correct and properly working. They also serve as a stepping stone for the models to come.

4.1.1 Fluid Model with Rigid Boundaries

As it has been discussed, the first model developed was the simplest. Physically, this model is able to simulate the wave dynamics inside a Kundt tube where both ends are closed and no test material is placed inside. The evolution is also passive, since no speaker is included, so only the perturbations present at the initial time can influence the behavior of the wave.

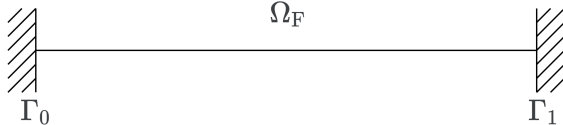


Figure 8: Diagram of the fluid model with rigid boundaries.

A fluid domain is defined within two rigid boundaries, as shown in Fig. 8. The domain equation is the standard wave equation, whereas the boundaries are null Dirichlet conditions. Precisely, because of this reason no signal dependent on time has been introduced, and therefore the simulation has to rely on the initial conditions to introduce perturbations in the system. A formulation on displacements has been chosen, although, as it can be observed in the described models written below, the transformation from displacements to pressures and velocities is relatively straightforward, even in the most complex models used here. In the first case, the differential model is given by

$$\begin{cases} \rho_f \partial_t^2 u_f - \rho_f c_f^2 \partial_x^2 u_f = f & \text{in } (0, T) \times \Omega_f, \\ u_f = 0 & \text{on } (0, T) \times (\Gamma_0 \cup \Gamma_1), \end{cases} \quad (\mathcal{P}_1')$$

where u_f is the displacement in the fluid media, ρ_f the density of the fluid, c_f the speed of sound in the fluid and f is any external force that acts upon the wave, although it was never used in simulations. For

the application of the finite element method, it is required to write its variational form. Taking the first equation, multiplying it by test function $w \in H_0^1(\Omega_f)$, and integrating it in the domain,

$$\int_{\Omega_f} \rho_f \partial_t^2 u_f \cdot w \, dx - \int_{\Omega_f} \rho_f c_f^2 \partial_x^2 u_f \cdot w \, dx = \int_{\Omega_f} f \cdot w \, dx. \quad (1)$$

After integrating the second term by parts, it holds

$$\int_{\Omega_f} \rho_f \partial_t^2 u_f \cdot w \, dx - (\rho_f c_f^2 \partial_x u_f \cdot w|_{\Gamma_1} + (\rho_f c_f^2 \partial_x u_f \cdot w|_{\Gamma_0} + \int_{\Omega_f} \rho_f c_f^2 \partial_x u_f \cdot \partial_x w \, dx = \int_{\Omega_f} f \cdot w \, dx, \quad (2)$$

and then, substituting the second equation in (P'_1) in the second and third terms, the following variational formulation is obtained: Given a source term $f \in C([0, T], L^2(\Omega_f))$ and the initial conditions for the displacement and the velocity fields, u_f^0 and v_f^0 in $H_0^1(\Omega_f)$ respectively, find $u_f \in C^2((0, T), L^2(\Omega_f)) \cap C^1([0, T], H_0^1(\Omega_f))$ such that $u_f(0, \cdot) = u_f^0$, $\partial_t u_f(0, \cdot) = v_f^0$, and it holds

$$\int_{\Omega_f} \rho_f \partial_t^2 u_f \cdot w \, dx + \int_{\Omega_f} \rho_f c_f^2 \partial_x u_f \cdot \partial_x w \, dx = \int_{\Omega_f} f \cdot w \, dx. \quad (V_1)$$

for all $w \in H_0^1(\Omega_f)$.

In general, for the numerical method of time integration that will be used, which will be described further on, there is a need to obtain a variational formulation with four parts: a mass term, which is dependent on $\partial_t^2 u_f$, a damping term, which is dependent on $\partial_t u_f$, a stiffness term, dependent on u_f directly, and finally an external force term, not dependent on u_f at all. As shown, in this model it is possible to find a mass term, the first, a stiffness term, the second, and an external forces term, the last. This is to show that some of the terms can in fact be empty.



Figure 9: Diagram of the fluid model with speaker-rigid boundaries.

Seeking a more general model a speaker in one of the boundaries was introduced (see Fig. 9). This only has the effect of changing one of the Dirichlet conditions from a null condition to a time-dependent condition:

$$\begin{cases} \rho_f \partial_t^2 u_f - \rho_f c_f^2 \partial_x^2 u_f = f & \text{in } (0, T) \times \Omega_f, \\ u_f = g & \text{on } (0, T) \times \Gamma_0, \\ u_f = 0 & \text{on } (0, T) \times \Gamma_1, \end{cases} \quad (P_1)$$

where $g \in C(0, T)$ is a time-dependent function representing the displacement at the boundary point Γ_0 . Since the term on Γ_0 in (2) only includes $\partial_x u_f$, and in this case $u_f|_{\Gamma_0}$ is only dependent on time, the variational form of (P_1) is identical to (V_1) , except that in this case, u_f^0 and v_f^0 in $H^1(\Omega_f)$ (which satisfy the boundary conditions), $u_f \in C^2((0, T), L^2(\Omega_f)) \cap C^1([0, T], H^1(\Omega_f))$ (satisfying the Dirichlet boundary conditions), and $w \in H_{\Gamma_1}^1(\Omega_f)$.

4.1.2 Fluid Model with Rigid-Transparent Boundaries

The following step is to develop an extremely simple model for the other physical configuration of an impedance-Kundt tube, where one of the ends is open. Still, no test material is placed inside, so the domain of the model remains entirely fluid and the wave equation is still used. The only change with

respect to the previous model is that one of the Dirichlet conditions, in particular the one on the right boundary, is changed to a transparent Sommerfeld condition.

$$\begin{cases} \rho_f \partial_t^2 u_f - \rho_f c_f^2 \partial_x^2 u_f = f & \text{in } (0, T) \times \Omega_f, \\ u_f = 0 & \text{on } (0, T) \times \Gamma_0, \\ \partial_t u_f + c_f \partial_x u_f = 0 & \text{on } (0, T) \times \Gamma_1. \end{cases} \quad (\mathcal{P}'_2)$$



Figure 10: Diagram of the fluid model with rigid-transparent boundaries.

In the same fashion as before a transformation from the strong form into its variational form can be performed, although this time $w \in H_{\Gamma_0}^1(\Omega_f) = \{s \in H^1(\Omega_f) : s|_{\Gamma_0} = 0\}$ since the boundary must be able to move freely. It is to be noted that an additional term has appeared. This is precisely due to the need to let the wave pass through the transparent boundary, which forces $\partial_t u_f$ not to be zero on Γ_1 . The new term forms in this case the damping part of the equation. The variational formulation is: Given a source term $f \in C([0, T], L^2(\Omega_f))$ and the initial conditions for the displacement and the velocity fields, u_f^0 and v_f^0 in $H_{\Gamma_0}^1(\Omega_f)$ respectively, find $u_f \in C^2((0, T), L^2(\Omega_f)) \cap C^1([0, T], H_{\Gamma_0}^1(\Omega_f))$ such that $u_f(0, \cdot) = u_f^0$, $\partial_t u_f(0, \cdot) = v_f^0$, and it holds

$$\int_{\Omega_f} \rho_f \partial_t^2 u_f \cdot w \, dx + (\rho_f c_f \partial_t u_f)|_{\Gamma_1} + \int_{\Omega_f} \rho_f c_f^2 \partial_x u_f \cdot \partial_x w \, dx = \int_{\Omega_f} f \cdot w \, dx, \quad (\mathcal{V}_2)$$

for all $w \in H_{\Gamma_0}^1(\Omega_f)$.

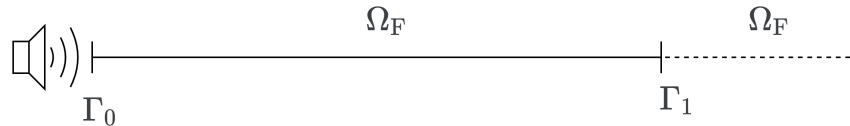


Figure 11: Diagram of the fluid model with speaker-transparent boundaries.

As before, a variant of this model using a speaker in the left boundary (Fig. 11) can be described as

$$\begin{cases} \rho_f \partial_t^2 u_f - \rho_f c_f^2 \partial_x^2 u_f = f & \text{in } (0, T) \times \Omega_f, \\ u_f = g & \text{on } (0, T) \times \Gamma_0, \\ \partial_t u_f + c_f \partial_x u_f = 0 & \text{on } (0, T) \times \Gamma_1. \end{cases} \quad (\mathcal{P}_2)$$

For the same reason as before, and including the same modifications to the functional spaces, the variational formulation of this model corresponds to (\mathcal{V}_2) .

4.2 Rigid Porous Models

In this section all the models that make use of a rigid porous model are grouped. This is the simplest kind of porous media, so there are no thermal or viscous effects, but they can be useful in certain cases. Even having a coupling between the porous media and the fluid media it is still possible to obtain some exact solutions to validate them, so more complex models to come can be reliably based upon these.

4.2.1 Fluid-Porous Coupled Model with Rigid Boundaries

Having developed models for the two different physical configurations of the impedance tube, the next logical step is to start including porous media in the domain. At first, a simple rigid porous model is used. Although more accurate models exist for poro-elastic materials, it also has its benefits. For one, it is much faster to compute, specially given high-frequency signals, and it provides a baseline onto which more complex models can be built. The first step, as before, is having two rigid boundaries, since this is the simplest of the two. For this reason, the Dirichlet conditions are re-established at both ends. Now the domain is split in two parts. Since the speaker, which will be included later, needs to be placed at the opposite end than the open limit, and the right boundary was made transparent, the speaker will be placed on the left. This means that the fluid domain must occupy this position, leaving the porous domain at the right side. An interface boundary between the two media appears, so a coupling is needed in this model:

$$\begin{cases} \rho_f \partial_t^2 u_f - \rho_f c_f^2 \partial_x^2 u_f = f & \text{in } (0, T) \times \Omega_f, \\ \rho_p \partial_t^2 u_p - \frac{\rho_p c_p^2}{\phi \gamma_p} \partial_x^2 u_p + \sigma \partial_t u_p = 0 & \text{in } (0, T) \times \Omega_p, \\ u_f = \phi u_p & \text{on } (0, T) \times \Gamma, \\ \rho_f c_f^2 \partial_x u_f = \frac{\rho_p c_p^2}{\phi \gamma_p} \partial_x u_p & \text{on } (0, T) \times \Gamma, \\ u_f = 0 & \text{on } (0, T) \times \Gamma_0, \\ u_p = 0 & \text{on } (0, T) \times \Gamma_1, \end{cases} \quad (\mathcal{P}'_3)$$

where, in addition to the variables defined before, u_p is the displacement in the porous media, ρ_p is the density of the porous material, c_p is the speed of sound in the porous media, ϕ is the porosity as the fraction of the volume of voids over the total volume, γ is the adiabatic index as the ratio of the heat capacity at constant pressure over the heat capacity at constant volume, and σ is the flux resistivity tensor (in this case a scalar due to the dimensionality of the problem).

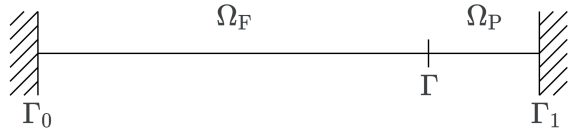


Figure 12: Diagram of the fluid-porous coupled model with rigid-rigid boundaries.

Since in the implementation only one displacement variable will be accepted, the following definition is needed:

$$\tilde{u}_p = \phi u_p \implies u_f = \tilde{u}_p \quad \text{on } (0, T) \times \Gamma. \quad (3)$$

This makes the displacement variable continuous in the entire domain, which later on will allow choosing a continuous test function. Substituting $u_p = \tilde{u}_p/\phi$ in (\mathcal{P}'_3) , a model dependent on a single continuous displacement is obtained:

$$\begin{cases} \rho_f \partial_t^2 u_f - \rho_f c_f^2 \partial_x^2 u_f = f & \text{in } (0, T) \times \Omega_f, \\ \frac{\rho_p}{\phi} \partial_t^2 \tilde{u}_p - \frac{\rho_p c_p^2}{\phi^2 \gamma_p} \partial_x^2 \tilde{u}_p + \frac{\sigma}{\phi} \partial_t \tilde{u}_p = 0 & \text{in } (0, T) \times \Omega_p, \\ u_f = \tilde{u}_p & \text{on } (0, T) \times \Gamma, \\ \rho_f c_f^2 \partial_x u_f = \frac{\rho_p c_p^2}{\phi^2 \gamma_p} \partial_x \tilde{u}_p & \text{on } (0, T) \times \Gamma, \\ u_f = 0 & \text{on } (0, T) \times \Gamma_0, \\ \tilde{u}_p = 0 & \text{on } (0, T) \times \Gamma_1. \end{cases} \quad (\mathcal{P}''_3)$$

In order to transform this formulation to the variational form, it is possible to multiply the first equation in (\mathcal{P}_3'') by a test function w in $H_0^1(\Omega)$, where Ω is the interior of $\overline{\Omega_f} \cup \overline{\Omega_p}$, and integrate over the fluid domain to get

$$\int_{\Omega_f} \rho_f \partial_t^2 u_f \cdot w \, dx - \int_{\Omega_f} \rho_f c_f^2 \partial_x^2 u_f \cdot w \, dx = \int_{\Omega_f} f \cdot w \, dx. \quad (4)$$

Integrating the second term by parts and substituting the fourth and fifth equations in (\mathcal{P}_3'') ,

$$\int_{\Omega_f} \rho_f \partial_t^2 u_f \cdot w \, dx - \left(\frac{\rho_p c_p^2}{\phi^2 \gamma_p} \partial_x \tilde{u}_p \cdot w \right)_{\Gamma} + \int_{\Omega_f} \rho_f c_f^2 \partial_x u_f \cdot \partial_x w \, dx = \int_{\Omega_f} f \cdot w \, dx. \quad (5)$$

Turning now to the porous media equation. Multiplying the second equation in (\mathcal{P}_3'') by test function w and integrating over the porous domain,

$$\int_{\Omega_p} \frac{\rho_p}{\phi} \partial_t^2 \tilde{u}_p \cdot w \, dx - \int_{\Omega_p} \frac{\rho_p c_p^2}{\phi^2 \gamma_p} \partial_x^2 \tilde{u}_p \cdot w \, dx + \int_{\Omega_p} \frac{\sigma}{\phi} \partial_t \tilde{u}_p \cdot w \, dx = 0. \quad (6)$$

Integrate by parts the second term and apply the sixth equation in (\mathcal{P}_3'') ,

$$\int_{\Omega_p} \frac{\rho_p}{\phi} \partial_t^2 \tilde{u}_p \cdot w \, dx + \left(\frac{\rho_p c_p^2}{\phi^2 \gamma_p} \partial_x \tilde{u}_p \cdot w \right)_{\Gamma} - \int_{\Omega_p} \frac{\rho_p c_p^2}{\phi^2 \gamma_p} \partial_x \tilde{u}_p \cdot \partial_x w \, dx + \int_{\Omega_p} \frac{\sigma}{\phi} \partial_t \tilde{u}_p \cdot w \, dx = 0. \quad (7)$$

Adding (5) and (7) together, the terms on Γ can be canceled out and the variational formulation is reached, which will be used in the implementation: Given a source term $f \in \mathcal{C}([0, T], L^2(\Omega_f))$ and the initial conditions for the displacement and the velocity fields, u_f^0 and v_f^0 in $H_{\Gamma_0}^1(\Omega_f)$, and u_p^0 and v_p^0 in $H_{\Gamma_1}^1(\Omega_p)$ respectively (and satisfying the coupling conditions $u_f^0 = u_p^0$ and $v_f^0 = v_p^0$), find $u_f \in \mathcal{C}^2((0, T), L^2(\Omega_f)) \cap \mathcal{C}^1([0, T], H_{\Gamma_0}^1(\Omega_f))$ and $\tilde{u}_p \in \mathcal{C}^2((0, T), L^2(\Omega_p)) \cap \mathcal{C}^1([0, T], H_{\Gamma_1}^1(\Omega_p))$ such that $u_f = \tilde{u}_p$ on $(0, T) \times \Gamma$, $u_f(0, \cdot) = u_f^0$, $\partial_t u_f(0, \cdot) = v_f^0$, $\tilde{u}_p(0, \cdot) = u_p^0$, $\partial_t \tilde{u}_p(0, \cdot) = v_p^0$, and it holds

$$\begin{aligned} & \int_{\Omega_f} \rho_f \partial_t^2 u_f \cdot w \, dx + \int_{\Omega_p} \frac{\rho_p}{\phi} \partial_t^2 \tilde{u}_p \cdot w \, dx + \int_{\Omega_p} \frac{\sigma}{\phi} \partial_t \tilde{u}_p \cdot w \, dx \\ & + \int_{\Omega_f} \rho_f c_f^2 \partial_x u_f \cdot \partial_x w \, dx + \int_{\Omega_p} \frac{\rho_p c_p^2}{\phi^2 \gamma_p} \partial_x \tilde{u}_p \cdot \partial_x w \, dx = \int_{\Omega_f} f \cdot w \, dx, \end{aligned} \quad (\mathcal{V}_3)$$

for all $w \in H_0^1(\Omega)$. In this case, the first two terms constitute the mass part, the third term is the damping part, the fourth and fifth are the stiffness terms and the last is the external forces term. As shown here the effects of the coupling are implied in the domain terms, and since both external boundaries are rigid, no boundary term appears.

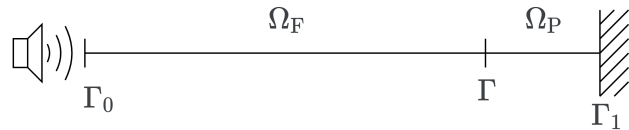


Figure 13: Diagram of the fluid-porous coupled model with speaker-rigid boundaries.

As before, a more general version of this model is introduced when the speaker is included (see Fig. 13):

$$\begin{cases} \rho_f \partial_t^2 u_f - \rho_f c_f^2 \partial_x^2 u_f = f & \text{in } (0, T) \times \Omega_f, \\ \rho_p \partial_t^2 u_p - \frac{\rho_p c_p^2}{\phi \gamma_p} \partial_x^2 u_p + \sigma \partial_t u_p = 0 & \text{in } (0, T) \times \Omega_p, \\ u_f = \phi u_p & \text{on } (0, T) \times \Gamma, \\ \rho_f c_f^2 \partial_x u_f = \frac{\rho_p c_p^2}{\phi \gamma_p} \partial_x u_p & \text{on } (0, T) \times \Gamma, \\ u_f = g & \text{on } (0, T) \times \Gamma_0, \\ u_p = 0 & \text{on } (0, T) \times \Gamma_1. \end{cases} \quad (\mathcal{P}_3)$$

Again, the integral terms of the variational formulation are unchanged by the introduction of the speaker, except that in this case, the solution should satisfy $u_f = g$ on $(0, T) \times \Gamma_0$ and the initial conditions in the fluid domain should be compatible with this boundary condition, this is, $u_f^0 = g(0)$ and $v_f^0 = g'(0)$ on Γ_0 .

4.2.2 Fluid-Porous Coupled Model with Rigid-Transparent Boundaries

The next step is to develop a model in which a porous media is included and one of the ends of the tube is open. On the open right end of the tube the Dirichlet boundary condition from the previous model is substituted, but the condition must not be perfectly transparent like in the fluid case. In spite of the modeling domain ending at the end of the porous domain it is important to consider what comes beyond, since the condition there is clearly not rigid. When performing an experiment with the objective of characterizing the acoustic properties of a porous material, a sample of the material is placed at the end of the tube, and beyond the limit, it is open to the fluid again. For this reason the fluid domain beyond the boundary Γ_1 is extended (see Fig. 14).



Figure 14: Diagram of the fluid-porous coupled model with rigid-transparent boundaries.

In the boundary between two media, two acoustic phenomena occur. The incoming wave is both reflected back to the original media and also refracted into the new one. After this process the energy of each of the rays is less than that of the original wave. This happens on the interface Γ , and like so, the coupling equations are added to the system like in the previous model, but it also happens in the new coupled boundary created at the end of the tube. For this reason, this model has two coupled boundaries, one interior coupled boundary in Γ and one exterior coupled boundary in Γ_1 :

$$\begin{cases} \rho_f \partial_t^2 u_f - \rho_f c_f^2 \partial_x^2 u_f = f & \text{in } (0, T) \times \Omega_f, \\ \rho_p \partial_t^2 u_p - \frac{\rho_p c_p^2}{\phi \gamma_p} \partial_x^2 u_p + \sigma \partial_t u_p = 0 & \text{in } (0, T) \times \Omega_p, \\ u_f = \phi u_p & \text{on } (0, T) \times \Gamma, \\ \rho_f c_f^2 \partial_x u_f = \frac{\rho_p c_p^2}{\phi \gamma_p} \partial_x u_p & \text{on } (0, T) \times \Gamma, \\ u_f = 0 & \text{on } (0, T) \times \Gamma_0, \\ u_f = \phi u_p & \text{on } (0, T) \times \Gamma_1, \\ \rho_f c_f^2 \partial_x u_f = \frac{\rho_p c_p^2}{\phi \gamma_p} \partial_x u_p & \text{on } (0, T) \times \Gamma_1, \\ \partial_t u_f + c_f \partial_x u_f = 0 & \text{on } (0, T) \times \Gamma_1. \end{cases} \quad (8)$$

The three equations on Γ_1 can be combined in order to simplify the model. Consider the three equations on Γ_1 .

$$\begin{cases} u_f = \phi u_p & \text{on } (0, T) \times \Gamma_1, \\ \rho_f c_f^2 \partial_x u_f = \frac{\rho_p c_p^2}{\phi \gamma_p} \partial_x u_p & \text{on } (0, T) \times \Gamma_1, \\ \partial_t u_f + c_f \partial_x u_f = 0 & \text{on } (0, T) \times \Gamma_1. \end{cases} \quad (9)$$

Differentiating the first and rearranging the second,

$$\begin{cases} \partial_t u_f = \phi \partial_t u_p & \text{on } (0, T) \times \Gamma_1, \\ \partial_x u_f = \frac{\rho_p c_p^2}{\rho_f c_f^2 \phi \gamma_p} \partial_x u_p & \text{on } (0, T) \times \Gamma_1, \\ \partial_t u_f + c_f \partial_x u_f = 0 & \text{on } (0, T) \times \Gamma_1, \end{cases} \quad (10)$$

which can then be substituted in the third:

$$\phi \partial_t u_p + \frac{\rho_p c_p^2}{\rho_f c_f \phi \gamma_p} \partial_x u_p = 0 \quad \text{on } (0, T) \times \Gamma_1. \quad (11)$$

Substituting the three original equations with (11) yields the following differential model:

$$\begin{cases} \rho_f \partial_t^2 u_f - \rho_f c_f^2 \partial_x^2 u_f = f & \text{in } (0, T) \times \Omega_f, \\ \rho_p \partial_t^2 u_p - \frac{\rho_p c_p^2}{\phi \gamma_p} \partial_x^2 u_p + \sigma \partial_t u_p = 0 & \text{in } (0, T) \times \Omega_p, \\ u_f = \phi u_p & \text{on } (0, T) \times \Gamma, \\ \rho_f c_f^2 \partial_x u_f = \frac{\rho_p c_p^2}{\phi \gamma_p} \partial_x u_p & \text{on } (0, T) \times \Gamma, \\ u_f = 0 & \text{on } (0, T) \times \Gamma_0, \\ \phi \partial_t u_p + \frac{\rho_p c_p^2}{\rho_f c_f \phi \gamma_p} \partial_x u_p = 0 & \text{on } (0, T) \times \Gamma_1. \end{cases} \quad (\mathcal{P}'_4)$$

In a similar fashion to model (\mathcal{P}'_3) , a derivation of its variational formulation is straightforward. However, in the process of substituting the transparent boundary condition an additional term that was canceled before emerges. The variational formulation is the following: Given a source term $f \in \mathcal{C}([0, T], L^2(\Omega_f))$ and the initial conditions for the displacement and the velocity fields, u_f^0 and v_p^0 in $H_{\Gamma_0}^1(\Omega_f)$, and u_p^0 and v_p^0 in $H^1(\Omega_p)$ respectively (and satisfying the coupling conditions $u_f^0 = u_p^0$ and $v_f^0 = v_p^0$), find $u_f \in \mathcal{C}^2((0, T), L^2(\Omega_f)) \cap \mathcal{C}^1([0, T], H_{\Gamma_0}^1(\Omega_f))$ and $\tilde{u}_p \in \mathcal{C}^2((0, T), L^2(\Omega_p)) \cap \mathcal{C}^1([0, T], H^1(\Omega_p))$ such that $u_f = \tilde{u}_p$ on $(0, T) \times \Gamma$, $u_f(0, \cdot) = u_f^0$, $\partial_t u_f(0, \cdot) = v_f^0$, $\tilde{u}_p(0, \cdot) = u_p^0$, $\partial_t \tilde{u}_p(0, \cdot) = v_p^0$, and it holds

$$\begin{aligned} & \int_{\Omega_f} \rho_f \partial_t^2 u_f \cdot w \, dx + \int_{\Omega_p} \frac{\rho_p}{\phi} \partial_t^2 \tilde{u}_p \cdot w \, dx + \int_{\Omega_p} \frac{\sigma}{\phi} \partial_t \tilde{u}_p \cdot w \, dx + (\rho_f c_f \partial_t \tilde{u}_p \cdot w|_{\Gamma_1} \\ & + \int_{\Omega_f} \rho_f c_f^2 \partial_x u_f \cdot \partial_x w \, dx + \int_{\Omega_p} \frac{\rho_p c_p^2}{\phi^2 \gamma_p} \partial_x \tilde{u}_p \cdot \partial_x w \, dx = \int_{\Omega_f} f \cdot w \, dx. \end{aligned} \quad (\mathcal{V}_4)$$

for all $w \in H^1(\Omega)$. Here it is shown that the additional term is added to the damping part, the fourth term. Finally, the speaker is included to get a more general model (see Fig. 15). As before, the Dirichlet boundary condition on the left is changed but the integral terms of the variational formulation remains identical to (\mathcal{V}_4) .



Figure 15: Diagram of the fluid-porous coupled model with speaker-transparent boundaries.

$$\begin{cases} \rho_f \partial_t^2 u_f - \rho_f c_f^2 \partial_x^2 u_f = f & \text{in } (0, T) \times \Omega_f, \\ \rho_p \partial_t^2 u_p - \frac{\rho_p c_p^2}{\phi \gamma_p} \partial_x^2 u_p + \sigma \partial_t u_p = 0 & \text{in } (0, T) \times \Omega_p, \\ u_f = \phi u_p & \text{on } (0, T) \times \Gamma, \\ \rho_f c_f^2 \partial_x u_f = \frac{\rho_p c_p^2}{\phi^2 \gamma_p} \partial_x u_p & \text{on } (0, T) \times \Gamma, \\ u_f = g & \text{on } (0, T) \times \Gamma_0, \\ \phi \partial_t u_p + \frac{\rho_p c_p^2}{\rho_f c_f \phi \gamma_p} \partial_x u_p = 0 & \text{on } (0, T) \times \Gamma_1. \end{cases} \quad (\mathcal{P}_4)$$

4.3 Poro-elastic Models

This section is home to the most complex models used in this project. The models included here represent the behavior of poro-elastic materials, where many factors come into play, such as thermal and viscous effects that were not previously modeled in simpler formulations.

4.3.1 Umnova's Low Frequency Approximation on Porous Media

Following the Umnova's lead, the first model of this kind is an unbounded porous model. In the paper, the following two equations are proposed as low frequency approximations of the fluid-equivalent model used for poro-elastic materials (Eq. (11) and (14) in [52]). Thanks to the low frequency approximation, the time convolutions are avoided and the model is approximated as follows:

$$\begin{cases} \rho_f \alpha_\infty \partial_t v + \frac{\rho_f \alpha_\infty}{\tau_1} v = -\partial_x p, \\ \gamma_p \partial_t p = -\rho_f c_f^2 \partial_x v, \end{cases} \quad (12)$$

where v and p are the velocity and the pressure field, respectively, and α_∞ is the tortuosity. Additionally, coefficient τ_1 is defined by

$$\tau_1 = \frac{\alpha_\infty \rho_f}{\phi \sigma}.$$

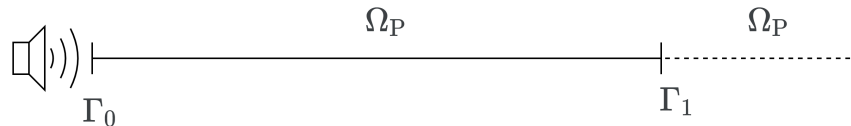


Figure 16: Diagram of the coupled problem involving Umnova's porous model.

It is important to note that these equations are formulated in terms of pressures and velocities while this project has been working with displacements. For this reason the first thing that must be done is to transform it to the kind of formulation that has appeared throughout the project. Taking the time

derivative of the first equation in (12) and the spatial derivative of the second equation in (12), and adding them together,

$$\rho_f \alpha_\infty \partial_t^2 v + \frac{\rho_f \alpha_\infty}{\tau_1} \partial_t v - \frac{\rho_f c_f^2}{\gamma_p} \partial_x^2 v = -\partial_{tx} p + \partial_{xt} p. \quad (13)$$

Assuming that fields v and p are smooth, then $\partial_{tx} p = \partial_{xt} p$. Substituting τ_1 too it is possible to eliminate p from the formulation. Consider that $v = \partial_t u_p$, so the expression becomes

$$\rho_f \alpha_\infty \partial_t^3 u_p + \phi \sigma \partial_t^2 u_p - \frac{\rho_f c_f^2}{\gamma_p} \partial_{xxt} u_p = 0. \quad (14)$$

Integrating in time the equation can be transformed back to a second order (in time) partial differential equation:

$$\rho_f \alpha_\infty \partial_t^2 u_p + \phi \sigma \partial_t u_p - \frac{\rho_f c_f^2}{\gamma_p} \partial_x^2 u_p = 0. \quad (15)$$

Boundary conditions are needed in order to model this configuration of the impedance tube. Since one of the requirements is to control the displacement of the left boundary through a function of pressure, as is done in [52], a relationship between the two must be established. Substituting $v = \partial_t u_p$ in the second equation in (12) and integrating on time, it holds

$$p = -\frac{\rho_f c_f^2}{\gamma_p} \partial_x u_p. \quad (16)$$

This can be used in the speaker boundary in order to input a pressure function. The other condition must be a transparent condition, whose form is not clear. For this reason, a different strategy is used in order to find the differential model. The strategy followed here involves formulating the problem in the harmonic frequency domain, where it is easier to define the equations, and then transforming it back to the time domain. Now, it is possible to transform (15) and write in at the frequency domain. Assuming that $u_p(t, x) = \text{Re}(U_p(x)e^{-i\omega t})$ being ω the angular frequency and U_p the complex-valued harmonic displacement field, it holds

$$-(\omega^2 \rho_f \alpha_\infty + i\omega \phi \sigma) U_p - \frac{\rho_f c_f^2}{\gamma_p} \partial_x^2 U_p = 0. \quad (17)$$

Solving the characteristic polynomial yields the wave number,

$$k_p = \sqrt{\frac{\gamma_p}{\rho_f c_f^2} (\omega^2 \rho_f \alpha_\infty + i\omega \phi \sigma)}. \quad (18)$$

The problem is that in order to be able to use this wave number, it needs to be real, while this expression is complex. So an approximation of its value using a first order Taylor approximation is used. Higher orders would result in not meeting the order of the Newmark method that is being employed to solve the models. Defining

$$k_p = \omega \bar{k}(r) = \omega \sqrt{C_1 + \frac{C_2}{r}}, \quad (19)$$

where

$$C_1 = \frac{\gamma_p \alpha_\infty}{c_f^2} \in \mathbb{R}^+, \quad C_2 = \frac{\phi \gamma_p \sigma}{\rho_f c_f^2} \in \mathbb{R}^+, \quad r = -i\omega.$$

The first order Taylor approximation centered at $r = r_0$ results in

$$\bar{k}(r) \approx A_0 + A_1 r, \quad (20)$$

where

$$A_0 = \frac{2r_0C_1 + 3C_2}{2r_0\bar{k}(r_0)},$$

$$A_1 = \frac{-C_2}{2r_0^2\bar{k}(r_0)}.$$

Substituting $r = -i\omega$ in (20) and then $k_p \approx \omega\bar{k}$ in the Sommerfeld transparent condition in the frequency domain,

$$-ik_p U_p + \partial_x U_p = 0, \quad (21)$$

the following expression is obtained,

$$-\omega(A_0 - i\omega A_1) U_p + \partial_x U_p = 0, \quad (22)$$

which can be transformed back to the time domain.

$$A_1 \partial_t^2 u_p + A_0 \partial_t u_p + \partial_x u_p = 0. \quad (23)$$

Collecting the domain equation (15) and the boundary conditions (16) and (22), a differential model on displacements that approximates that of Umnova's [52] low frequency approximation on unbounded poro-elastic materials is obtained,

$$\begin{cases} \frac{\rho_f \alpha_\infty}{\phi} \partial_t^2 u_p + \sigma \partial_t u_p - \frac{\rho_f c_f^2}{\phi \gamma_p} \partial_x^2 u_p = 0 & \text{on } (0, T) \times \Omega_p, \\ -\frac{\rho_f c_f^2}{\gamma_p} \partial_x u_p = g & \text{on } (0, T) \times \Gamma_0, \\ A_1 \partial_t^2 u_p + A_0 \partial_t u_p + \partial_x u_p = 0 & \text{on } (0, T) \times \Gamma_1, \end{cases} \quad (\mathcal{P}_5)$$

being $g \in \mathcal{C}([0, T])$ any time-dependent (spatially-constant) function that describes the pressure at the left boundary. Multiplying the first equation by a test function $w \in H^1(\Omega_p)$, integrating it over the porous domain, integrating by parts, and substituting the boundary conditions, yields the variational formulation: Given a boundary term $g \in \mathcal{C}([0, T])$ and the initial conditions for the displacement and the velocity fields, u_p^0 and v_p^0 in $H^1(\Omega_p)$ respectively (satisfying the boundary conditions $u_p^0 = g(0)$ on Γ_0 and $v_p^0 = g'(0)$), find $u_p \in C^2((0, T), L^2(\Omega_p)) \cap C^1([0, T], H^1(\Omega_p))$ such that $u_p(0, \cdot) = u_p^0$, $\partial_t u_p(0, \cdot) = v_p^0$, and it holds

$$\begin{aligned} & \int_{\Omega_p} \frac{\rho_f \alpha_\infty}{\phi} \partial_t^2 u_p \cdot w \, dx + \left(A_1 \frac{\rho_f c_f^2}{\phi \gamma_p} \partial_t^2 u_p \cdot w \right|_{\Gamma_1} + \int_{\Omega_p} \sigma \partial_t u_p \cdot w \, dx \\ & + \left(A_0 \frac{\rho_f c_f^2}{\phi \gamma_p} \partial_t u_p \cdot w \right|_{\Gamma_1} + \int_{\Omega_p} \frac{\rho_f c_f^2}{\phi \gamma_p} \partial_x u_p \cdot \partial_x w \, dx = \left(\frac{1}{\phi} g \cdot w \right|_{\Gamma_0}, \end{aligned} \quad (\mathcal{V}_5)$$

for all $w \in H^1(\Omega_p)$. Due to the low-order Taylor approximation used, this model is imperfect in the way the sound waves are transmitted on the transparent boundary. This is something to keep in mind, but a simple solution to the problem is to elongate the domain beyond what is needed so that the dissipation caused by the poro-elastic material corrects and minimizes the defects present in the formulation. This will be explored with greater detail in the validation of the model.

4.3.2 Umnova's Low Frequency Approximation on Fluid-Porous Coupled Media with Speaker-Rigid Boundaries

Having a working fluid-porous coupled model with rigid boundaries on one side (model (P₃)) and a better porous model on the other (model (P₅)), it becomes a matter of joining them together in order to improve

the first and expand its capabilities to poro-elastic media. As in the previous model, upon which this one is based on, this is a low frequency approximation:

$$\begin{cases} \rho_f \partial_t^2 u_f - \rho_f c_f^2 \partial_x^2 u_f = 0 & \text{in } (0, T) \times \Omega_f, \\ \frac{\rho_f \alpha_\infty}{\phi} \partial_t^2 u_p + \sigma \partial_t u_p - \frac{\rho_f c_f^2}{\phi \gamma_p} \partial_x^2 u_p = 0 & \text{in } (0, T) \times \Omega_p, \\ u_f = \phi u_p & \text{on } (0, T) \times \Gamma, \\ \phi \gamma_p \partial_x u_f = \partial_x u_p & \text{on } (0, T) \times \Gamma, \\ -\frac{\rho_f c_f^2}{\gamma} \partial_x u_p = g & \text{on } (0, T) \times \Gamma_0, \\ u_p = 0 & \text{on } (0, T) \times \Gamma_1. \end{cases} \quad (\mathcal{P}_6)$$



Figure 17: Diagram of Umnova's low model involving a fluid-porous coupled media with speaker-rigid boundaries.

This model includes both the wave equation for the fluid domain Ω_f , Umnova's low frequency approximation [52] for the porous domain Ω_p , a coupling between the domains in the interface Γ , a pressure controlled boundary Γ_0 and a rigid null boundary Γ_1 . Substituting the boundary condition on Γ_0 with a simple Dirichlet condition gives a model controlled by displacements instead of by pressures. In the same fashion as it has been done until now, the variational formulation is found to be the following: Given a boundary term $g \in C([0, T])$ and the initial conditions for the displacement and the velocity fields, u_f^0 and v_f^0 in $H^1(\Omega_f)$, and u_p^0 and v_p^0 in $H_{\Gamma_1}^1(\Omega_p)$ respectively (and satisfying the coupling conditions $u_f^0 = u_p^0$ and $v_f^0 = v_p^0$), find $u_f \in C^2((0, T), L^2(\Omega_f)) \cap C^1([0, T], H^1(\Omega_f))$ and $\tilde{u}_p \in C^2((0, T), L^2(\Omega_p)) \cap C^1([0, T], H_{\Gamma_1}^1(\Omega_p))$ such that $u_f = \tilde{u}_p$ on $(0, T) \times \Gamma$, $u_f(0, \cdot) = u_f^0$, $\partial_t u_f(0, \cdot) = v_f^0$, $\tilde{u}_p(0, \cdot) = u_p^0$, $\partial_t \tilde{u}_p(0, \cdot) = v_p^0$, and it holds

$$\begin{aligned} & \int_{\Omega_f} \rho_f \partial_t^2 u_f \cdot w \, dx + \int_{\Omega_p} \frac{\rho_f \alpha_\infty}{\phi^2} \partial_t^2 \tilde{u}_p \cdot w \, dx + \int_{\Omega_p} \frac{\sigma}{\phi} \partial_t \tilde{u}_p \cdot w \, dx \\ & + \int_{\Omega_f} \rho_f c_f^2 \partial_x u_f \cdot \partial_x w \, dx + \int_{\Omega_p} \frac{\rho_f c_f^2}{\phi^2 \gamma_p} \partial_x \tilde{u}_p \cdot \partial_x w \, dx = (\gamma_p g \cdot w|_{\Gamma_0}, \end{aligned} \quad (\mathcal{V}_6)$$

for all $w \in H^1(\Omega)$.

5 Discretization Algorithms

A few algorithms were used throughout the development of this project. Each of them meets one function and they rely on each other to achieve the results that are seek. Considering the described models it is apparent that finding an exact solution is not a viable option. For this reason, the logical next step that is needed in order to find a solution is to resort to numerical methods. Two different methods are needed for the two necessary discretizations. In the spatial domain the discretization is performed through a finite element method (FEM), whereas the Newmark-beta integration method is used in the time domain discretization. Both methods are widely used in acoustics.

5.1 Finite Element Method

The finite element method (FEM) is by far the most widespread technique used when solving mathematical models, from structural mechanics [39, 57] to fluid flow [58, 35]. It works by subdividing the computational domain into smaller parts (mesh) with some special features. Since the developed models only have a single spatial dimension, the selection of the kind of elements and the discretization itself is greatly simplified. Furthermore, since only a baseline working model is needed, the simplest kind of elements were selected: \mathbb{P}_1 -approximations are used for each element in the mesh.

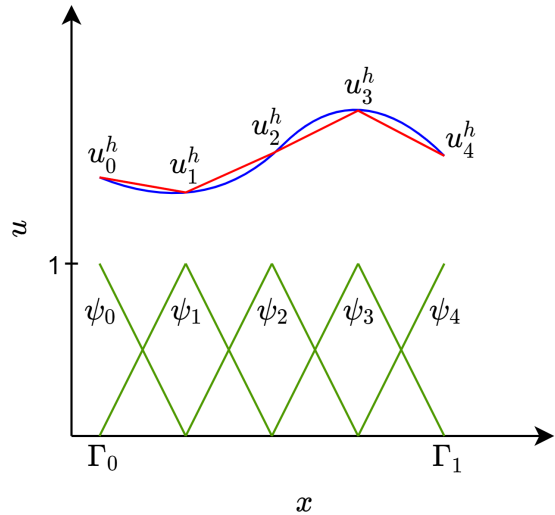


Figure 18: Diagram of the linear \mathbb{P}_1 -elements. The exact solution (blue line) is approximated by the numerical solution (red line) as a linear combination of the basis functions (green lines). In the picture, the red line represents the interpolation function into the FEM discrete space.

Although in practice this method was applied internally within the FEniCS library, meaning it was not needed to manually assemble the required matrices, some examples on how to find them are shown, one for a fluid model and another for a coupled model. Firstly, the FEM discrete space is introduced for fluid model (\mathcal{P}_1). Given a mesh $\mathcal{T} = \{T_j\}_{j=1}^N$ of N elements, the discrete space is defined by

$$V_h = \{w \in H_0^1(\Omega_f) : w|_{T_j} \in \mathbb{P}_1, j = 1, \dots, N\}.$$

Hence, the discrete variational formulation of the fluid model with rigid boundaries is written as follows: Given a source term $f \in C([0, T], V_h)$ and the initial conditions for the displacement and the velocity fields, u_f^0 and v_f^0 in V_h respectively, find $u^h \in C^2([0, T], V_h)$ such that $u^h(0, \cdot) = u_f^0$, $\partial_t u^h(0, \cdot) = v_f^0$, and

it holds

$$\int_{\Omega_f} \rho_f \partial_t^2 u^h \cdot w^h \, dx + \int_{\Omega_f} \rho_f c_f^2 \partial_x u^h \cdot \partial_x w^h \, dx = \int_{\Omega_f} f \cdot w^h \, dx, \quad (\mathcal{V}_1^h)$$

for all $w^h \in V_h$. Seeking the discretization of this expression, $N+1$ equally spaced nodes with coordinates x_0, x_1, \dots, x_N are introduced in the spatial domain, separated by a distance Δx , that carry associated with them the set of basis functions $\{\psi_0, \psi_1, \dots, \psi_N\}$. The discrete variable u^h is used to approximate u_f , and w^h is used to approximate test function w . The basis function ψ_i , located on the interior node $x = x_i$, is defined as

$$\psi_i(x) = \begin{cases} \frac{x - x_{i-1}}{\Delta x} & \text{in } x_{i-1} < x \leq x_i, \\ -\frac{x - x_{i+1}}{\Delta x} & \text{in } x_i < x \leq x_{i+1}, \\ 0 & \text{elsewhere ,} \end{cases} \quad (24)$$

for $i = 1, \dots, N-1$, whereas the basis functions on the boundaries are

$$\psi_0(x) = \begin{cases} -\frac{x - x_1}{\Delta x} & \text{in } x_0 < x \leq x_1, \\ 0 & \text{elsewhere ,} \end{cases} \quad (25)$$

$$\psi_N(x) = \begin{cases} \frac{x - x_{N-1}}{\Delta x} & \text{in } x_{N-1} < x \leq x_N, \\ 0 & \text{elsewhere .} \end{cases} \quad (26)$$

Based on this, it is possible to define the FEM solution

$$u^h(t, x) = \sum_{i=0}^N u_i^h(t) \psi_i(x), \quad (27)$$

and the test functions

$$w^h(x) = \sum_{i=0}^N w_i^h \psi_i(x). \quad (28)$$

Using these discrete approximations in the variational formulation (\mathcal{V}_1^h) and setting the test function $w = \psi_j$, it yields

$$\rho_f \int_{\Omega_f} \sum_{i=0}^N (\partial_t^2 u_i^h \psi_i \cdot \psi_j) \, dx + \rho_f c_f^2 \int_{\Omega_f} \sum_{i=0}^N (u_i^h \partial_x \psi_i \cdot \partial_x \psi_j) \, dx = \int_{\Omega_f} f \cdot \psi_j \, dx, \quad (29)$$

for all $0 \leq i, j \leq N$. Considering the linearity of the expression it can be written as

$$\sum_{i=0}^N M_{j,i} \ddot{u}_i^h + \sum_{i=0}^N K_{j,i} u_i^h = f_j, \quad (30)$$

where

$$\begin{aligned} M_{i,j} &= M_{j,i} = \int_{\Omega_f} \rho_f \psi_i \cdot \psi_j \, dx, \\ K_{i,j} &= K_{j,i} = \int_{\Omega_f} \rho_f c_f^2 \partial_x \psi_i \cdot \partial_x \psi_j \, dx, \\ f_j &= \int_{\Omega_f} f \cdot \psi_j \, dx, \end{aligned}$$

for all $0 \leq i, j \leq N$. Realize that the basis functions are equal to zero on most of the domain, so these expressions can be simplified by splitting the integral in each of the non-zero elements and taking into account that the mass matrix M and the stiffness matrix K are symmetric:

$$\begin{aligned} M_{i,i} &= \int_{x_{i-1}}^{x_i} \rho_f \psi_i^2 dx + \int_{x_i}^{x_{i+1}} \rho_f \psi_i^2 dx = \rho_f \frac{\Delta x}{3}, \\ M_{i,i-1} &= \int_{x_{i-1}}^{x_i} \rho_f \psi_i \psi_{i-1} dx = \rho_f \frac{\Delta x}{6}, \\ K_{i,i} &= \int_{x_{i-1}}^{x_i} \rho_f c_f^2 (\partial_x \psi_i)^2 dx + \int_{x_i}^{x_{i+1}} \rho_f c_f^2 (\partial_x \psi_i)^2 dx = \rho_f c_f^2 \frac{2}{\Delta x}, \\ K_{i,i-1} &= \int_{x_{i-1}}^{x_i} \rho_f c_f^2 \partial_x \psi_i \cdot \partial_x \psi_{i-1} dx = -\rho_f c_f^2 \frac{1}{\Delta x}, \end{aligned}$$

for all $1 \leq i \leq N$. The rest of the overlaps in the lower part (and therefore the rest of the entries of lower part of both matrices) are equal to zero due to the product between the basis functions. This however does not apply to the vector f , where there is no product because of its global character.

The second example discretization that will be shown is that of the coupled model (\mathcal{P}_4). In this case, consider that u^h represents either a discrete approximation of u_f or \tilde{u}_p depending on the subdomain in which it is found, and consequently the discrete space is defined by

$$V_h = \{w \in H_{\Gamma_0}^1(\Omega) : w|_{T_j} \in \mathbb{P}_1, j = 1, \dots, N\},$$

where the mesh $\mathcal{T} = \{T_j\}_{j=1}^N$ is compatible with the coupling boundary Γ . Its discrete variational formulation is described as follows: Given a source term $f \in \mathcal{C}([0, T], V_h)$ and suitable initial conditions for the displacement and the velocity fields, u^0 and v^0 in V_h , find $u^h \in \mathcal{C}^2([0, T], V_h)$ such that $u^h(0, \cdot) = u^0$, $\partial_t u^h(0, \cdot) = v^0$, and it holds

$$\begin{aligned} &\int_{\Omega_f} \rho_f \partial_t^2 u^h \cdot w^h dx + \int_{\Omega_p} \frac{\rho_p}{\phi} \partial_t^2 u^h \cdot w^h dx + \int_{\Omega_p} \frac{\sigma}{\phi} \partial_t u^h \cdot w^h dx \\ &+ (\rho_f c_f \partial_t u^h \cdot w^h)|_{\Gamma_1} + \int_{\Omega_f} \rho_f c_f^2 \partial_x u^h \cdot \partial_x w^h dx + \int_{\Omega_p} \frac{\rho_p c_p^2}{\phi^2 \gamma_p} \partial_x u^h \cdot \partial_x w^h dx = \int_{\Omega_f} f \cdot w^h dx, \end{aligned} \quad (\mathcal{V}_4^h)$$

for all $w^h \in V_h$. The same basis functions will be used (see (24), (25) and (26)), so the FEM solution and test functions are still (27) and (28). Introducing the discrete approximations in the variational formulation of the problem yields

$$\begin{aligned} &\int_{\Omega_f} \sum_{i=0}^N (\rho_f \partial_t^2 u_i^h \psi_i \cdot \psi_j) dx + \int_{\Omega_p} \sum_{i=0}^N \left(\frac{\rho_p}{\phi} \partial_t^2 u_i^h \psi_i \cdot \psi_j \right) dx \\ &+ \int_{\Omega_p} \sum_{i=0}^N \left(\frac{\sigma}{\phi} \partial_t u_i^h \psi_i \cdot \psi_j \right) dx + \left(\sum_{i=0}^N (\rho_f c_f \partial_t u_i^h \psi_i \cdot \psi_j) \right) \Big|_{\Gamma_1} \\ &+ \int_{\Omega_f} \sum_{i=0}^N (\rho_f c_f^2 u_i^h \partial_x \psi_i \cdot \partial_x \psi_j) dx + \int_{\Omega_p} \sum_{i=0}^N \left(\frac{\rho_p c_p^2}{\phi^2 \gamma_p} u_i^h \partial_x \psi_i \cdot \partial_x \psi_j \right) dx \\ &= \int_{\Omega_f} f \cdot \psi_j dx. \end{aligned} \quad (31)$$

Applying linearity it is possible to extract the terms that are dependent on u_i^h to get

$$\sum_{i=0}^N M_{j,i} \ddot{u}_i^h + \sum_{i=0}^N C_{j,i} \dot{u}_i^h + \sum_{i=0}^N K_{j,i} u_i^h = f_j. \quad (32)$$

where

$$\begin{aligned} M_{i,j} &= \int_{\Omega_f} \rho_f \psi_i \psi_j dx + \int_{\Omega_p} \frac{\rho_p}{\phi} \psi_i \psi_j dx, \\ C_{i,j} &= \int_{\Omega_p} \frac{\sigma}{\phi} \psi_i \psi_j dx + (\rho_f c_f \psi_i \psi_j|_{\Gamma_1}, \\ K_{i,j} &= \int_{\Omega_f} \rho_f c_f^2 \partial_x \psi_i \cdot \partial_x \psi_j dx + \int_{\Omega_p} \frac{\rho_p c_p^2}{\phi^2 \gamma_p} \partial_x \psi_i \cdot \partial_x \psi_j dx, \\ f_i &= \int_{\Omega_f} f \psi_i dx. \end{aligned}$$

Considering the overlap of the basis functions as before,

$$\begin{aligned} M_{i,i} &= \int_{\Omega_f} \rho_f \psi_i^2 dx + \int_{\Omega_p} \frac{\rho_p}{\phi} \psi_i^2 dx, \\ M_{i,i-1} &= \int_{\Omega_f} \rho_f \psi_i \psi_{i-1} dx + \int_{\Omega_p} \frac{\rho_p}{\phi} \psi_i \psi_{i-1} dx, \\ C_{i,i} &= \int_{\Omega_p} \frac{\sigma}{\phi} \psi_i^2 dx + (\rho_f c_f \psi_i^2|_{\Gamma_1}, \\ C_{i,i-1} &= \int_{\Omega_p} \frac{\sigma}{\phi} \psi_i \psi_{i-1} dx + (\rho_f c_f \psi_i \psi_{i-1}|_{\Gamma_1}, \\ K_{i,i} &= \int_{\Omega_f} \rho_f c_f^2 (\partial_x \psi_i)^2 dx + \int_{\Omega_p} \frac{\rho_p c_p^2}{\phi^2 \gamma_p} (\partial_x \psi_i)^2 dx, \\ K_{i,i-1} &= \int_{\Omega_f} \rho_f c_f^2 \partial_x \psi_i \cdot \partial_x \psi_{i-1} dx + \int_{\Omega_p} \frac{\rho_p c_p^2}{\phi^2 \gamma_p} \partial_x \psi_i \cdot \partial_x \psi_{i-1} dx, \end{aligned}$$

which is dependent on where the domains are placed and must be calculated for each problem. The rest of the entries will be empty. These matrices are the ones that will be later used in the Newmark scheme. It is to be noted that the structure of the resulting ordinary differential equation is that of the Newmark method since this is its source. However, due to the simplicity of the model, in the first example no damping matrix appears, only the mass and the stiffness matrices, as well as the external forces vector are present. This corresponds to what was commented in the previous chapter, when the models were developed.

5.2 Newmark-Beta Method

In the same way that FEM was used to subdivide the spatial dimension, so is done for the time dimension with this method. Newmark-beta method [36] is a numerical integration scheme commonly used to solve differential equations in dynamic response systems, usually in association with FEM, as done here. It offers a semi-discretized structural equation of second order, that combined with FEM reduces the PDE to an ODE,

$$M\ddot{u} + C\dot{u} + Ku = f, \quad (33)$$

where M represents the mass matrix, C is the damping matrix, K is the stiffness matrix and F are the external forces. This aligns very well with the terms seen in the variational formulations of the models and the FEM, which simplifies the implementation. The discrete form of the method can be written as

$$\begin{cases} u^{n+1} = u^n + \Delta t \dot{u}^n + \left(\frac{1}{2} - \beta\right) \Delta t^2 \ddot{u}^n + \beta \Delta t^2 \ddot{u}^{n+1}, \\ \dot{u}^{n+1} = \dot{u}^n + (1 - \gamma) \Delta t \ddot{u}^n + \gamma \Delta t \ddot{u}^{n+1}, \\ M\ddot{u}^{n+1} + C\dot{u}^{n+1} + Ku^{n+1} = f^{n+1}, \end{cases} \quad (34)$$

where γ and β represent the method's parameters, n is the current time step of the method and Δt the time step size. In this case $\gamma = 0.5$ and $\beta = 0.25$ were used, which corresponds to the middle point rule. These parameters were chosen because using them the method becomes unconditionally stable, whereas with other configurations is only conditionally stable. In practice the implementation of the method is divided in three parts. It begins with an initialization, in which the problem matrix A is created:

$$\begin{cases} A = \frac{1}{\beta \Delta t^2} M + \frac{\gamma}{\beta \Delta t} C + K, \\ u^0 = u_0, \\ \dot{u}^0 = v_0, \\ \ddot{u}^0 = M^{-1} (f^0 - C\dot{u}^0 - Ku^0), \end{cases} \quad (35)$$

where u_0 and v_0 are the initial conditions of the problem. In each time loop, the method then establishes some explicit prediction values for the displacement and the velocity,

$$\begin{cases} u_{pr}^{n+1} = u^n + \Delta t \dot{u}^n + \left(\frac{1}{2} - \beta \right) \Delta t^2 \ddot{u}^n, \\ \dot{u}_{pr}^{n+1} = \dot{u}^n + (1 - \gamma) \Delta t \ddot{u}^n. \end{cases} \quad (36)$$

These predictions are then used to obtain the final values of each variable for each iteration of the method as follows:

$$\begin{cases} F^{n+1} = f^{n+1} + \frac{1}{\beta \Delta t^2} M u_{pr}^{n+1} + \left(\frac{\gamma}{\beta \Delta t} u_{pr}^{n+1} - \dot{u}_{pr}^{n+1} \right) C, \\ u^{n+1} = A^{-1} F^{n+1}, \\ \dot{u}^{n+1} = \dot{u}_{pr}^{n+1} + \frac{\gamma}{\beta \Delta t} (u^{n+1} - u_{pr}^{n+1}), \\ \ddot{u}^{n+1} = \frac{1}{\beta \Delta t^2} (u^{n+1} - u_{pr}^{n+1}). \end{cases} \quad (37)$$

Although the method is unconditionally stable, it is important to choose a correct time step size in order to increase the success at lower resolutions. The Courant-Friedrich-Lowy (CFL) condition establishes that the time step must be smaller than a certain size in order for the numerical solution to be convergent. In particular for the one-dimensional case,

$$C = \frac{\Delta t}{\Delta x} c_f \leq C_{\max}. \quad (38)$$

The exact value of C_{\max} depends on the method, but, for explicit methods such as this project's, it is common to use $C_{\max} = 1$. This in essence, and in order to minimize the execution time, means that the mesh speed must be the same as the speed of propagation of sound:

$$\frac{\Delta x}{\Delta t} = c_f. \quad (39)$$

The effects of not choosing the correct ratio will be showcased later, but for now it is important to note that using this condition only one of the increments must be chosen, while the other can be calculated. Generally the mesh size was chosen and the time step calculated.

6 Reduced Order Methods

The discretization methods are able to solve the models numerically and it is thanks to them that the simulations are run. The results of the simulations are a series of snapshots that describe the displacement (or the velocity, acceleration and pressure if needed) in each of the discrete spatial points at each of the discrete times. The second part of the project consists in applying a reduced order method (ROM), in particular dynamic mode decomposition (DMD), to be able to speed up the computation of a solution by making predictions and performing reconstructions of the snapshots. Since DMD relies heavily in a more classical ROM, the singular value decomposition (SVD), and since a comparison between them is performed later in this report, both methods will be described next.

6.1 Singular Value Decomposition

The singular value decomposition (SVD) is a matrix factorization algorithm that is able to decompose a $n \times m$ matrix much in the same way the eigendecomposition decomposes square diagonalizable matrices. It is a data-driven method that has been widely used in a variety of fields. Given a matrix $A \in \mathbb{R}^{n \times m}$, SVD is able to factorize it as

$$A = U\Sigma V^T, \quad (40)$$

where V^T denotes the conjugate transpose of V , and $U \in \mathbb{R}^{n \times n}$, $\Sigma \in \mathbb{R}^{n \times m}$, $V \in \mathbb{R}^{m \times m}$. In addition, U and V form orthonormal bases, meaning that $U^T U = I_n$ and $V^T V = I_m$. The matrix U is comprised of the left singular vectors as columns, Σ contains in its diagonal the singular values ordered in a decreasing sequence, and V^T is composed of the right singular vectors as rows. Calculating the decomposition is a very straight forward process. The left singular vectors are simply the eigenvectors of AA^T , the right singular vectors are the eigenvectors of $A^T A$, and the singular values are the square roots of the eigenvalues of either AA^T or $A^T A$. The matrix AA^T will be a symmetric and semidefinite positive matrix, meaning the eigenvalues will be real and non-negative, and so will the singular values be:

$$A = \begin{bmatrix} | & | & & | \\ u_1 & u_2 & \dots & u_n \\ | & | & & | \end{bmatrix}_{n \times n} \begin{bmatrix} \sigma_1 & & & \\ & \sigma_2 & & \\ & & \ddots & \\ & & & \sigma_{\min(n,m)} \end{bmatrix}_{n \times m} \begin{bmatrix} - & v_1 & - \\ - & v_2 & - \\ \vdots & & \\ - & v_m & - \end{bmatrix}_{m \times m}, \quad (41)$$

where u_i are the left singular vectors, $\sigma_i = \sqrt{\lambda_i}$ are the singular values (being λ_i the eigenvalues), and v_i are the right singular vectors. Notice that Σ is not necessarily a square matrix, so only Σ_{ii} entries are populated, the rest are filled with zeros. This means that the matrix Σ (and therefore A) is of rank $k \leq \min(n, m)$. For this reason, the matrix A can also be expressed as the sum of its modes:

$$A = \sum_{i=1}^k \sigma_i u_i v_i^T. \quad (42)$$

This decomposition is lossless, meaning that by multiplying $U\Sigma V^T$ (or by adding all the modes) the original matrix is obtained. This extracts some useful information codified in the resulting matrices, but it is not a reduced order method. The truncated SVD method however, is. It consists in keeping the most relevant SVD modes. Since the singular values are ordered ($\sigma_1 > \sigma_2 > \dots > \sigma_k > 0$), it is possible to choose a rank $r < k$ such that only $\{u_1, \dots, u_r\}$, $\{\sigma_1, \dots, \sigma_r\}$ and $\{v_1, \dots, v_r\}$ are kept, which are the r most representative modes of the decomposition:

$$A \approx U_r \Sigma_r V_r^T, \quad (43)$$

where $U_r \in \mathbb{R}^{n \times r}, \Sigma_r \in \mathbb{R}^{r \times r}, V_r \in \mathbb{R}^{r \times m}$,

$$A = \begin{bmatrix} | & | & & | \\ u_1 & u_2 & \dots & u_r \\ | & | & & | \end{bmatrix}_{n \times r} \begin{bmatrix} \sigma_1 & & & \\ & \sigma_2 & & \\ & & \ddots & \\ & & & \sigma_r \end{bmatrix}_{r \times r} \begin{bmatrix} --- & v_1 & --- \\ --- & v_2 & --- \\ \vdots & & \vdots \\ --- & v_r & --- \end{bmatrix}_{r \times m}. \quad (44)$$

Using the proportion of variance explained it is possible to get a measure of the compression loss produced by the truncated SVD,

$$\text{var} = \frac{\sum_{i=1}^r \sigma_i^2}{\sum_{i=1}^k \sigma_i^2}. \quad (45)$$

6.2 Dynamic Mode Decomposition

The dynamic mode decomposition (DMD) algorithm [47] is a dimensionality reduction algorithm similar to singular value decomposition (SVD), and in fact, it is used within the DMD algorithm. The main difference between other order reduction methods and DMD is that DMD is dynamic, which means that is able to consider variations in the mode through time, whereas the others rely on static modes. Its main advantage is that it is a data-driven method, so there is no need for the algorithm to have any knowledge of the underlying equations, which enables it to function on experimental data of un-modeled phenomena, not only on simulation results. Its main use is to extract the most relevant spatial modes and their dynamics (i.e. how they develop in time) and to make predictions about its future development. Essentially, the given data is first spatially decomposed through SVD and then a Fourier transform is applied in order to get the time dynamics.

The input to the algorithm is a data matrix formed by a number of equally spaced in time snapshots (although there are newer methods that allow for the use of uneven time steps [51]). There are m snapshots, denominated x_1, x_2, \dots, x_m , and each of them is a vector composed by n spatial points. Two matrices are formed from the given snapshots:

$$X = \begin{bmatrix} | & | & & | \\ x_1 & x_2 & \dots & x_{m-1} \\ | & | & & | \end{bmatrix}, \quad (46)$$

$$X' = \begin{bmatrix} | & | & & | \\ x_2 & x_3 & \dots & x_m \\ | & | & & | \end{bmatrix}, \quad (47)$$

The algorithm starts by decomposing X through a truncated SVD of rank r (see (43)),

$$X \approx U \Sigma V^T, \quad (48)$$

where V^T denotes the conjugate transpose of V , and $U \in \mathbb{R}^{n \times r}, \Sigma \in \mathbb{R}^{r \times r}, V \in \mathbb{R}^{m \times r}$. Next, the matrix A as a pseudo-inverse of X is calculated,

$$A = X' \Sigma^{-1} U^T. \quad (49)$$

While the formulation using matrix A is mathematically correct, the implementation proves to be ill-conditioned in that it is often unable to find any mode except the very most relevant ones, specially if the input data is noisy. For this reason, a more robust approach is to choose a projection of A onto the SVD basis (see [47]),

$$\tilde{A} = U^T X' V \Sigma^{-1}. \quad (50)$$

Then, the eigenvalues (λ_k , contained in the diagonal of Λ , where $i \in \{1, \dots, r\}$) and eigenvectors (contained as columns in W) of \tilde{A} are computed,

$$\tilde{A} = W\Lambda W^{-1}. \quad (51)$$

Finally, the data is reconstructed back to the original space,

$$X \approx \Phi\Lambda, \quad (52)$$

where Φ are the eigenvectors of A , also named DMD modes, and can be calculated as shown below:

$$\Phi = X'V\Sigma^{-1}W. \quad (53)$$

This reconstruction can be useful in terms of denoising and extracting principal components, but in order to predict future values (which is the main concern of this project since that would cut the computation time greatly when compared to having to simulate the entire time domain) it is imperative that the time dimension of the reconstruction is expanded. It can be extended to any desired future time as follows,

$$x(t) \approx \sum_{k=1}^r \phi_k e^{\omega_k t} b_k = \Phi e^{\Omega t} b, \quad (54)$$

where b_k is the initial amplitude of each mode, b the vector that contains them, ϕ_k is each of the modes from Φ , and $\Omega = \text{diag}(\omega_k)$, where $\omega_k = \log(\lambda_k)/\Delta t$ are the continuous time eigenvalues. The vector b can be obtained by

$$b = \Phi^* x_1, \quad (55)$$

where Φ^* denotes the Moore-Penrose pseudoinverse of Φ . In this prediction, Φ represents the spatial modes, and $e^{\Omega t} b$ represents the dynamics. All of this and much more is explained in more detail in [29]. The implementation of this method, as well as of all the variants tested were implemented through the pyDMD package [13].

7 Validation

In this chapter the tests performed in order to troubleshoot the models and to make sure that each of them were behaving correctly are explored. In some occasions an exact solution for certain cases is available, so a comparison between the exact solution and the results of the simulations is used as validation. In others, comparisons to published data or trends in error reduction were used.

7.1 Error Control Through Space and Time Step Size

The first test performed was a test on the implementation of the basic Python program, including the FEM and the Newmark method contained within. Model (P_1) and exact solution (68) were used to perform these tests, since it was the first model available and the results are model independent. The discretization methods were supposed to be of order two, both in time and space, meaning that error ε in the last snapshot of the simulation must hold

$$\varepsilon \leq C_x \Delta x^2 + C_t \Delta t^2, \quad (56)$$

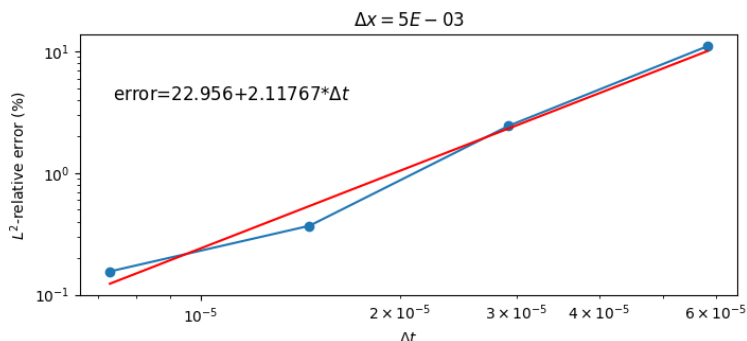
where C_x and C_t are positive constants. Neglecting of the terms in the right-hand side, it is possible to take the logarithm of (56), X being either $\log \Delta x$ or $\log \Delta t$ and Y being the logarithm of the error, and adjust a linear model of the shape

$$\log \varepsilon = Y = a + bX, \quad (57)$$

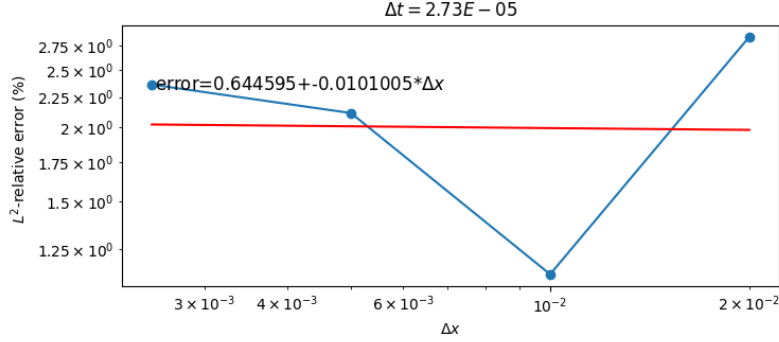
a and b being some constants. Since the methods are of order two, $b \approx 2$ in both cases. At first, as can be seen in Fig. 19, a Δx is fixed and the Δt is changed, or conversely, Δt is fixed and the Δx is changed. Specially in the second case it is easy to appreciate that the slope of the fitted line, understanding that the plot is in logarithmic scale, is far from the desired. The reason for this discrepancy between the theory and the practice is that by keeping constant one of the step sizes, the CFL ratio was not proper, which causes the numerical results not to be accurate as expected. The physical parameters used in Fig. 19 and Fig. 20 are shown in Tab. 1.

Sound speed in fluid	c_f	343 m/s
Fluid density	ρ_f	1.21 kg/m ³

Table 1: Physical parameters.



(a) Static Δx .

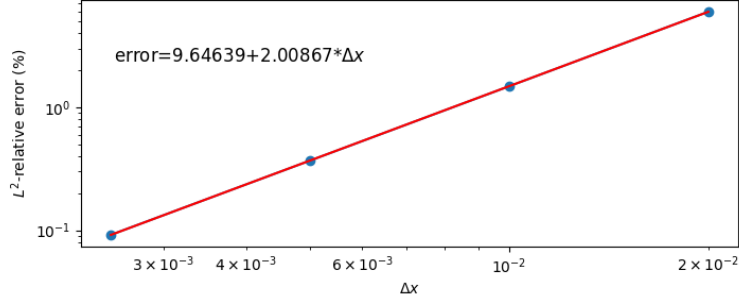


(b) Static Δt .

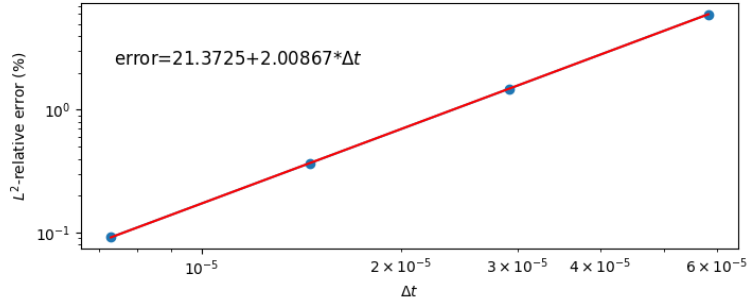
Figure 19: Error reduction trends keeping one of the step sizes static. The CFL ratio is not regarded.

In Fig. 20 both Δx and Δt are varied so that the CFL condition is met. It shows that the slope of the linear fit is in fact equal to two, both in space and in time, as expected, since

$$\Delta t = c_f \Delta x. \quad (58)$$



(a) Error reduction on Δx .



(b) Error reduction on Δt .

Figure 20: Error reduction trends choosing the step sizes in accordance to the CFL condition.

7.2 Exact Result Using d'Alembert's Solution

In cases where the evolution of the sound wave through a fluid is not forced by an external impulse, like that of a speaker, there exists an exact solution called d'Alembert's Solution [11]. Given initial conditions $u_f(0, x) = u_f^0(x)$ and $\partial_t u_f(0, x) = v_f^0(x)$, the exact solution to the wave equation in a open domain is

$$u_f(t, x) = \frac{1}{2} (u_f^0(x - c_f t) + u_f^0(x + c_f t)) + \frac{1}{2c_f} \int_{x - c_f t}^{x + c_f t} v_f^0(\xi) d\xi. \quad (59)$$

This formula provides the solution for an initial condition but is not able to model rigid boundaries. With the purpose of simulating them, the virtual images principle was used. It consists on placing a symmetrical and of opposite sign initial condition beyond the rigid boundary, so that as both travel towards it, they meet and cancel each other precisely where it is needed, and then the virtual solution takes the place of the original within the domain. This method was used to verify fluid models before the introduction of a speaker, that is (P'_1) and (P'_2) .

7.2.1 Fluid Model with Rigid Boundaries

Recall that the model (P'_1) has rigid boundaries at both ends of the domain, which, since there is no dissipation in the fluid media and the rigid boundaries are perfectly rigid, means that the waves will bounce infinitely within the domain, so infinitely many virtual images are needed to get the exact solution at any point in time. However, since the objective of this validation is to test the simulation, only enough reflections to fill the time domain chosen are needed. Two reflections were used.

A diagram of the virtual images used for this model is shown in Fig. 21. In green, the original wave, and since the exact solution is fundamentally unbounded, it passes through both boundaries, Γ_0 and Γ_1 . However, the waves represented in red, which have an opposite amplitude than the original and are only propagated towards the domain Ω_f , destructively interact with the principal solution, effectively canceling out the displacement at the boundaries. This process is repeated as many times as reflections want to be simulated, two in this case.

Choosing $\Omega_f = [0, 1]$ and initial conditions

$$u_f(x, 0) = \begin{cases} \exp\left(\frac{2\exp(-0.2)}{\frac{|x-0.5|}{0.2}-1}\right) & \text{on } |x - 0.5| < 0.2, \\ 0 & \text{elsewhere,} \end{cases} \quad (60)$$

$$\partial_t u_f(x, 0) = 0, \quad (61)$$

it is possible to simulate two reflections of the inert wave. The fist reflection is shown in Fig. 22. As observed, the simulated result, calculated using $\Delta x = 2 \times 10^{-3}$ and $\Delta t = 5.83 \times 10^{-6}$, is almost identical to the exact solution, representing a successful test. The physical parameters used in this test case are shown in Tab. 1.

7.2.2 Fluid Model with Rigid-Transparent Boundaries

The case of model (P'_2) is simpler in this regard, since only one of the boundaries is rigid, while the other is transparent, so only left-going waves must be reflected, which means that only one reflection is needed, since the only source of waves in this model is the initial condition. Therefore, in order to compare the model to its exact solution the principle of virtual images is still available, but since only one of the boundaries emit reflections, only one image is needed.

As seen in Fig. 24, taking the same initial conditions and parameters and applying it to model (P'_2) yields a solution that is very similar in quality to the one observed in the previous case. However it shows clearly how at the right boundary the wave is not reflected but just passes through the transparent boundary. The physical parameters used in this test case are shown in Tab. 1.

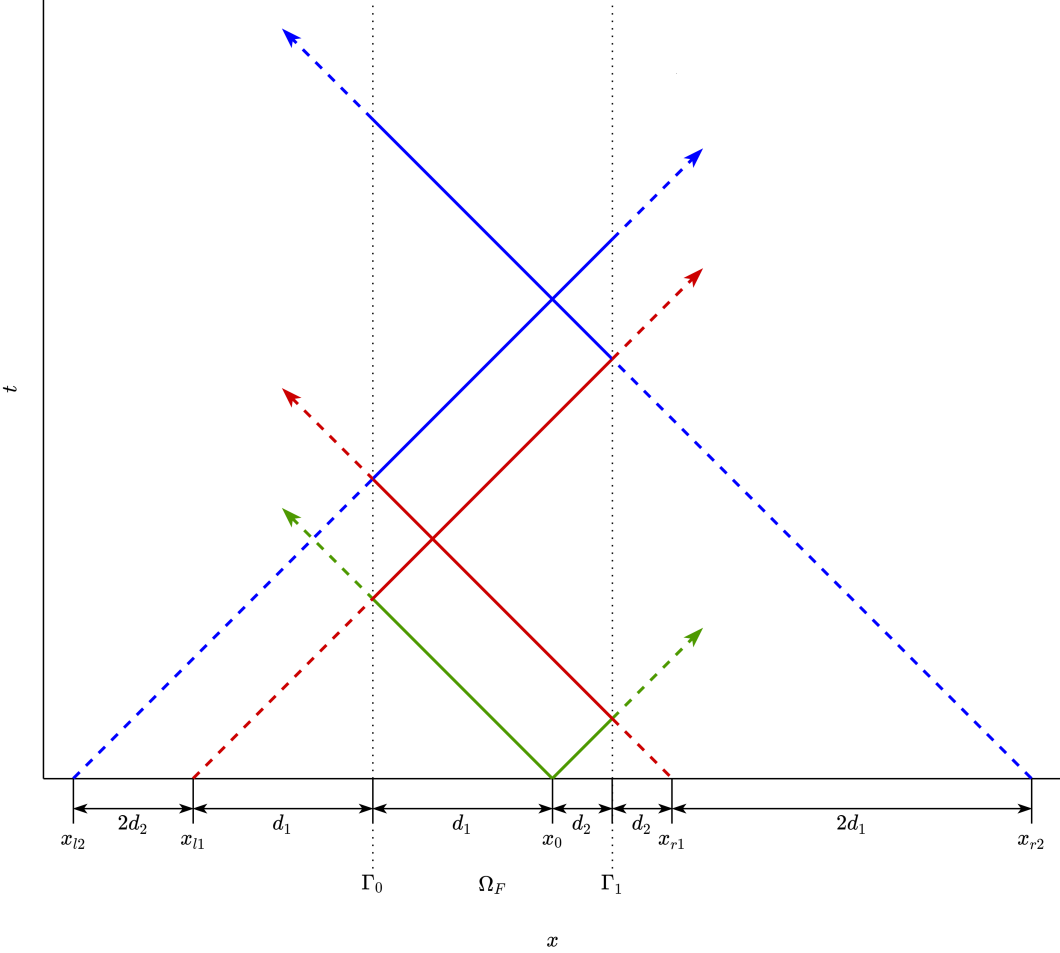


Figure 21: Diagram of the virtual images used in the exact solution of (\mathcal{P}'_1) .

7.3 Exact Result Using Harmonic Solution

Calculating the exact solution through d'Alembert's formula is only possible when no perturbations are applied to the wave and the domain is a perfect fluid. This means that this method does not work on coupled systems, so another method is needed to check the implementation. Using rigid porous media it is possible however to find the exact harmonic solution, as well as in the fluid domain, and it is also possible to couple them together using a harmonic multilayer scheme. Because of this reason, the harmonic solution was used to test models (\mathcal{P}_3) , (\mathcal{P}_4) , (\mathcal{P}_3) and (\mathcal{P}_4) .

7.3.1 Fluid Model with Rigid Boundaries

Firstly, the simplest case is introduced: the harmonic solution in a fluid domain with rigid boundaries, (\mathcal{P}_3) . Since the speaker is placed on the left boundary, this will be free to move, while the right boundary will be perfectly still. The displacement function used on Γ_0 to test this model was

$$g(t) = \operatorname{Re}(e^{-i\omega t}) = \cos(\omega t), \quad (62)$$

where ω is the frequency of the harmonic wave. Introducing this function in (\mathcal{P}_1) , the time-domain model can then be taken to the frequency domain (assuming $u_f(t, x) = \operatorname{Re}(e^{-i\omega t} U_f(x))$ with U_f a complex-valued

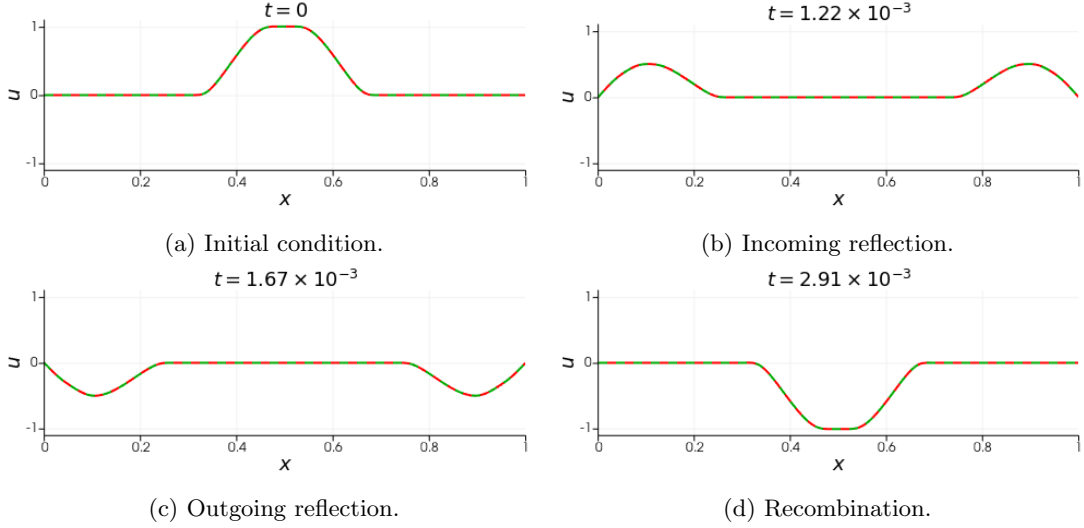


Figure 22: Development of the first complete reflection given the initial conditions (60) and (61) on model (\mathcal{P}'_1) . In red, the simulated solution, in green the exact d'Alembert's solution.

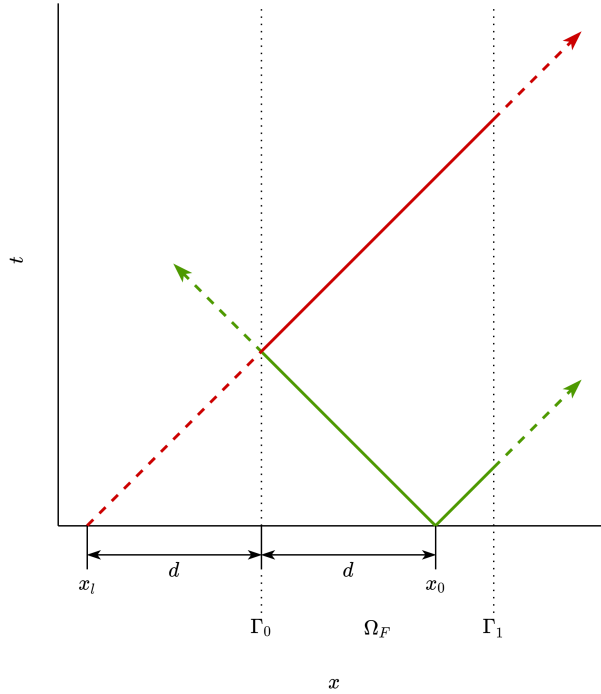


Figure 23: Diagram of the virtual images used in the exact solution of (\mathcal{P}'_2) .

function), which results in the following Helmholtz equation:

$$\begin{cases} -\omega^2 \rho_f U_f - \rho_f c_f^2 \partial_x^2 U_f = 0 & \text{in } \Omega_f, \\ U_f = 1 & \text{on } \Gamma_0, \\ U_f = 0 & \text{on } \Gamma_1. \end{cases} \quad (63)$$

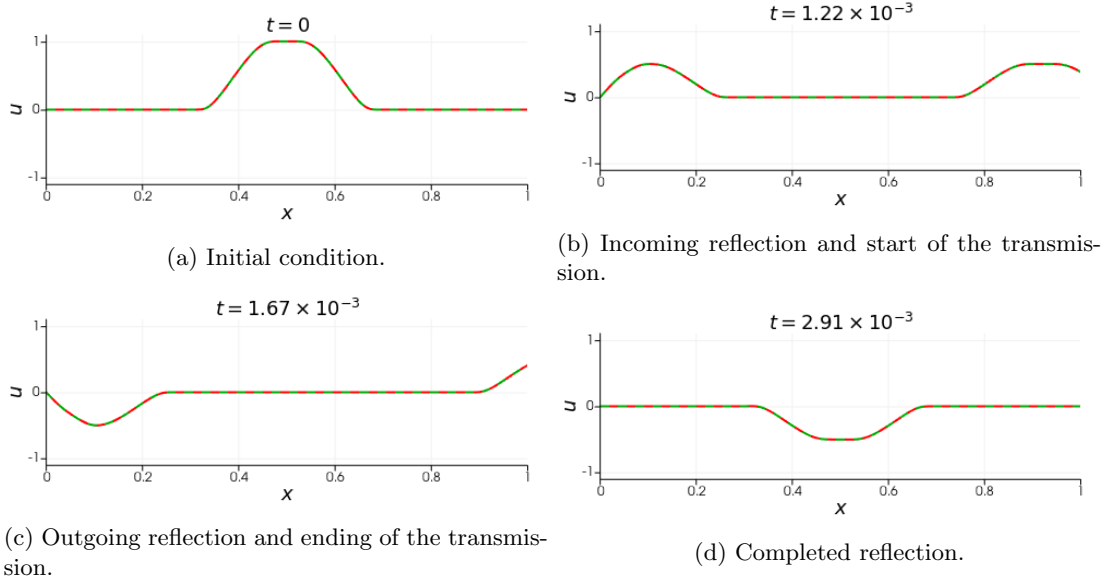


Figure 24: Development of the first complete reflection given the initial conditions (60) and (61) on model (\mathcal{P}'_2) . In red, the simulated solution, in green the exact d'Alembert's solution.

By solving the characteristic polynomial of the first equation, the wave number k_f is obtained:

$$-\rho_f c_f^2 \lambda^2 - \omega^2 \rho_f = 0 \implies \lambda = \pm i \sqrt{\frac{\omega^2}{c_f^2}} = \pm i k_f. \quad (64)$$

Using this λ the general harmonic solution is formed, which solves the Helmholtz equation:

$$U_f(x) = A e^{\lambda_1 x} + B e^{\lambda_2 x} = A e^{-i k_f x} + B e^{i k_f x}. \quad (65)$$

Substitute this expression in the second and third equations in (63) in order to find the coefficients A and B . Defining for simplicity $x|_{\Gamma_0} = L_0$ and $x|_{\Gamma_1} = L_1$,

$$\begin{cases} U_f|_{\Gamma_0} = A e^{-i k_f L_0} + B e^{i k_f L_0} = 1, \\ U_f|_{\Gamma_1} = A e^{-i k_f L_1} + B e^{i k_f L_1} = 0, \end{cases} \quad (66)$$

which yields

$$\begin{cases} A = \frac{1}{e^{-i k_f L_0} - e^{-i k_f (2L_1 - L_0)}}, \\ B = \frac{1}{e^{i k_f L_0} - e^{i k_f (2L_1 - L_0)}}. \end{cases} \quad (67)$$

This gives the harmonic solution, which can be transformed back to the time domain to get the exact solution needed:

$$u_f(t, x) = \operatorname{Re}(e^{-i \omega t} U_f(x)) = \operatorname{Re}\left(e^{-i \omega t} \left(\frac{e^{-i k_f x}}{e^{-i k_f L_0} - e^{-i k_f (2L_1 - L_0)}} + \frac{e^{i k_f x}}{e^{i k_f L_0} - e^{i k_f (2L_1 - L_0)}}\right)\right). \quad (68)$$

Therefore, the initial conditions for the simulation will be

$$u_f(x, 0) = \operatorname{Re}\left(\frac{e^{-i k_f x}}{e^{-i k_f L_0} - e^{-i k_f (2L_1 - L_0)}} + \frac{e^{i k_f x}}{e^{i k_f L_0} - e^{i k_f (2L_1 - L_0)}}\right), \quad (69)$$

$$\partial_t u_f(x, 0) = \operatorname{Re}\left(-i \omega \left(\frac{e^{-i k_f x}}{e^{-i k_f L_0} - e^{-i k_f (2L_1 - L_0)}} + \frac{e^{i k_f x}}{e^{i k_f L_0} - e^{i k_f (2L_1 - L_0)}}\right)\right). \quad (70)$$

Compare this solution to the simulated solution to see (in Fig. 25). The results are highly accurate. As a result of the harmonic motion and the rigid boundary, a standing wave is generated. The physical parameters used in this test case are shown in Tab. 1.

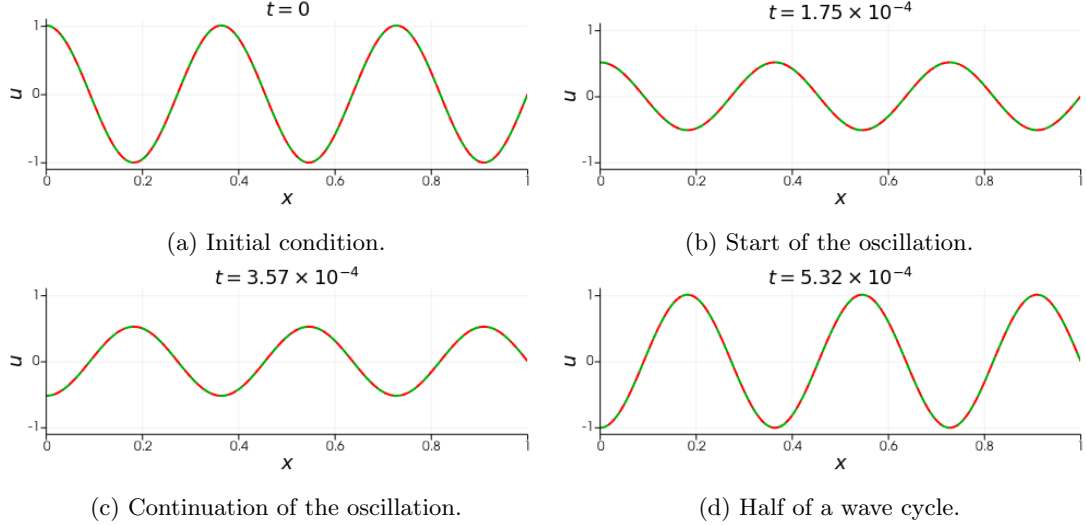


Figure 25: Development of the first half of a wave cycle of the standing wave given by the initial conditions (69) and (70) on model (\mathcal{P}_1). In red, the simulated solution, in green the exact harmonic solution.

7.3.2 Fluid Model with Rigid-Transparent Boundaries

The same process can be performed on model (\mathcal{P}_2). Using the same boundary function (62), the time domain model can be transformed into the following frequency domain model, which uses the frequency domain version of the Sommerfeld transparent condition:

$$\begin{cases} -\omega^2 \rho_f U_f - \rho_f c_f^2 \partial_x^2 U_f = 0 & \text{in } \Omega_f, \\ U_f = 1 & \text{on } \Gamma_0, \\ \lim_{x \rightarrow \infty} (\partial_x U_f - ik_f U_f) = 0 & \text{on } \Gamma_1. \end{cases} \quad (71)$$

Since the domain equation is unchanged, so is the wave number k_f . The general harmonic solution is also the same, but upon substituting the values of the boundary conditions of (71) the values of A and B change:

$$\begin{cases} U_f|_{\Gamma_0} = A e^{-ik_f L_0} + B e^{ik_f L_0} = 1, \\ \lim_{x \rightarrow \infty} (\partial_x U_f|_{\Gamma_1} - ik_f U_f|_{\Gamma_1}) = 0, \end{cases} \quad (72)$$

which yields

$$\begin{cases} A = 0, \\ B = e^{-ik_f L_0}. \end{cases} \quad (73)$$

Using these values it is possible to transform the solution in the frequency domain back to the time domain:

$$u_f(t, x) = \operatorname{Re}(e^{-i\omega t} U_f(x)) = \operatorname{Re}(e^{-i\omega t} e^{-ik_f L_0} e^{ik_f x}). \quad (74)$$

The initial conditions for the simulation will be

$$u_f(x, 0) = \operatorname{Re}(e^{-ik_f L_0} e^{ik_f x}), \quad (75)$$

$$\partial_t u_f(x, 0) = \operatorname{Re}(-i\omega e^{-ik_f L_0} e^{ik_f x}). \quad (76)$$

The results of the simulation are shown in Fig. 26, and are once again highly matching. On this occasion, since the right boundary is transparent, it is no longer a standing wave, but instead it travels towards the open end. It still maintains its periodicity, since it is a harmonic solution. The physical parameters used in this test case are shown in Tab. 1.

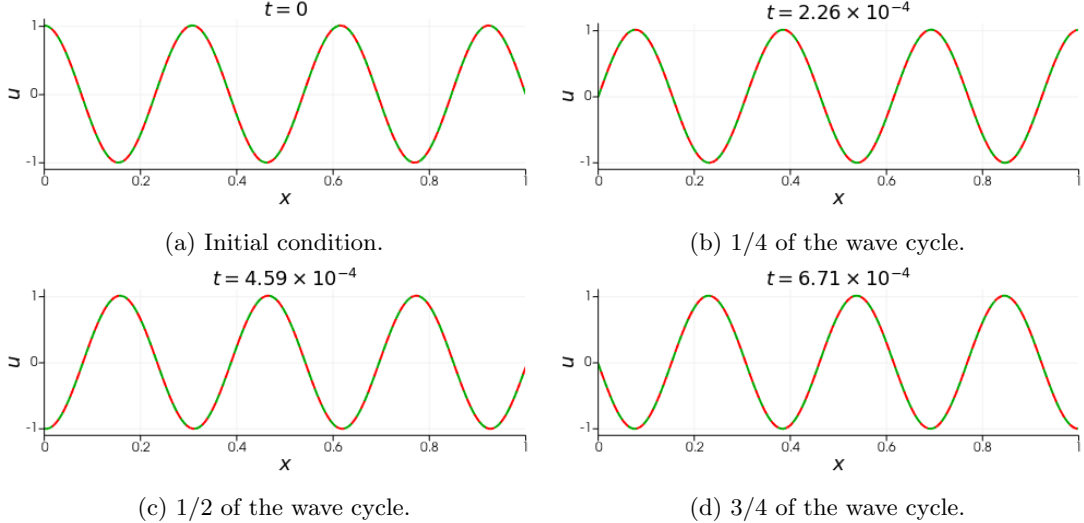


Figure 26: Development of the first wave cycle of the transporting wave given by the initial conditions (75) and (76) on model (\mathcal{P}_2). In red, the simulated solution, in green the exact harmonic solution.

7.3.3 Fluid-Porous Coupled Model with Rigid Boundaries

Next the coupled models are validated. In fluid models, since the variational formulation of disturbed and undisturbed models where the same (compare (\mathcal{P}_1') with (\mathcal{P}_1) or (\mathcal{P}_2') with (\mathcal{P}_2)) the harmonic solution was not a critical test. However, it is in coupled models, since it is the easiest way to test them. Taking model (\mathcal{P}_3), which has a rigid boundary on Γ_1 and both fluid and rigid porous media, it is possible to impose the same boundary time function as before, (62), and transform it into the frequency domain:

$$\begin{cases} -\omega^2 \rho_f U_f - \rho_f c_f^2 \partial_x^2 U_f = 0 & \text{in } \Omega_f, \\ -(\omega^2 \rho_p + i\omega\sigma) \tilde{U}_p - \frac{\rho_p c_p^2}{\phi \gamma_p} \partial_x^2 \tilde{U}_p = 0 & \text{in } \Omega_p, \\ U_f = \tilde{U}_p & \text{on } \Gamma, \\ \rho_f c_f^2 \partial_x U_f = \frac{\rho_p c_p^2}{\phi^2 \gamma_p} \partial_x \tilde{U}_p & \text{on } \Gamma, \\ U_f = 1 & \text{on } \Gamma_0, \\ \tilde{U}_p = 0 & \text{on } \Gamma_1. \end{cases} \quad (77)$$

The characteristic polynomial, as well as the wave number, in the fluid domain is the same as in previous cases, but it is not equal in the porous domain. Solving the characteristic polynomial of the second equation in (77) yields the porous wave number k_p .

$$-\frac{\rho_p c_p^2}{\phi \gamma_p} \lambda^2 - (\omega^2 \rho_p + i\omega\sigma) = 0 \implies \lambda = \pm i \sqrt{\frac{\phi \gamma_p}{\rho_p c_p^2} (\omega^2 \rho_p + i\omega\sigma)} = \pm ik_p. \quad (78)$$

Taking the general solution,

$$\begin{cases} U_f(x) = A_f e^{-ik_f x} + B_f e^{ik_f x} & \text{in } \Omega_f, \\ \tilde{U}_p(x) = A_p e^{-ik_p x} + B_p e^{ik_p x} & \text{in } \Omega_p, \end{cases} \quad (79)$$

and substituting it in the boundary conditions of the Helmholtz problem (77) a linear system is obtained, which can be solved in order to get the parameters. Recalling that $x|_{\Gamma_0} = L_0$, $x|_{\Gamma_1} = L_1$ and defining $x|_{\Gamma} = L$,

$$\begin{bmatrix} e^{-ik_f L} & e^{ik_f L} & -e^{-ik_p L} & -e^{ik_p L} \\ -r_1 e^{-ik_f L} & r_1 e^{ik_f L} & r_2 e^{-ik_p L} & -r_2 e^{ik_p L} \\ e^{-ik_f L_0} & e^{ik_f L_0} & 0 & 0 \\ 0 & 0 & e^{-ik_p L_1} & e^{ik_p L_1} \end{bmatrix} \begin{bmatrix} A_f \\ B_f \\ A_p \\ B_p \end{bmatrix} = \begin{bmatrix} 0 \\ 0 \\ 1 \\ 0 \end{bmatrix}, \quad (80)$$

where

$$r_1 = ik_f \rho_f c_f^2,$$

$$r_2 = ik_p \frac{\rho_p c_p^2}{\phi^2 \gamma_p}.$$

Given a particular solution to this system, the time domain solution is

$$u(t, x) = \begin{cases} \operatorname{Re}(e^{-i\omega t} (A_f e^{-ik_f x} + B_f e^{ik_f x})) & \text{in } \Omega_f, \\ \operatorname{Re}(e^{-i\omega t} (A_p e^{-ik_p x} + B_p e^{ik_p x})) & \text{in } \Omega_p, \end{cases} \quad (81)$$

which means that the initial conditions are

$$u(x, 0) = \begin{cases} \operatorname{Re}(A_f e^{-ik_f x} + B_f e^{ik_f x}) & \text{in } \Omega_f, \\ \operatorname{Re}(A_p e^{-ik_p x} + B_p e^{ik_p x}) & \text{in } \Omega_p, \end{cases} \quad (82)$$

$$\partial_t u(x, 0) = \begin{cases} \operatorname{Re}(-i\omega (A_f e^{-ik_f x} + B_f e^{ik_f x})) & \text{in } \Omega_f, \\ \operatorname{Re}(-i\omega (A_p e^{-ik_p x} + B_p e^{ik_p x})) & \text{in } \Omega_p, \end{cases} \quad (83)$$

The results of the simulation are shown in Fig. 27. Since the rigid boundary has been reinstated, the resulting wave is once again a standing wave. The physical parameters used here are shown in Tab. 2.

Sound speed in fluid	c_f	343 m/s
Fluid density	ρ_f	1.21 kg/m ³
Sound speed in porous	c_p	350 m/s
Porous density	ρ_p	1.5 kg/m ³
Porosity	ϕ	0.5
Specific heat capacity ratio	γ_p	1.4
Flux resistivity	σ	100 N s/m ⁴

Table 2: Physical parameters.

7.3.4 Fluid-Porous Coupled Model with Rigid-Transparent Boundaries

The last model that is able to be checked against an exact solution is the open configuration of the fluid-porous coupling. Much in the same way that for the previous case, using the harmonic solution is

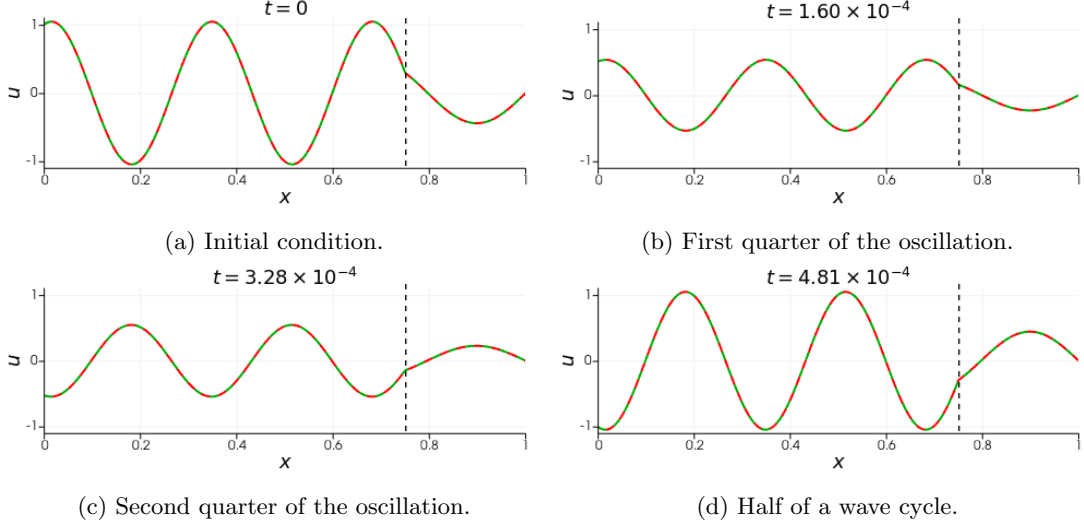


Figure 27: Development of the first wave cycle of the standing wave given by the initial conditions (82) and (83) on model (\mathcal{P}_3) . In red, the simulated solution, in green the exact harmonic solution. The dashed vertical line marks the interface between the fluid domain (to the left) and the porous media (to the right).

the best way to test this model. As has done before, model (\mathcal{P}_4) can be taken to the frequency domain using (62) as boundary displacement function:

$$\begin{cases} -\omega^2 \rho_f U_f - \rho_f c_f^2 \partial_x^2 U_f = 0 & \text{in } \Omega_f, \\ -(\omega^2 \rho_p + i\omega\sigma) \tilde{U}_p - \frac{\rho_p c_p^2}{\phi \gamma_p} \partial_x^2 \tilde{U}_p = 0 & \text{in } \Omega_p, \\ U_f = \tilde{U}_p & \text{on } \Gamma, \\ \rho_f c_f^2 \partial_x U_f = \frac{\rho_p c_p^2}{\phi \gamma_p} \partial_x \tilde{U}_p & \text{on } \Gamma, \\ U_f = 1 & \text{on } \Gamma_0, \\ -i\omega \tilde{U}_p + \frac{\rho_p c_p^2}{\rho_f c_f \phi^2 \gamma_p} \partial_x \tilde{U}_p & \text{on } \Gamma_1. \end{cases} \quad (84)$$

Both wave numbers, k_f and k_p , are the same wave numbers that were found earlier, so it is possible to directly substitute the general solution (79) into the boundary conditions of (84) to formulate the linear system. That allows finding the general solution's parameters given by

$$\begin{bmatrix} e^{-ik_f L} & e^{ik_f L} & -e^{-ik_p L} & -e^{ik_p L} \\ -r_1 e^{-ik_f L} & r_1 e^{ik_f L} & r_2 e^{-ik_p L} & -r_2 e^{ik_p L} \\ e^{-ik_f L_0} & e^{ik_f L_0} & 0 & 0 \\ 0 & 0 & -i(r_3 + \omega) e^{-ik_p L_1} & -i(r_3 - \omega) e^{ik_p L_1} \end{bmatrix} \begin{bmatrix} A_f \\ B_f \\ A_p \\ B_p \end{bmatrix} = \begin{bmatrix} 0 \\ 0 \\ 1 \\ 0 \end{bmatrix}, \quad (85)$$

where r_1 and r_2 are identical to the coefficients defined previously, and

$$r_3 = k_p \frac{\rho_p c_p^2}{\rho_f c_f^2 \phi^2 \gamma_p}.$$

Although the values of the coefficients differ, the solution of this system in the time domain corresponds to (81) using the solution of (85) as coefficients, and in the same fashion, (82) and (83) will be the initial conditions for the simulation. The results of the test can be observed in Fig. 28. The behavior of this

wave is difficult to describe, but it involves both traveling and shrinking, although never reaching the zero displacement in the entire spatial domain at the same time. A phase shift is observed between the fluid and the porous media. This complex behavior is the result of partial reflections, since as viewed from the porous material, the incoming wave is partially reflected and partially refracted, and the second part is reflected and refracted again at the right boundary, unlike in the previous model where it was perfectly reflected and no energy was lost. It could be said that this behavior is a mixture between a standing and a traveling wave. It is of course still periodic. The physical parameters used in Fig. 28 are shown in Tab. 2.

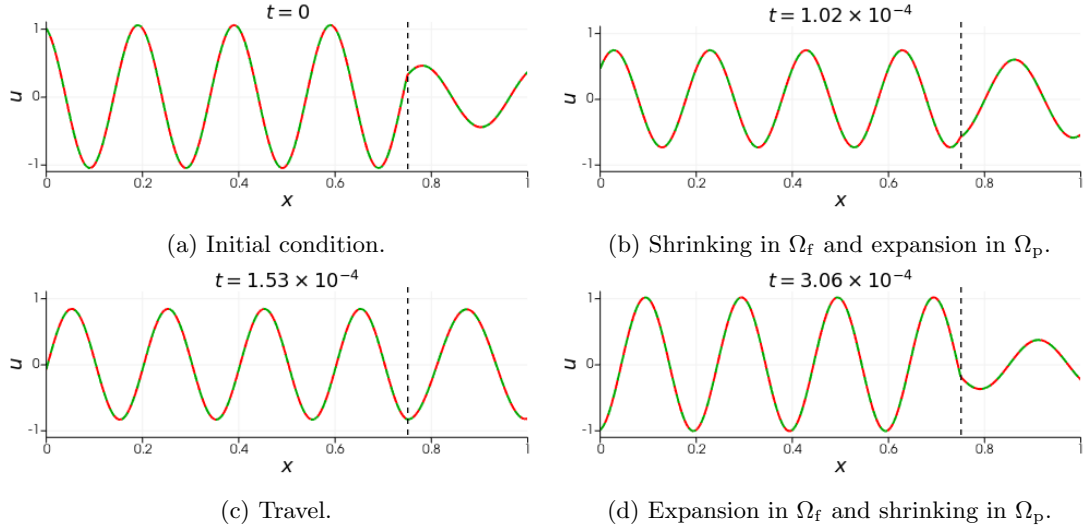


Figure 28: Development of the first half of a wave cycle of the standing wave given by the initial conditions (82) and (83) on model (\mathcal{P}_4). In red, the simulated solution, in green the exact harmonic solution. The dashed vertical line marks the interface between the fluid domain (to the left) and the porous media (to the right).

7.4 Umnova’s Low Frequency Approximation Comparison

For the first time in the development of the project it appears a model that is too complex to be able to offer an exact solution to, even for a simple particular case. The difficulty arises from the fact that porous model is no longer rigid but poro-elastic, meaning that thermal and elastic losses must be considered. Instead, the validation of the model is performed through the data included in Umnova’s paper (see Fig. 1 in [52]). First, the data is extracted from the graph, and then, using the same acoustic source, the “Mexican Hat” defined by (86), the simulation of model (\mathcal{P}_5) is run. Finally the results are compared. Recall that the entire domain is porous, and in order to lessen the effects of the approximation discussed in section 4.3.1, $\Omega_p = [0, 3]$ is chosen, although the furthest sampling point is $x = 1$. The “Mexican Hat” equation is

$$g(t) = \left(1 - \omega^2(t - t_0)^2\right) \exp\left(-\frac{\omega^2(t - t_0)^2}{2}\right), \quad (86)$$

with the parameters used in the paper as well, $\omega = 50$, and $t_0 = 0.1$. In order to transform the displacements to pressures so that a comparison between the simulation’s results and the available data is viable, the relation between pressures and displacements given by the model, (16), is used. The result of the comparison is shown in Fig. 29. The physical parameters of the solution are taken from the paper and are the ones reflected in Tab. 3.

Sound speed in fluid	c_f	343 m/s
Fluid density	ρ_f	1.21 kg/m ³
Porosity	ϕ	0.36
Specific heat capacity ratio	γ_p	1.4
Flux resistivity	σ	27888 N s/m ⁴
Tortuosity	α_∞	1.89

Table 3: Physical parameters for the low frequency model.

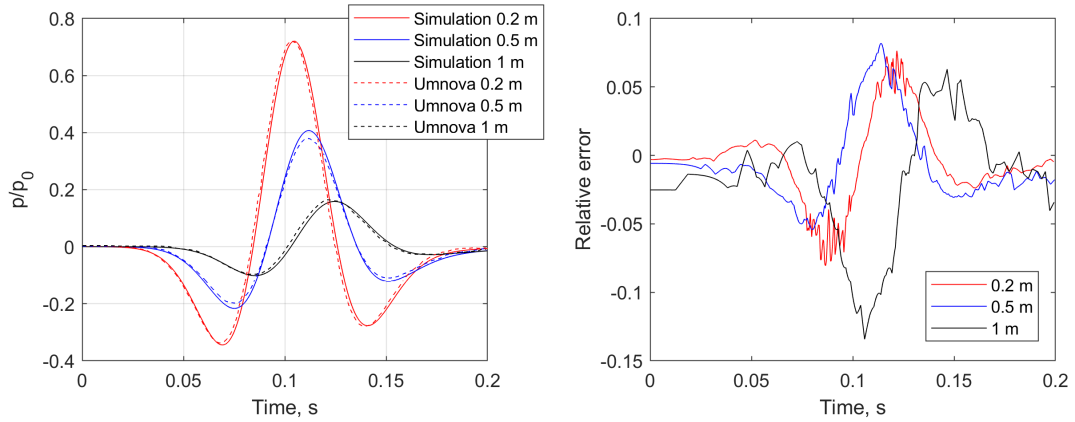


Figure 29: Comparison of the simulated results by model (P_5) (in solid lines), with the data presented in Umnova 2009 [52] (in dashed lines). Red lines are sampled at $x = 0.2$, blue lines at $x = 0.5$ and black lines are sampled at $x = 1$.

8 Numerical Results

After developing and validating the models, the goal is to find out if DMD is an effective predictor of such models, or in which cases it is. The advantage of using DMD in regards to the computation time is tremendous, specially in more complex models, since they radically increase the simulation time but DMD is not affected by the complexity of the model running underneath the data. In the following pages the conclusions extracted from numerous tests are presented. The particular results shown are representative of the behavior exhibited by other models of the same characteristics as well, and the remaining results have not been included in the interest of clarity.

8.1 Harmonic Reconstruction

Firstly, the simplest case is introduced. The DMD method is specially well behaved in periodic data, so the first step will be simply to reconstructing harmonic solutions. Using an truncation rank of 2 ($r = 2$), it is possible to reconstruct the solutions with a very small error, as shown in Fig. 31. Note the color scale of the error. In Fig. 30 it is clearly shown that the DMD modes, defined in (53), properly capture the porous domain, which is manifested by the reduced amplitude on the rightmost half-wave, or by the “unfocused” vertical band on the right of the reconstructions of Fig. 31 and Fig. 33. The dynamics are given by $e^{\Omega t} b$ in (54). Compare the modes with the actual wave form in Fig. 27 to see the similarities. In these graphs, the horizontal axis represents the spatial dimension x , the vertical axis the temporal dimension t , and the color axis represents the displacement u . The parameters used are shown in Tab. 4 and Tab. 5.

Sound speed in fluid	c_f	343 m/s
Fluid density	ρ_f	1.21 kg/m ³
Sound speed in porous	c_p	350 m/s
Porous density	ρ_f	1.5 kg/m ³
Porosity	ϕ	0.5
Specific heat capacity ratio	γ_p	1.4
Flux resistivity	σ	100 N s/m ⁴

Table 4: Physical parameters.

Time step	Δt	1.46×10^{-5} s
Space step	Δx	5×10^{-3} m
Truncation rank	r	2
<i>d</i> parameter in HODMD	d	5

Table 5: Discretization and ROM parameters.

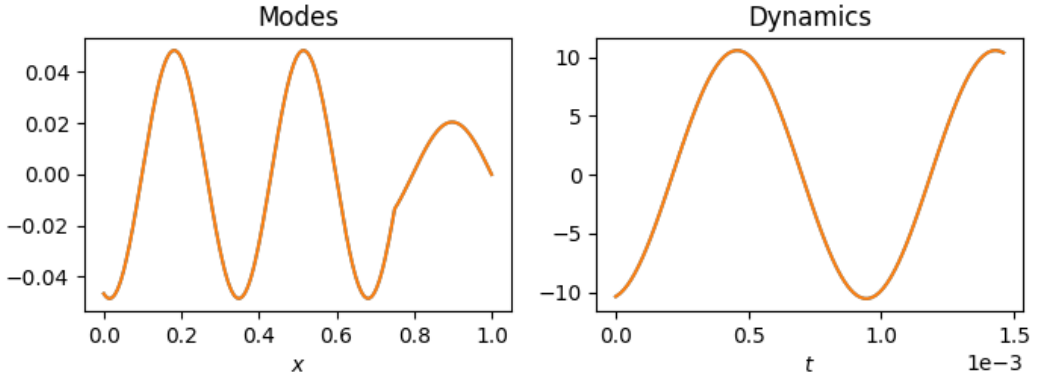


Figure 30: Two overlapping DMD modes (to the left) and dynamics (to the right) of the reconstruction shown in Fig. 31.

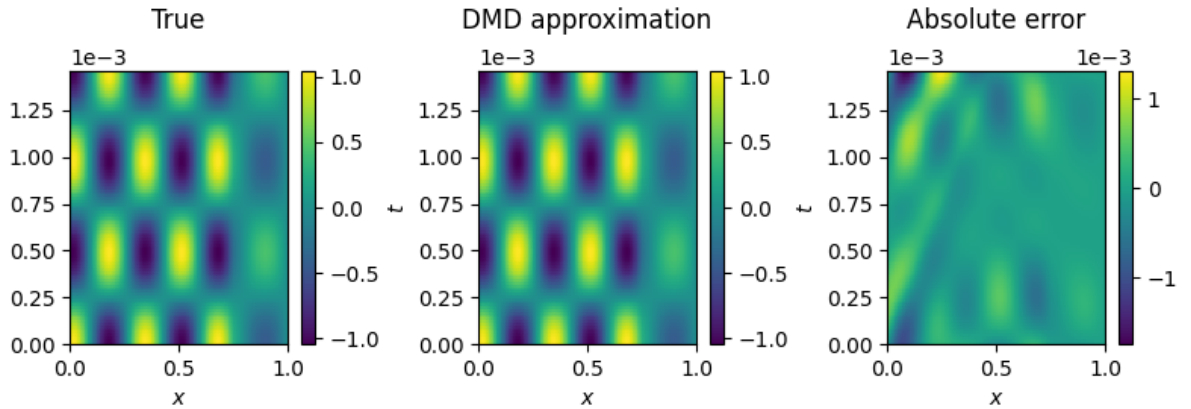


Figure 31: Reconstruction of simulated harmonic solution of model (\mathcal{P}_3).

The same can be done with model (\mathcal{P}_4), where there exists a transparent boundary on the right. In Fig. 33 it becomes apparent the traveling and shrinking in the fluid domain discussed in the validation section.

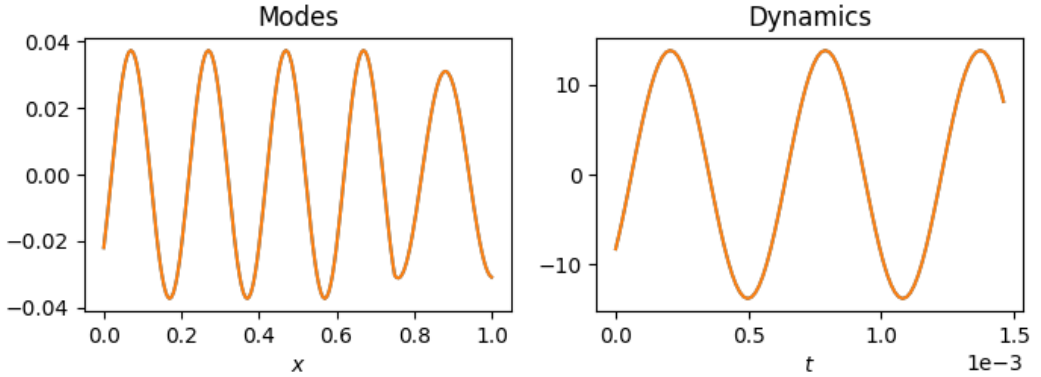


Figure 32: Two overlapping DMD modes (to the left) and dynamics (to the right) of the reconstruction shown in Fig. 33.

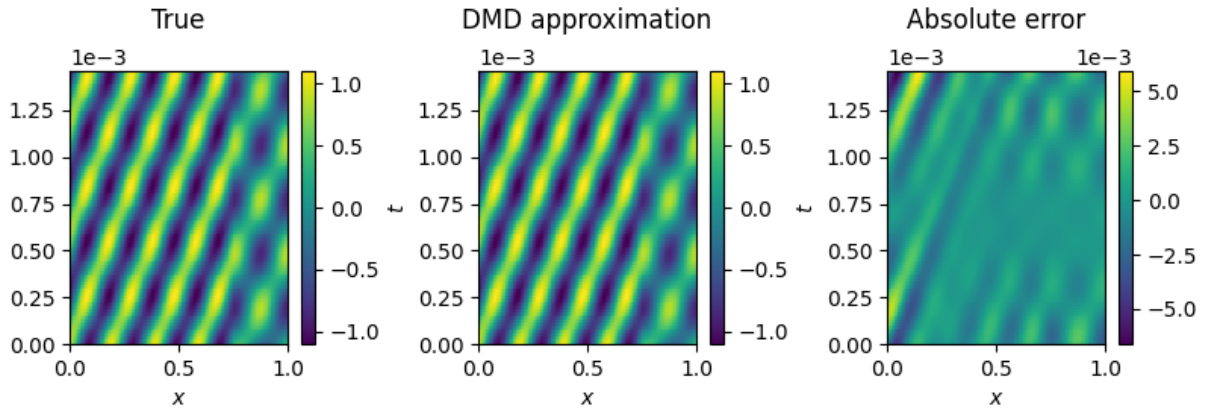


Figure 33: Reconstruction of simulated harmonic solution of model (\mathcal{P}_4).

These reconstructions show that DMD is able to extract modes and reconstruct an approximated data set in the original dimension, but that is nothing special since other methods such as SVD are already capable of that and in fact are slightly more efficient at it. The capability needed from DMD is that it is also able to predict the evolution of the data further into the future.

8.2 Harmonic Predictions

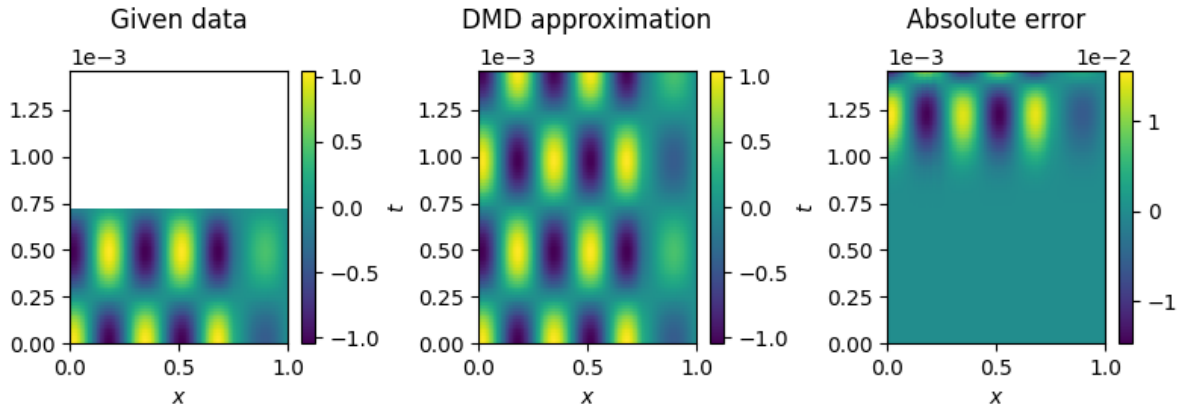
Using the same source data, only a fraction of it will be fed to the method. DMD will reconstruct it and then the absolute error will be found by comparing the prediction to the ground truth. A decrease in the amount of snapshots given to the method will be used in order to showcase the limits for this kind of problem. The results for the rigid boundary model are shown in Fig. 34. Similar results can be obtained for models with transparent Γ_1 as well as fluid models, but the harmonic solution used in the validation of model (\mathcal{P}_3) will be used as an example.

8.2.1 Effects of the Number of Snapshots Given

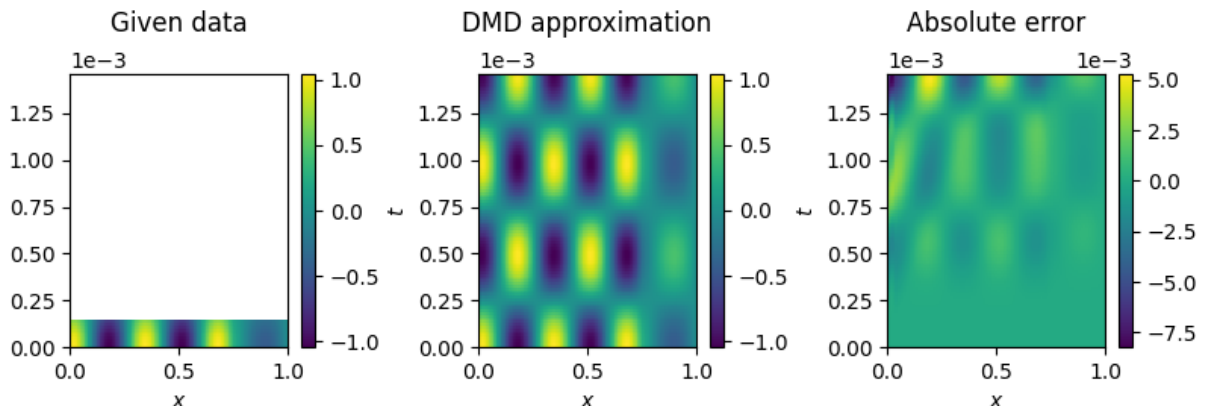
The error seems to be going down as the number of snapshots is limited. This is due to the noise of the data, that becomes greater as the simulation advances, which can, on occasions, throw the dynamics off track. The mesh used in this particular simulation was quite thick, with $\Delta x = 5 \times 10^{-3}$ and $\Delta t = 1.46 \times 10^{-5}$. Nonetheless, note that DMD is able to reconstruct 100 snapshots with a maximum error of about 0.8% from just three snapshots. However, it is not able to infer the dynamics from only two snapshots. The physical parameters from Tab. 4 were used, and the discretization and ROM parameters are shown in Tab. 7. The truncation rank was decided autonomously by the software, and since $d = 1$, a standard DMD was performed.

Time step	Δt	1.46×10^{-5} s
Space step	Δx	5×10^{-3} m
Truncation rank	r	auto
d parameter in HODMD	d	1

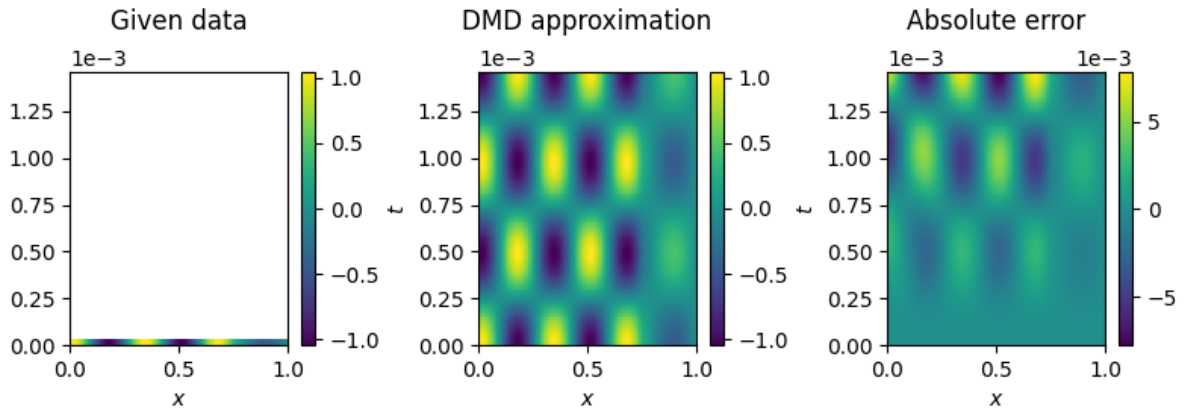
Table 6: Discretization and ROM parameters.



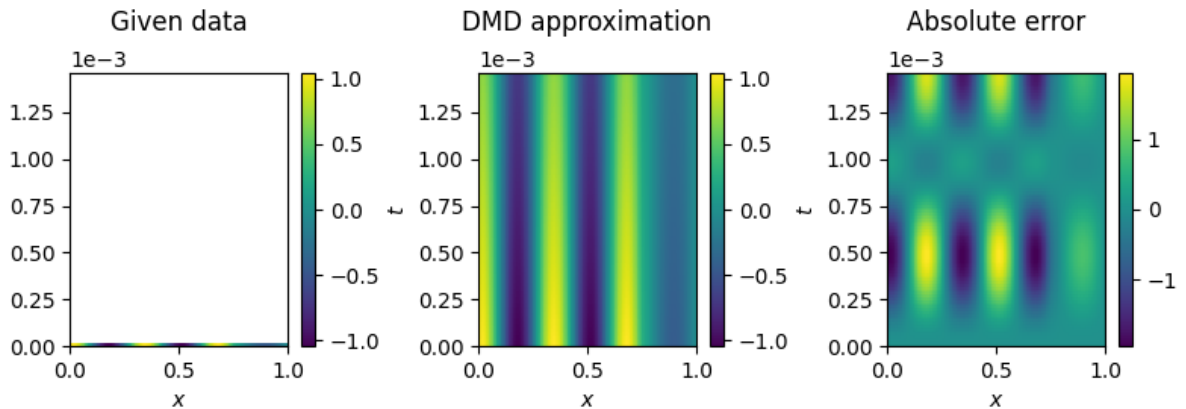
(a) 50 snapshots.



(b) 10 snapshots.



(c) 3 snapshots.



(d) 2 snapshots.

Figure 34: Effects of reducing the given snapshots in the reconstruction of harmonic data modeled by (\mathcal{P}_3) .

8.2.2 Effects of the Discretization Size

The error can be reduced if the mesh used is finer or if instead of the numerical data the exact solution is used, even if the mesh size is kept the same. In Fig. 35 a discretization of $\Delta x = 2.5 \times 10^{-3}$ and $\Delta t = 7.29 \times 10^{-6}$ is used, and although only three snapshots are given too, which means that the collected data covers a much smaller time space (4.38×10^{-5} versus 2.19×10^{-5} , exactly half), the maximum error goes down to about 0.2%. In Fig. 36 although the mesh is as rough as before, since the numerical noise is non-existent, the error drops to basically zero.

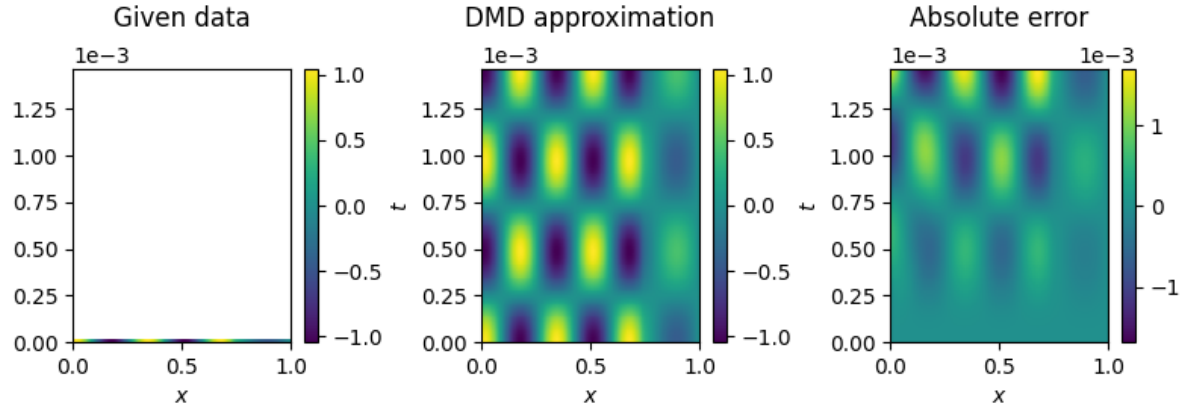


Figure 35: Reconstruction of harmonic data modeled by (\mathcal{P}_3) using a finer mesh.

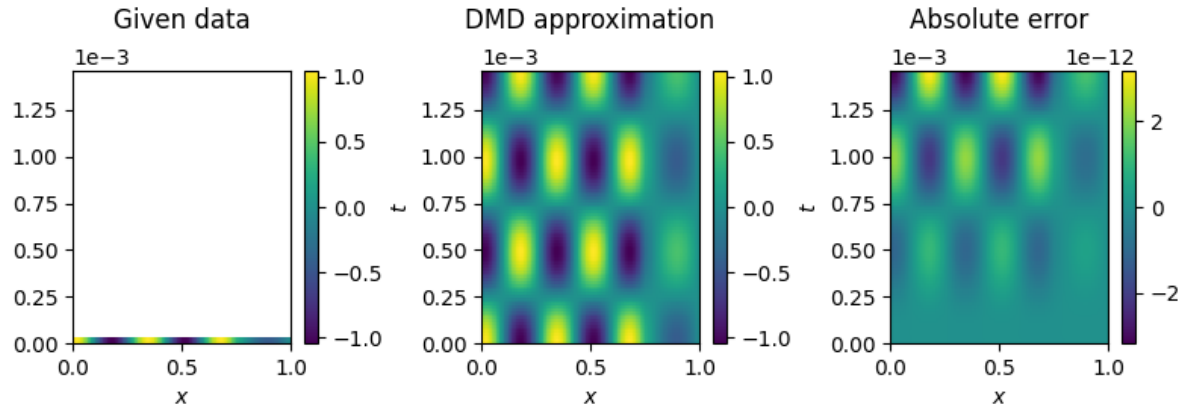
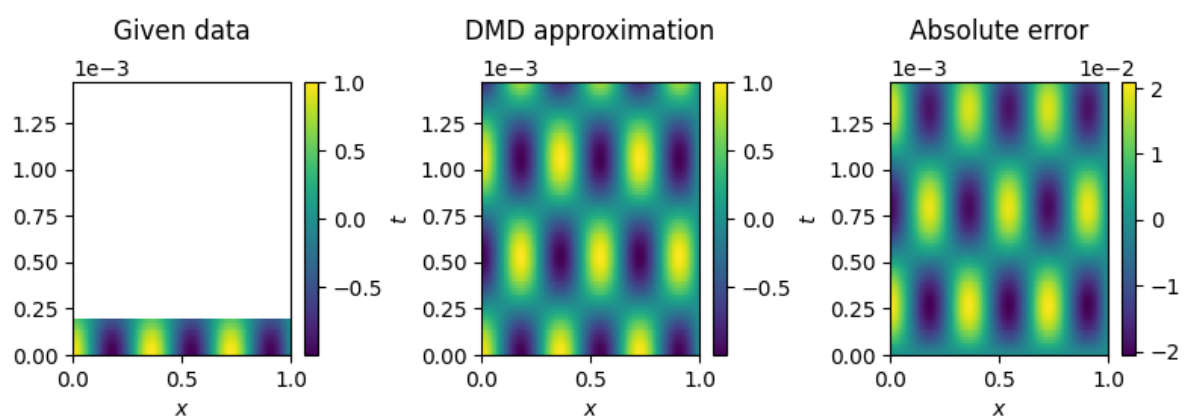
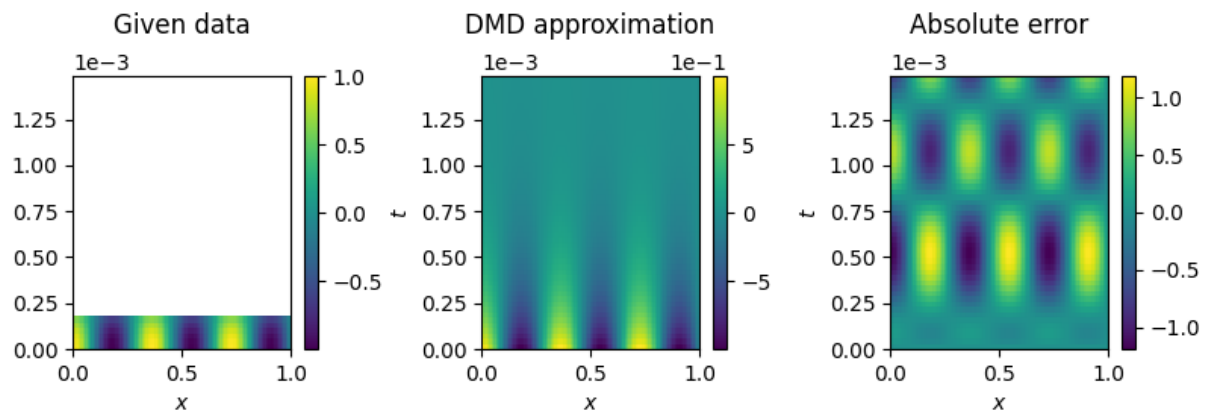
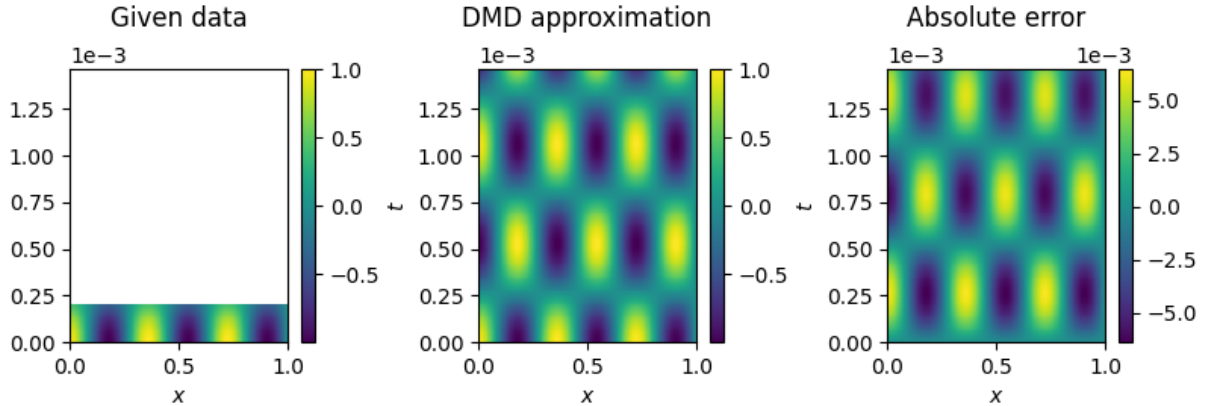


Figure 36: Reconstruction of the exact harmonic data modeled by (\mathcal{P}_3) . Note the color scale.

Keeping the sampling time static and varying the mesh size has a similar effect, the smaller finer the mesh the better the reconstruction. In Fig. 37 the sampling time has been fixed in $t \in [0, 2 \times 10^{-3}]$. The physical parameters used are the ones shown in Tab. 4. The DMD truncation rank was decided autonomously by the software, the parameter d was set to $d = 5$, and the discretization step sizes are shown for each case.



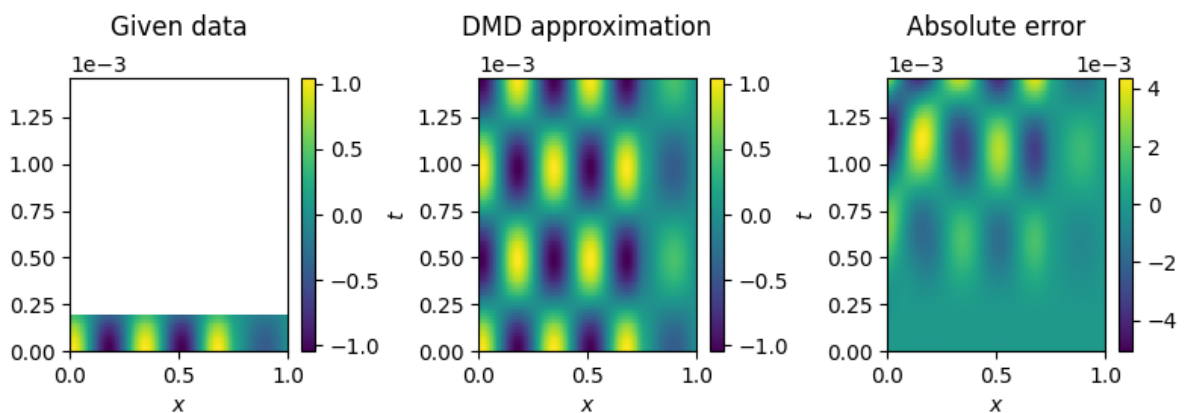


(c) $\Delta x = 2.5 \times 10^{-3}$ and $\Delta t = 7.29 \times 10^{-6}$.

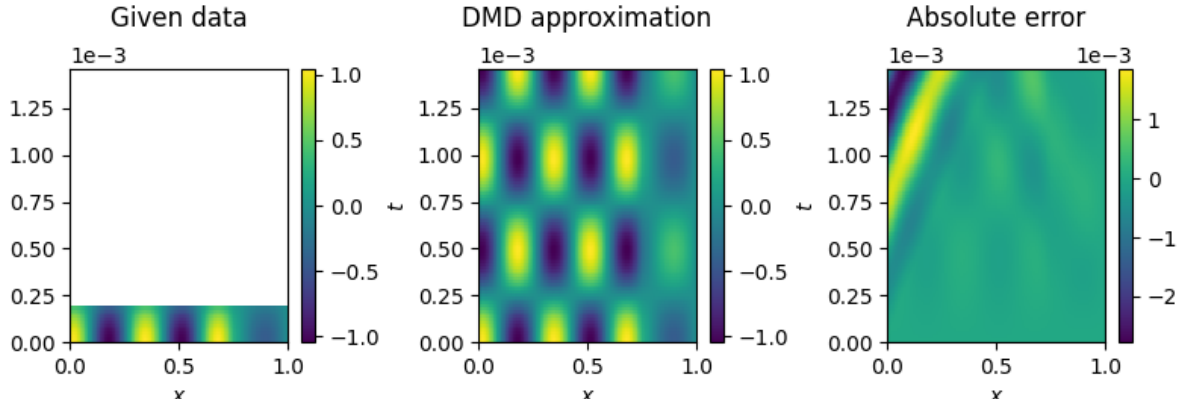
Figure 37: Effects of reducing the size of the discretization in the reconstruction of harmonic data modeled by (\mathcal{P}_3) with fixed time sampling period.

8.3 DMD vs. HODMD

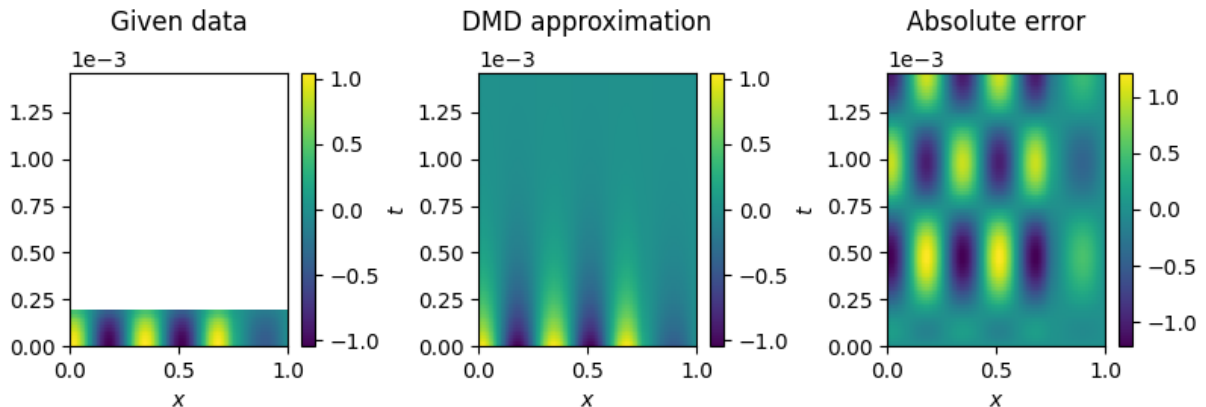
There exist a number of variations of the standard DMD. One of them, HODMD, deals with higher order data by decomposing it into d spatio-temporal structures. The standard DMD can be understood as a particularization of HODMD where $d = 1$. Choosing a correct value of this parameter can determine the success of the prediction or reconstruction. For instance, observing Fig. 38, if the parameter is too small and a simple DMD is performed, the error can be reduced, but if it is too big the coherence might be lost and the results might be even worse. For this reason it is important to choose a correct parameter for each case. The ideal value depends on the underlying dynamics of the system, but typically it should not be too close to either 1 or the number of snapshots. In this case 14 snapshots were used, and both $d = 1$ and $d = 13$ yield a poor result, while $d = 7$ performs much better, as expected. Further discussion can be found in [30]. The parameters used are reflected in Tab. 4 and Tab. 5 with the exception of d , which is varied and defined for each figure individually.



(a) $d = 1$ (standard DMD).



(b) $d = 7$.



(c) $d = 13$.

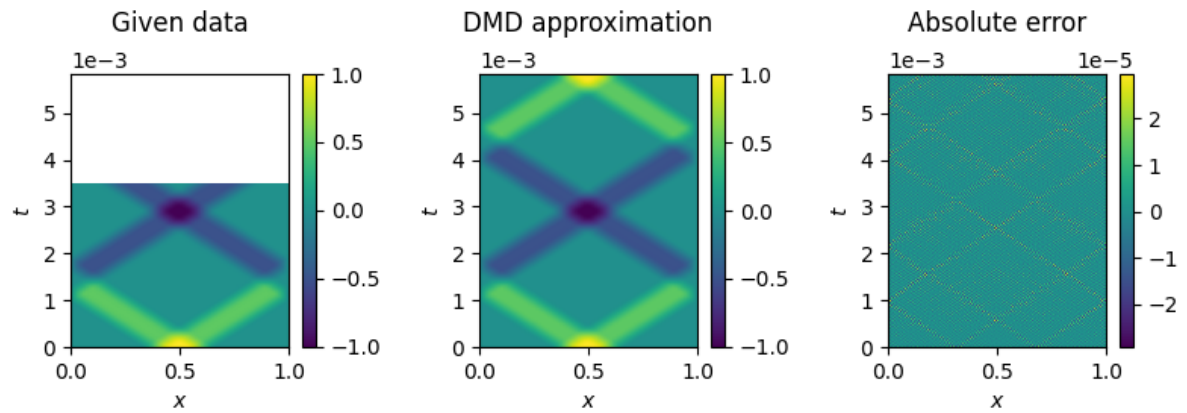
Figure 38: Effects of the parameter d in the HODMD method in a solution modeled by (\mathcal{P}_3) .

8.4 Periodic Impulses

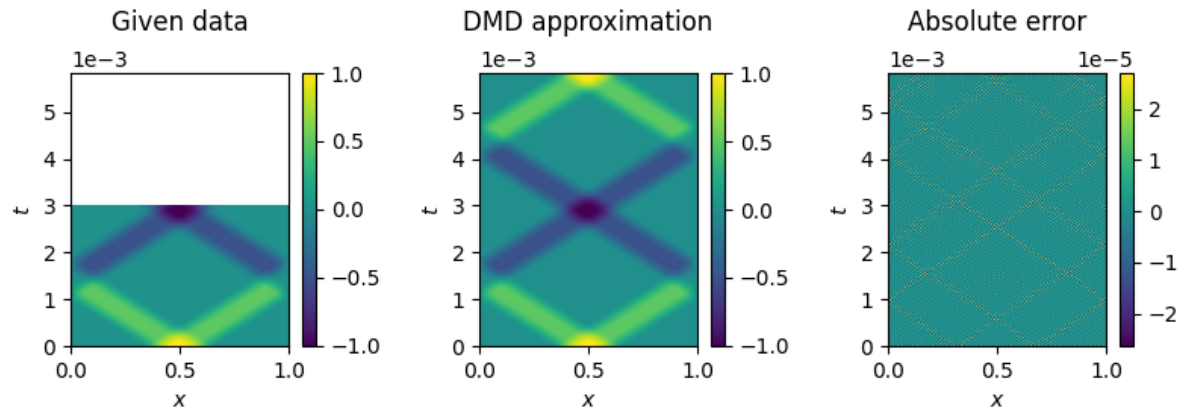
As stated before, DMD shines on periodic models. In general impulse responses are not periodic, but under certain circumstances they can become periodic (see the validation of model (\mathcal{P}_1)). By gradually decreasing the number of snapshots available to the method it becomes evident that having data over an entire period is critical to the success of the method in this situation (Fig. 39), unlike in harmonic oscillations, where a minimal amount of snapshots were sufficient. The physical parameters are shown in Tab. 4, and the discretization and ROM parameters are reflected in Tab. 7.

Time step	Δt	5.83×10^{-6} s
Space step	Δx	2×10^{-3} m
Truncation rank	r	100
d parameter in HODMD	d	5

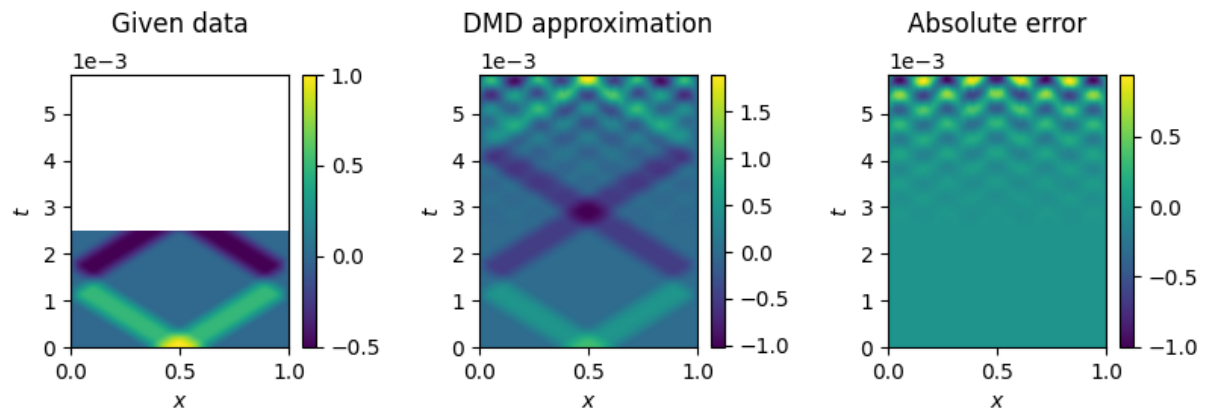
Table 7: Discretization and ROM parameters.



(a) Over a period.



(b) One period.



(c) Slightly under a period.

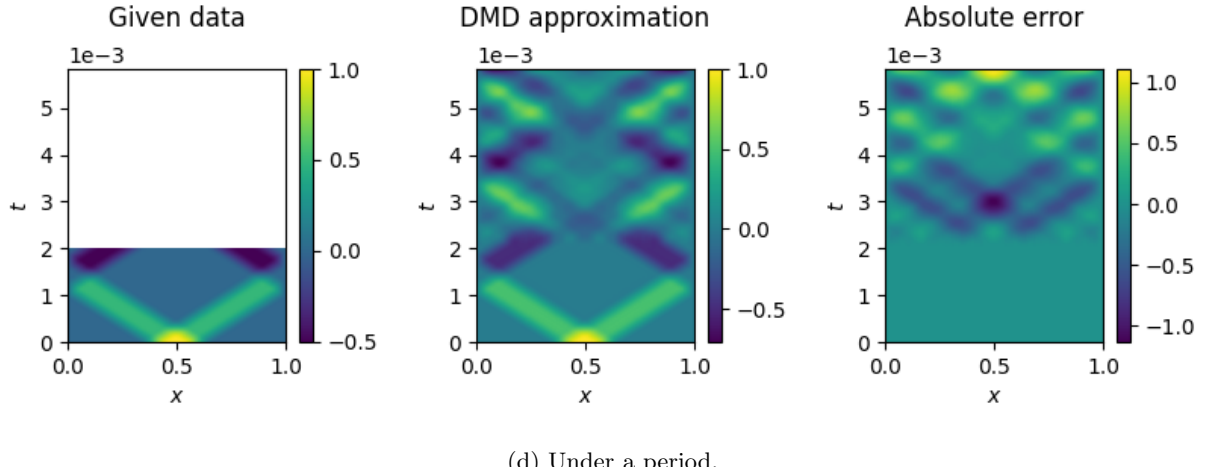


Figure 39: Effects of the number of snapshots given in periodic impulses in a solution modeled by (\mathcal{P}'_1) .

8.4.1 Effects of the DMD Rank

One of the main characteristics of the DMD method is that it is a reduced order method, which means that it solves a simplified version of the problem. In particular, the rank of the method defines how simplified the reduced problem is. It represents the amount of modes used in the reconstruction or prediction, so changing it can have great effects on the result. If the rank is too low the reconstruction will not capture all the modes, and if the rank is too high it will capture a greater degree of numerical noise, which although it reduces the error, it might not align well with a given objective.

Having a high truncation rank r is especially important in solutions to impulses, since a translating wave theoretically can only be recreated perfectly by infinitely many modes (or as many modes as spatial sample points in practice), whereas harmonic solutions can be perfectly captured by just two modes. Fig. 40 shows that the spatial modes (53) elapse the entire domain while the temporal dynamics ($e^{\Omega t} b$ in equation (54)) are a lot more organized.

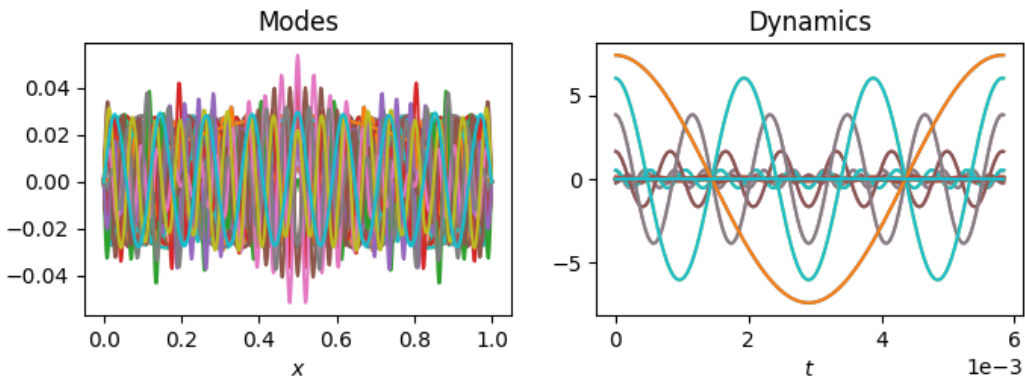


Figure 40: DMD modes (to the left) and dynamics (to the right) of the reconstruction shown in Fig. 41.

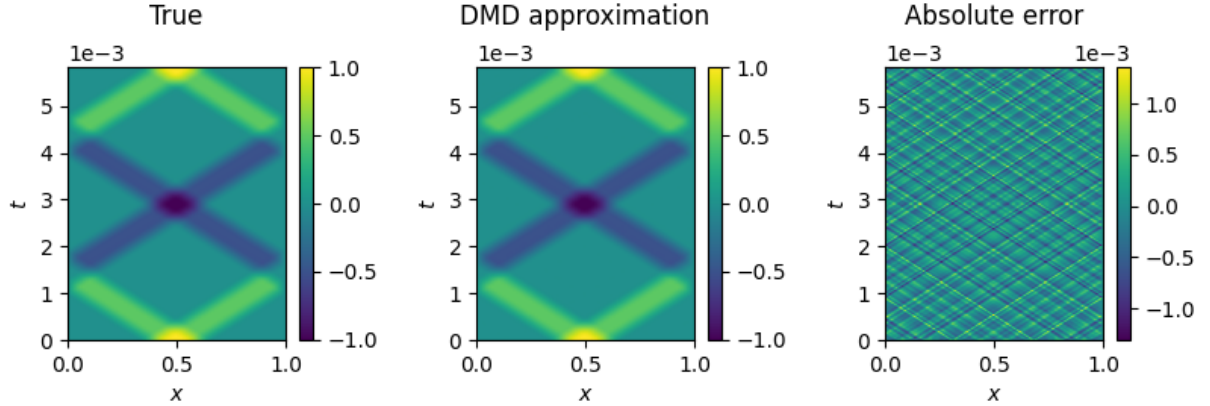
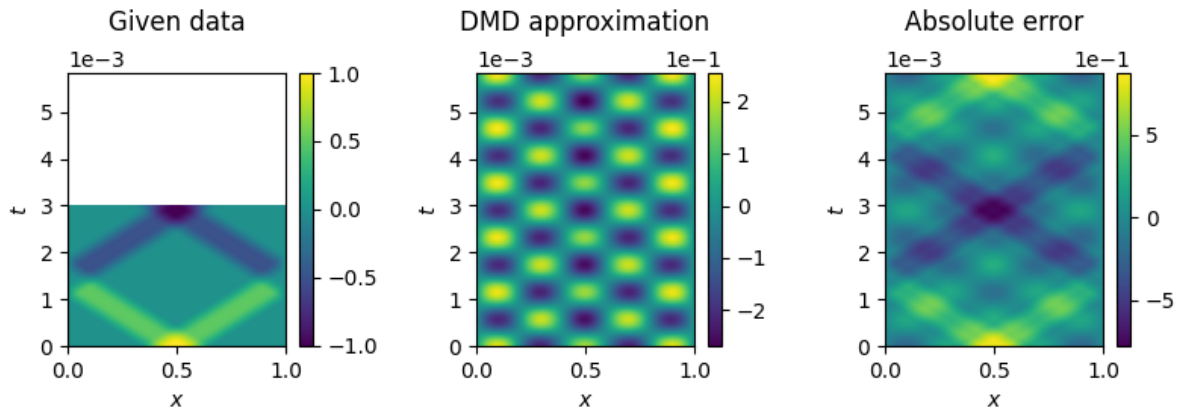


Figure 41: Reconstruction of an impulse response modeled by (\mathcal{P}'_1) .

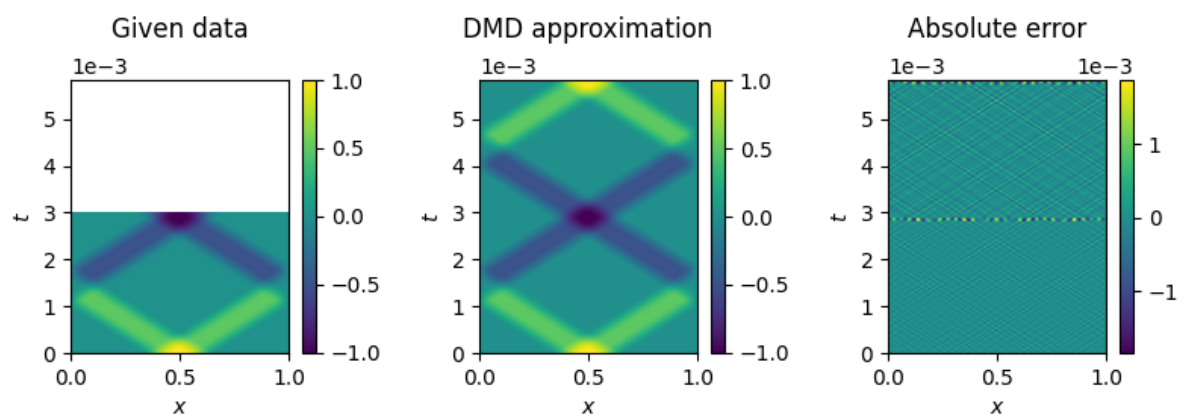
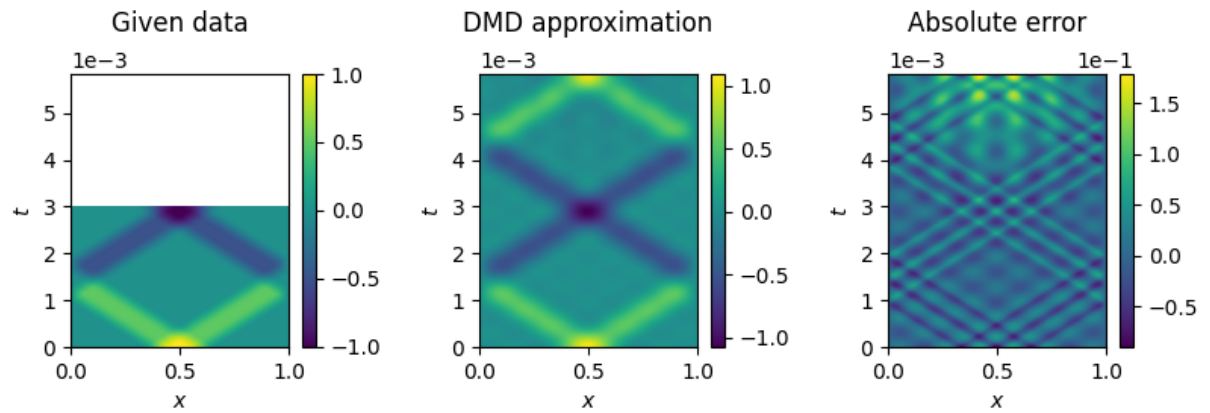
All of these modes together, 50 in this case, are able to approximate the solution, but in fact the lack of sufficient modes can become very noticeable, as shown in Fig. 42. The higher the rank goes the smaller the error becomes. This is not necessarily true for solutions with a finite amount of true modes like the harmonic solutions that were tested before. The physical parameters used are shown in Tab. 4, and the discretization and ROM parameters are recorded in Tab. 8. The truncation rank r is shown for each figure individually.

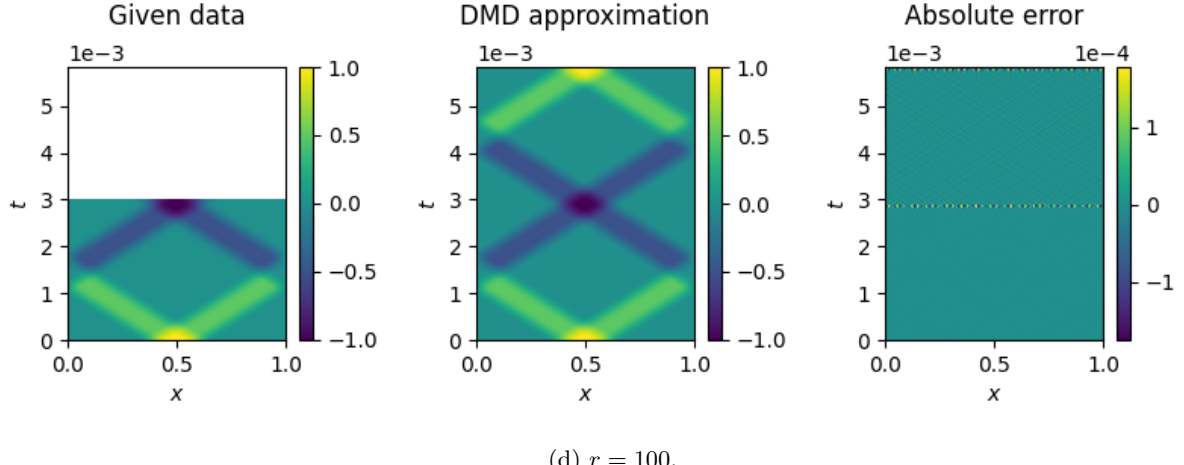
Time step	Δt	5.83×10^{-6} s
Space step	Δx	2×10^{-3} m
d parameter in HODMD	d	30

Table 8: Discretization and ROM parameters.



(a) $r = 5$.





(d) $r = 100$.

Figure 42: Effects of the DMD rank in periodic impulses in a solution modeled by (\mathcal{P}'_1) .

8.5 Non-Periodic Impulses

It has been found that the DMD method works very well with periodic data of any kind, as long as basic requirements for each case are met, but the interest of the project lies in finding out if this success can be extended to non-periodic data. It has been found that it is possible to reconstruct any given data, since this is easily achieved by the internal SVD, but it is completely unable to make any kind of prediction about the future. This is evident in Fig. 43, where high frequency data is used, and in Fig. 44 where low frequency data is utilized. Changing the method's parameters does not seem to have any effect on the success of the prediction. The physical parameters used for the high and low frequency responses are shown in Tab. 4 and Tab. 9 respectively, and the discretization and ROM parameters are shown in Tab. 10 and Tab. 11, high and low frequency respectively.

Sound speed in fluid	c_f	343 m/s
Fluid density	ρ_f	1.21 kg/m ³
Porosity	ϕ	0.36
Specific heat capacity ratio	γ_p	1.4
Flux resistivity	σ	27888 N s/m ⁴
Tortuosity	α_∞	1.89

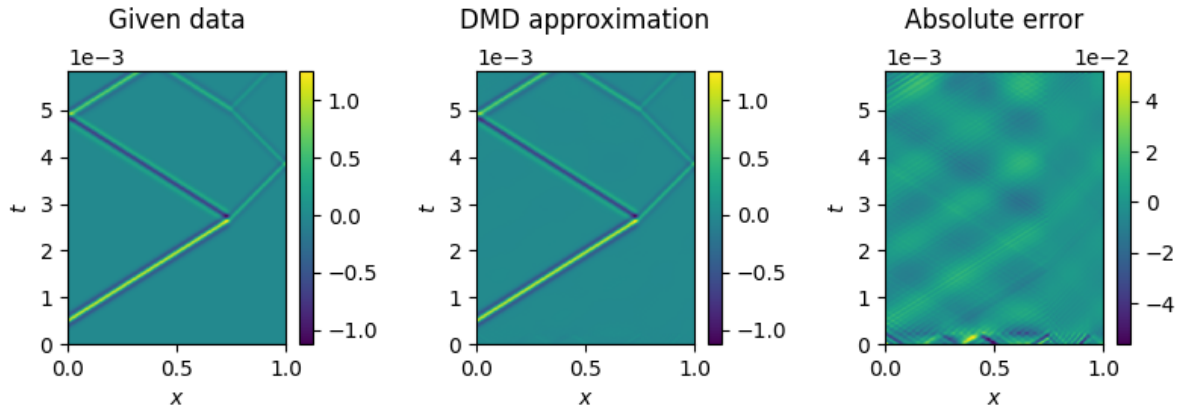
Table 9: Physical parameters for the low frequency model.

Time step	Δt	7.29×10^{-6} s
Space step	Δx	2.5×10^{-3} m
Truncation rank	r	100
d parameter in HODMD	d	5

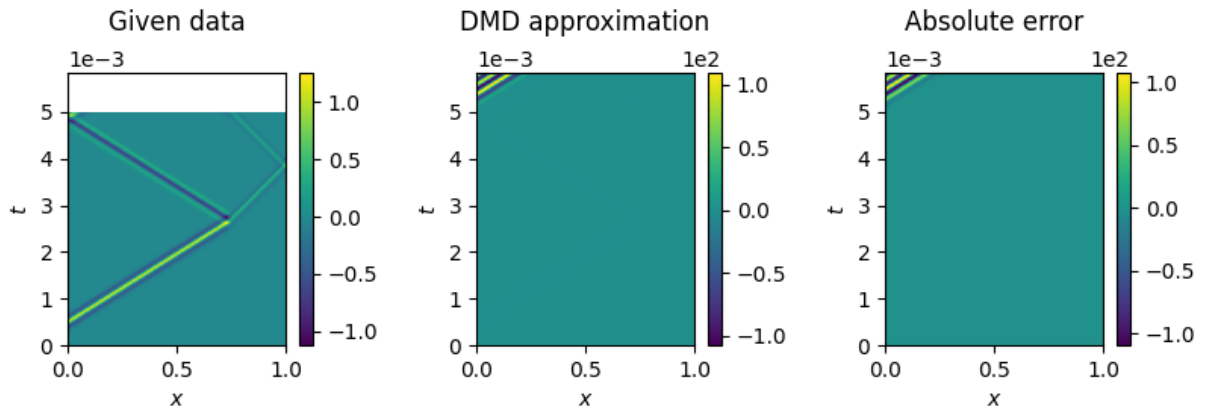
Table 10: Discretization and ROM parameters for the high frequency model.

Time step	Δt	5.83×10^{-5} s
Space step	Δx	2×10^{-2} m
Truncation rank	r	100
d parameter in HODMD	d	5

Table 11: Discretization and ROM parameters for the low frequency model.

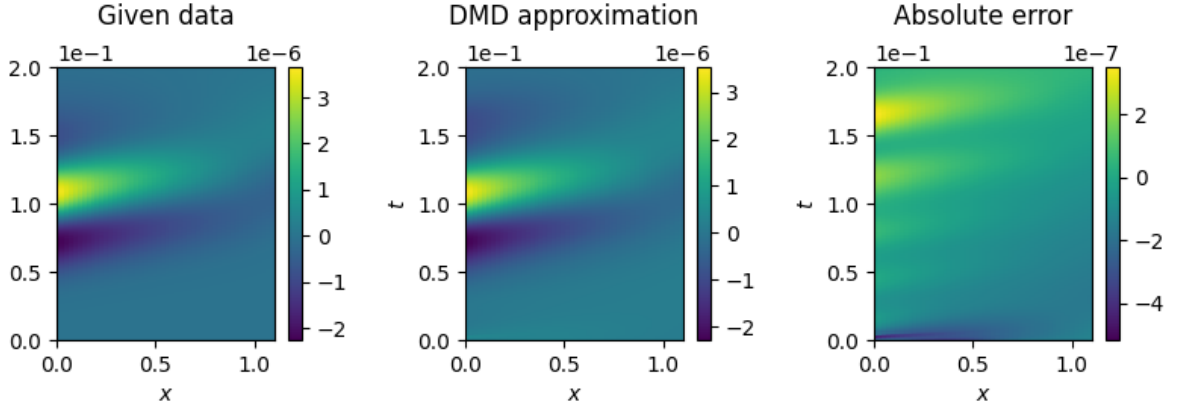


(a) Reconstruction.

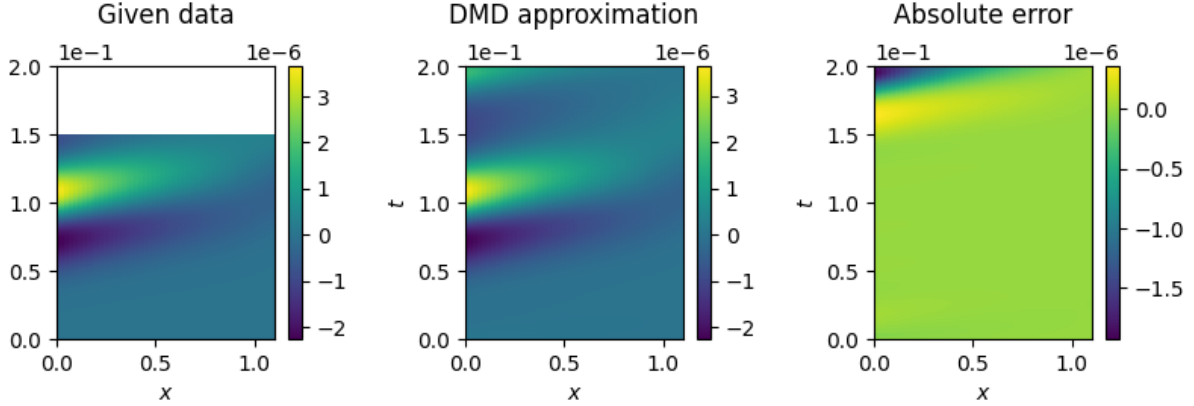


(b) Prediction.

Figure 43: High frequency non-periodic impulses modeled by (\mathcal{P}_3) .



(a) Reconstruction.



(b) Prediction.

Figure 44: Low frequency non-periodic impulses modeled by (\mathcal{P}_6) .

8.6 Simulation Mixing

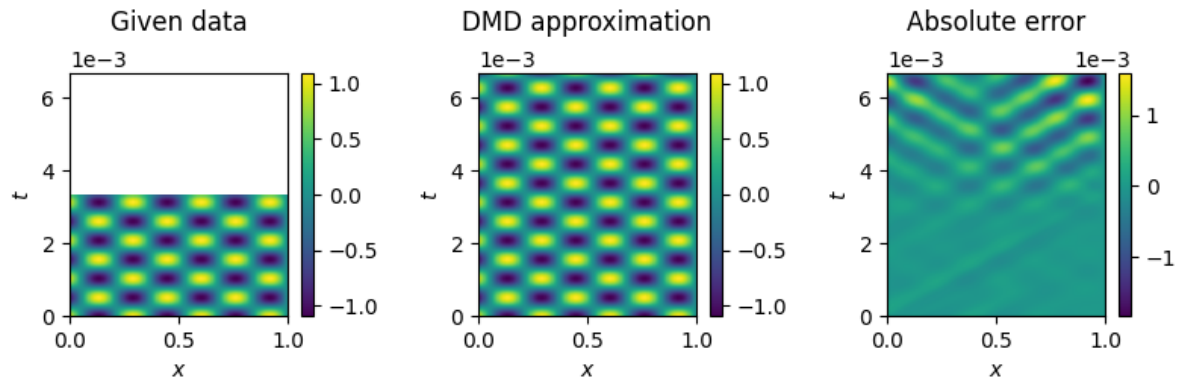
There was also an attempt to mix similar simulation results in order to improve predictions. The idea was that a slight parameter variation in the simulations, something like a slight change in fluid density or the speed of sound, would retain the qualities of the solution, so by running a complete simulation with a set of base parameters and then mixing its final snapshots with the first snapshots of the other simulation better predictions would be obtained than with the few snapshots of the second model alone. It turns out that this is not the case, and due to the abrupt change the method is unable to make any kind of predictions. In Fig. 45, Model 2 uses the physical parameters shown in Tab. 4 and Model 1 uses the same except that $c_f = 300$. The discretization and ROM parameters used for Model 1 and 2 are displayed in Tab. 12 and Tab. 13 respectively.

Time step	Δt	8.33×10^{-6} s
Space step	Δx	2.5×10^{-3} m
Truncation rank	r	5
d parameter in HODMD	d	5

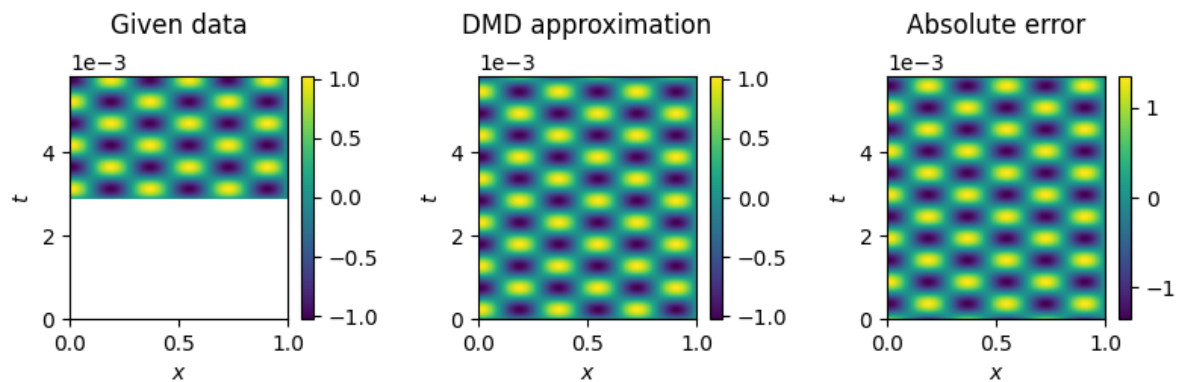
Table 12: Discretization and ROM parameters of Model 1.

Time step	Δt	7.29×10^{-6} s
Space step	Δx	2.5×10^{-3} m
Truncation rank	r	5
d parameter in HODMD	d	5

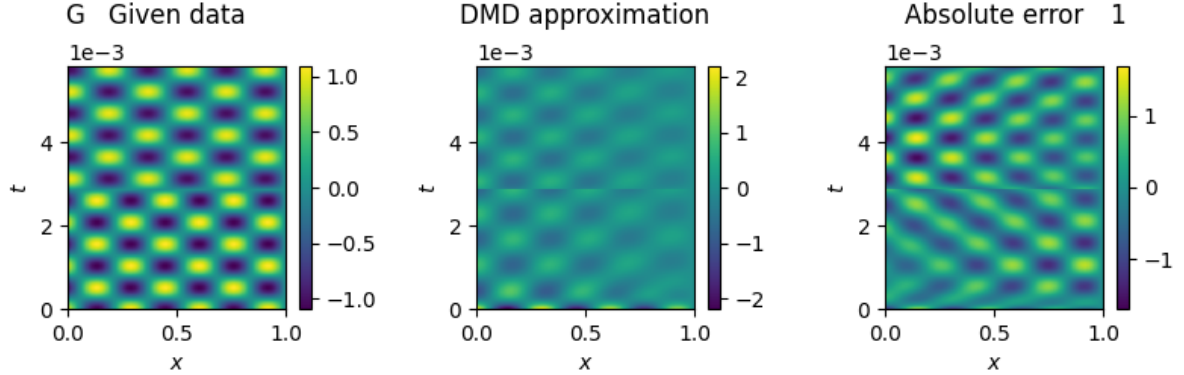
Table 13: Discretization and ROM parameters of Model 2.



(a) Model 1 data.



(b) Model 2 data.

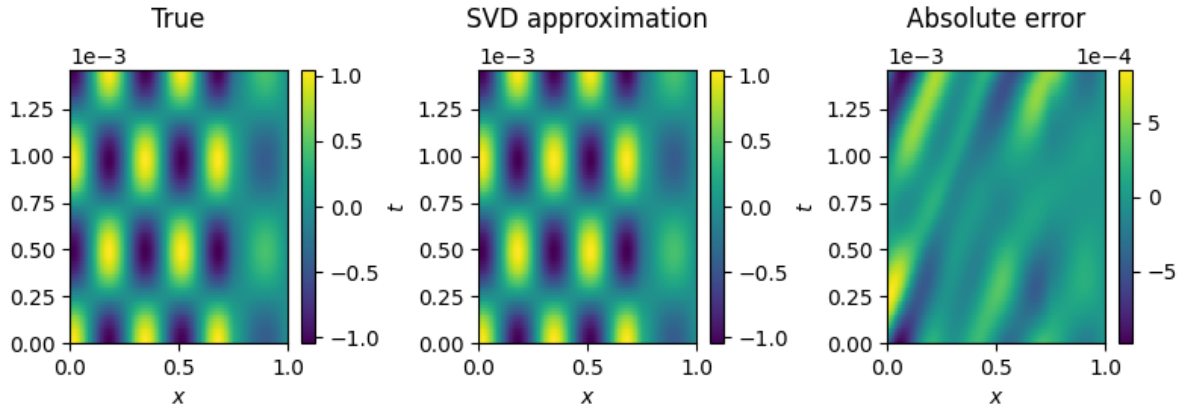


(c) Mixed models.

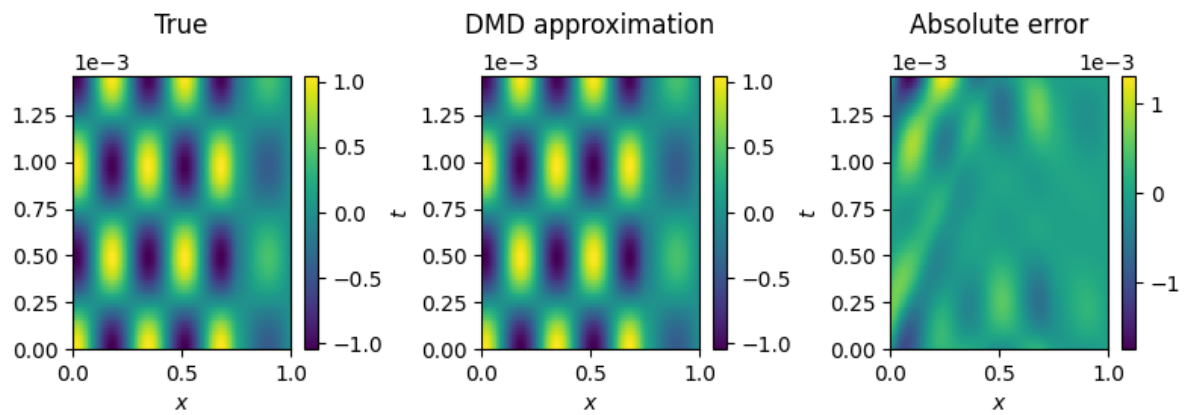
Figure 45: Mixed model reconstruction modeled by (P_1) .

8.7 Comparison to SVD

Finally, it seems reasonable to compare DMD to SVD, so that it can be determined how much of the success can be attributed to either of the methods. For starters it is important to understand that SVD runs within DMD, so DMD should be able to do anything SVD can. This includes of course reconstruction of periodic data, as seen in Fig. 46 or non-periodic data, as showcased in Fig. 47. In the harmonic case a truncation rank of $r = 2$ was chosen for both cases (see (43) for SVD and (48) for DMD), since this is the true number of modes of the exact solution. In the impulse reconstruction a SVD truncation rank of $r = 50$ was chosen and a DMD truncation rank of $r = 100$ was selected in order to show that in reconstructions where the true rank (k) is greater than the truncation rank (r), a SVD mode actually corresponds to two DMD modes, meaning that in order to obtain a comparable error only half of the SVD modes are necessary. This is due to the existence of dynamics in DMD ($e^{\Omega t} b$ in (54)), which introduces a new degree of freedom, so more data is needed to completely determine the state. In Fig. 46 the parameters used are those reflected in Tab. 4 and Tab. 5, adding a SVD truncation rank of 2, while for Fig. 47, the parameters are shown in Tab. 4 and Tab. 10 with SVD truncation rank of 50, as stated before.

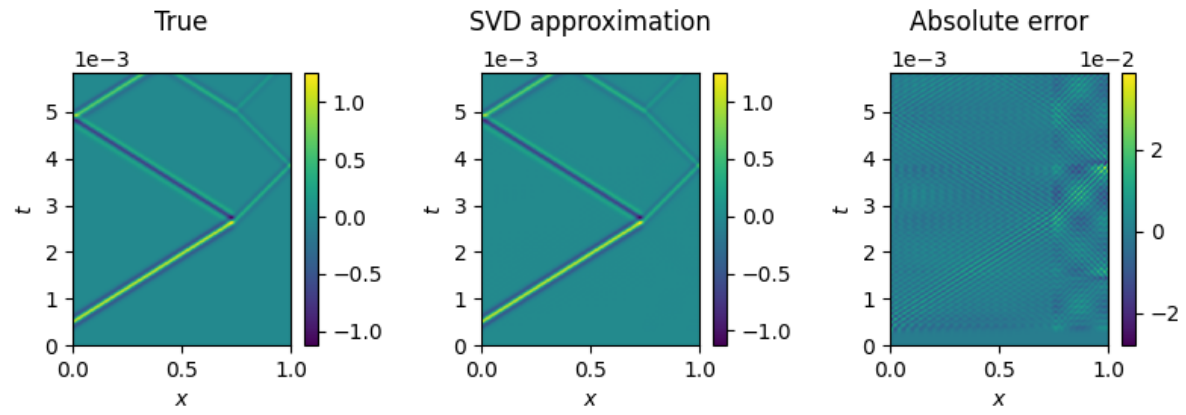


(a) SVD.



(b) DMD.

Figure 46: Reconstruction of periodic data modeled by (\mathcal{P}_3) .



(a) SVD.

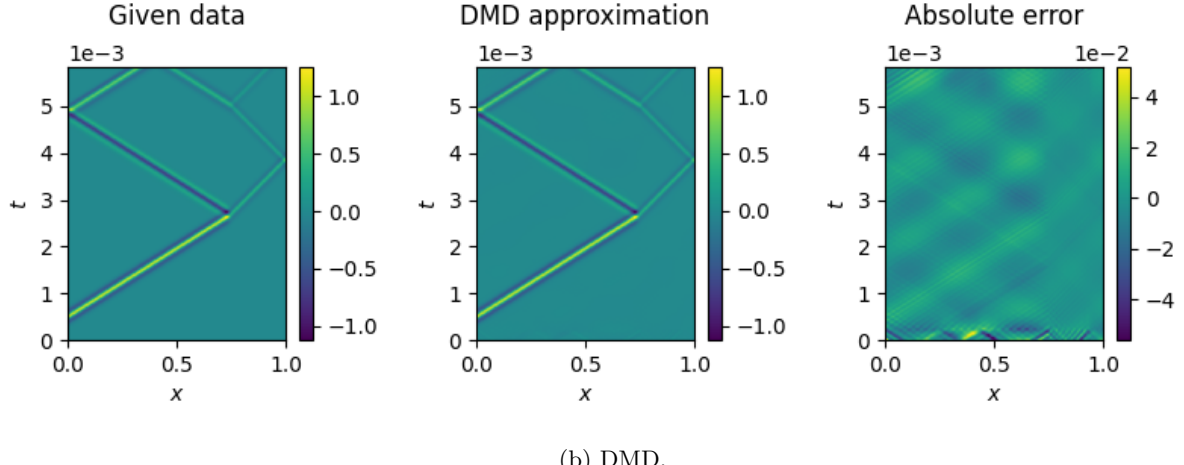


Figure 47: Reconstruction of non-periodic data modeled by (\mathcal{P}_3) .

When it comes to predictions however, there is no clear method in which SVD can directly make a prediction, since its aim is to reconstruct and extract modes, not to extend the dimensionality. For this reason, SVD is not a valid method for this project, since there is no need to reconstruct the available data, the interest of this project lies in predicting future behavior.

The closest thing that this project was able to achieve that resembles a dimensionality expansion using SVD involved calculating two SVDs, one on the data and one on a sample matrix of the goal dimensions. Then, the second was reconstructed using the data's modes. This implied that the dynamics from the sample matrix were kept, so the result did not resemble the target data. The results of that test can be seen in Fig. 48 Implementing methods of extrapolation in order to extend the dynamics beyond the given dimensions would result in a method that is very similar in function, if not identical, to DMD.

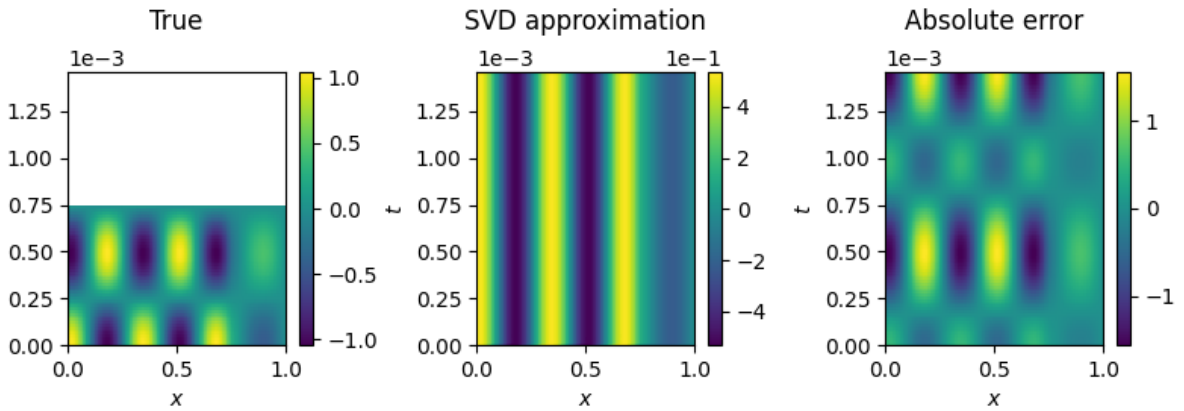


Figure 48: Predictions made by SVD using a sample matrix of ones (truncation rank of 50). Solution modeled by (\mathcal{P}_3) .

8.8 Shifted DMD

Rudimentary efforts were made trying to develop a method by which the data matrix of an impulse is transformed into a matrix in which the propagation path is aligned with the vertical. Had it been

successful it would have been possible to transform the data into the shifted space, perform DMD, and then transform it back in order to easily predict the future behavior of traveling waves, which would ideally work on non-periodic impulses. An example of one of the most basic (yet unsuccessful) cases is shown in Fig. 49. More information about this method can be found in [50] and [45]. The parameters used in the attempt of Fig. 49 correspond to those presented in Tab. 4 and Tab. 10.

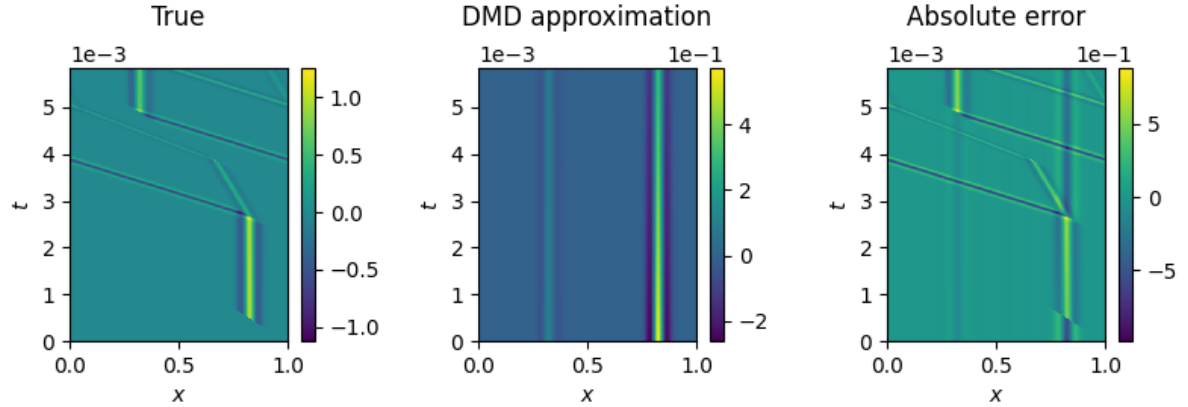


Figure 49: Shifted DMD attempt. The original data is that of Fig. 47.

9 Conclusions

In this project a number of acoustical models in the time domain that implement different materials with distinct characteristics were developed. These models are able to simulate acoustic propagation inside an impedance-Kundt tube. The project was started with a fluid model, and later a fluid-porous coupled model was added. At first the porous material used a rigid porous model, but it was later improved to a poro-elastic model. Most of the models have two variations that correspond with the physical configurations of a Kundt tube, one with a closed rigid boundary on the right, and one with a transparent boundary.

Each of the models have been validated. The first validation tested the capabilities and convergence of the numerical methods used (FEM and Newmark). Then, the fluid models were tested using d'Alembert's solution and the principle of virtual images, and both fluid and fluid-porous models (in its rigid variant) were tested against an exact harmonic solution. The poro-elastic model was tested against published data.

Then, applications of the DMD algorithm where explored, which allowed to make predictions from a reduced number of snapshots of the numerical simulation, which reduces the computational time significantly. In particular the findings include that DMD excels at predicting pure harmonic motion, reducing the simulation's computational time to an insignificant amount since only three snapshots are really necessary. With regards to non-harmonic periodic signals it seems that DMD is able to make predictions as long as a complete wave cycle is provided. Evidence was found that points to the fact that DMD, in its standard formulation or its generalized higher order form, HODMD, is ineffective in predicting non-periodic data.

There are a number of directions future work might head to, which include tasks that were not able to be completed due to time constraints, or new approaches to certain issues found. For starters, the use of DMD is most effective when the time required to run the simulation is high, and in no case this is more evident than in a high frequency approximation of poro-elastic dynamics, or directly in the case of the bare fluid-equivalent model, both of which include temporal convolutions that severely affect the execution time of the simulation.

Focusing on DMD, there exist a number of variations of the method, and while the focus of this project lied both in the standard version and in the higher order version, it is possible that other variations offer other advantages. For instance, MrDMD (multi-resolution DMD), which is able to better capture transient data and discontinuities, was lightly tested. No further exploration was performed because at this point its implementation in pyDMD lacked predictive capabilities, but the original formulation [28] allows it, and in fact, as stated in [1], the developers are working on it.

Another interesting approach would be to develop more intricate models and transformations in order to be able to apply a shifted DMD that would erase DMD's biggest flaw and allow it to make predictions about non-periodic impulse responses.

Finally, there are some interesting applications of this work. It has already been demonstrated that using DMD can be very advantageous when modeling 1D harmonic data. An extension of this work to higher dimensions can be critical, since simulation time increases dramatically when dimensionality is increased. With such an efficient model it makes it possible to execute parametric sweeps that were prohibitively expensive before in projects such as Nayak's. In the meantime, the 1D version can still be used to replace experimental testing in impedance-Kundt tubes or similar situations.

References

- [1] How do I use DMD for prediction/extrapolation? <https://github.com/mathLab/PyDMD/issues/63>
- [2] APMR: ACOUSTICAL POROUS MATERIAL RECIPES: "Acoustical" parameters. <https://apmr.matelys.com/Parameters/AcousticalParameters.html>
- [3] ARNOLD, N. D. ; LOGG, Anders: *Periodic table of the finite elements.* <https://sinews.siam.org/Details-Page/periodic-table-of-the-finite-elements>. Version: 2014
- [4] BATHE, Klaus-Jürgen: *Finite Element Procedures in Engineering Analysis.* Prentice Hall, Inc., 1982
- [5] BRUNTON, B. W. ; JOHNSON, L. A. ; OJEMANN, J. G. ; KUTZ, J. N.: Discovering dynamic patterns from infectious disease data using dynamic mode decomposition. In: *Journal of Neuroscience Methods* 258 (2016), S. 1–15
- [6] CARBAJO, J ; PRIETO, A ; RAMIS, J ; RÍO-MARTÍN, L: A non-parametric fluid-equivalent approach for the acoustic characterization of rigid porous materials. In: *Applied Mathematical Modelling* 76 (2019), S. 330–347
- [7] CHAMPOUX, Y. ; ALLARD, J.-F.: Dynamic tortuosity and bulk modulus in air-saturated porous media. In: *Journal of Applied Physics* 70 (1991), S. 1975–1979
- [8] CHUNG, J. Y. ; BLASER, D. A.: Transfer function method of measuring in-duct acoustic properties. I. Theory. In: *Acoustical Society of America Journal* 68 (1980), Nr. 3, S. 907–913. <http://dx.doi.org/10.1121/1.384778>. – DOI 10.1121/1.384778
- [9] CHUNG, J. Y. ; BLASER, D. A.: Transfer function method of measuring in-duct acoustic properties. II. Experiment. In: *The Journal of the Acoustical Society of America* 68 (1980), Nr. 3, S. 914–921. <http://dx.doi.org/10.1121/1.384779>. – DOI 10.1121/1.384779
- [10] COMSOL: *Multiphysics Encyclopedia: The Finite Element Method (FEM).* <https://www.comsol.com/multiphysics/finite-element-method>
- [11] D'ALEMBERT: Recherches sur la courbe que forme une corde tendue mise en vibration (Researches on the curve that a tense cord [string] forms [when] set into vibration). In: *Histoire de l'académie royale des sciences et belles lettres de Berlin* 3 (1747), S. 214–21
- [12] DAWSON, Scott T. M. ; HEMATI, Maziar S. ; WILLIAMS, Matthew O. ; ROWLEY, Clarence W.: Characterizing and correcting for the effect of sensor noise in the dynamic mode decomposition. In: *Experiments in Fluids* 57 (2016), Nr. 3, S. 1–19. <http://dx.doi.org/10.1007/s00348-016-2127-7>. – DOI 10.1007/s00348-016-2127-7
- [13] DEMO, Nicola ; TEZZELE, Marco ; ROZZA, Gianluigi: PyDMD: Python Dynamic Mode Decomposition. In: *The Journal of Open Source Software* 3 (2018), Nr. 22, S. 530. <http://dx.doi.org/10.21105/joss.00530>. – DOI 10.21105/joss.00530
- [14] ERICHSON, N. B. ; BRUNTON, S. L. ; KUTZ, J. N.: Compressed dynamic mode decomposition for real-time object detection. (2015)
- [15] ERICHSON, N. B. ; BRUNTON, Steven L. ; KUTZ, J. N.: Compressed dynamic mode decomposition for background modeling. In: *Journal of Real-Time Image Processing* 15 (2019), S. 1479–1492. <http://dx.doi.org/10.1007/s11554-016-0655-2>. – DOI 10.1007/s11554-016-0655-2
- [16] FAHY, F. J.: A Simple Method for Measuring Loudspeaker Cabinet Impedance. In: *Journal of the Audio Engineering Society* 41 (1993), Nr. 3, S. 154–156
- [17] FENICS PROJECT: *FEniCS Project.* <https://fenicsproject.org>

- [18] FUNG, K.-Y. ; JU, Hongbin: Broadband Time-Domain Impedance Models. In: *AIAA Journal* 39 (2001), Nr. 8, S. 1449–1454
- [19] FUNG, K.-Y. ; JU, Hongbin: Time-domain Impedance Boundary Conditions for Computational Acoustics and Aeroacoustics. In: *International Journal of Computational Fluid Dynamics* 18 (2004), Nr. 6, S. 503–511
- [20] GABARD, Gwénaël ; BRAMBLEY, Ed ; COSNEFROY, Matthias ; DAZEL, Olivier: Time-domain representation of acoustic impedance surfaces with flow, 2017. – LAUM, Université du Maine, Le Mans, France. Séminaire LMFA
- [21] GROSEK, J. ; KUTZ, J. N.: Dynamic mode decomposition for real-time background/foreground separation in video. (2014)
- [22] HOLMARC OPTO-MECHATRONICS PVT. LTD.: *Impedance Tube Apparatus*. https://holmarc.com/impedance_tube_apparatus_a.php
- [23] HOROSHENKOV, Kirill V.: A Review of Acoustical Methods for Porous Material Characterisation. In: *International Journal of Acoustics and Vibration* 22 (2017), Nr. 1, S. 92–103. <http://dx.doi.org/10.20855/ijav.2017.22.1455>. – DOI 10.20855/ijav.2017.22.1455
- [24] ITMATI: *Instituto Tecnológico de Matemática Industrial (ITMATI)*. <http://www.itmati.com/nosotros-0>
- [25] ITMATI: *Organización*. <http://www.itmati.com/organizaci\unhbox\voidb@x\bgroup\let\unhbox\voidb@x\setbox\@tempboxa\hbox{\global\mathchardef\accent@spacefactor\spacefactor}\accent19\egroup\spacefactor\accent@spacefactorn>
- [26] JOHNSON, L. D. ; KOPLIK, J. ; DASHEN, R.: Theory of dynamic permeability and tortuosity in fluid-saturated porous media. In: *Journal of Fluid Mechanics* 176 (1987), S. 379–402
- [27] JOLLIFFE, T. I.: *Principal Component Analysis*. Springer, 2002
- [28] KUTZ, J. N. ; FU, Xing ; BRUNTON, Steven L.: Multiresolution Dynamic Mode Decomposition. In: *SIAM Journal on Applied Dynamical Systems* 15 (2016), Nr. 2, S. 713–735. <http://dx.doi.org/10.1137/15M1023543>. – DOI 10.1137/15M1023543
- [29] KUTZ, Nathan J. ; BRUNTON, L. S. ; BRUNTON, W. B. ; PROCTOR, L. J.: *Dynamic mode decomposition: data-driven modeling of complex systems*. Society for Industrial and Applied Mathematics, 2016
- [30] LE CLAINCHE, Soledad ; VEGA, José M.: Higher Order Dynamic Mode Decomposition. In: *SIAM Journal on Applied Dynamical Systems* 16 (2017), Nr. 2, S. 882–925. <http://dx.doi.org/10.1137/15M1054924>. – DOI 10.1137/15M1054924
- [31] MAA, Dah-You: Potential of microperforated panel absorber. In: *Journal of Acoustical Society of America* 104 (1998), Nr. 5, S. 2861–2866
- [32] MICROFLOWN TECHNOLOGIES: *About us*. <https://www.microflown.com/about-us/>
- [33] MICROFLOWN TECHNOLOGIES: *Acoustic sensors & measuring solutions*. <https://www.microflown.com>
- [34] MICROFLOWN TECHNOLOGIES: *Sensors and probes*. <https://www.microflown.com/products/standard-probes/>

- [35] MOLINA-AIZ, Francisco ; FATNASSI, Hicham ; BOULARD, T. ; ROY, Jean-Claude ; VALERA, Diego: Comparison of finite element and finite volume methods for simulation of natural ventilation in greenhouses. In: *Computers and Electronics in Agriculture* 72 (2010), S. 69–86. <http://dx.doi.org/10.1016/j.compag.2010.03.002>. – DOI 10.1016/j.compag.2010.03.002
- [36] NEWMARK, Nathan M.: A method of computation for structural dynamics. In: *Journal of the Engineering Mechanics Division* 85 (1959), Nr. 3, S. 67–94
- [37] NOH, Gunwoo ; HAM, Seounghyun ; BATHE, Klaus-Jürgen: Performance of an implicit time integration scheme in the analysis of wave propagations. In: *Computers and Structures* 123 (2013), S. 93–105. <http://dx.doi.org/10.1016/j.compstruc.2013.02.006>. – DOI 10.1016/j.compstruc.2013.02.006
- [38] PANNETON, Raymond E. a.: Comments on the limp frame equivalent fluid model for porous media. In: *Acoustical Society of America* 122 (2007), Nr. 6, S. 217–222. <http://dx.doi.org/10.1121/1.2800895>. – DOI 10.1121/1.2800895
- [39] PRATHAP, Gangan: *Solid Mechanics and Its Applications*. Bd. 24: *The Finite Element Method in Structural Mechanics*. 1. Springer Netherlands, 1993. <http://dx.doi.org/10.1007/978-94-017-3319-9>. – ISBN 978-0-7923-2492-8
- [40] PROCTOR, Joshua L. ; BRUNTON, Steven L. ; KUTZ, J. N.: Dynamic mode decomposition with control. In: *SIAM Journal on Applied Dynamical Systems* 15 (2016), Nr. 1, S. 142–161. <http://dx.doi.org/10.1137/15M1013857>. – DOI 10.1137/15M1013857
- [41] PROCTOR, L. ; ECKHOFF, P. A.: Discovering dynamic patterns from infectious disease data using dynamic mode decomposition. In: *International Health* 2 (2015), Nr. 7, S. 139–145
- [42] PYDMD: *Python Dynamic Mode Decomposition*. <https://github.com/mathLab/PyDMD>
- [43] PYDMD: *Welcome to PyDMD's documentation!* <https://mathlab.github.io/PyDMD/build/html/index.html>
- [44] QUARTERONI, Alfio ; SACCO, Riccardo ; SALERI, Fausto: *Numerical Mathematics*. Springer, 1991
- [45] REISS, J. ; SCHULZE, P. ; SESTERHENN, J. ; MEHRMANN, V.: The shifted proper orthogonal decomposition: A mode decomposition for multiple transport phenomena. In: *SIAM Journal on Scientific Computing* 40 (2018), Nr. 3, S. A1322–A1344. <http://dx.doi.org/10.1137/17M1140571>. – DOI 10.1137/17M1140571
- [46] ROMSOC: *ROMSOC - Reduced Order Modelling, Simulation and Optimization of Coupled Systems*. <https://www.romsoc.eu>
- [47] SCHMID, Peter: Dynamic mode decomposition of numerical and experimental data. In: *Journal of Fluid Mechanics, Cambridge University Press (CUP)* 656 (2010), S. 5–28. <http://dx.doi.org/10.1017/s0022112010001217>. – DOI 10.1017/s0022112010001217
- [48] SCHURER, Hans ; ANNEMA, Peter ; DE BREE, Hans-Elias ; SLUMP, Cornelis H. ; HERRMANN, Otto E.: Comparison of Two Methods for Measurement of Horn Input Impedance, 1996, S. 1–10. – 100th Convention of the Audio Engineering Society 1996, AES 1996 ; Conference date: 11-05-1996 Through 14-05-1996
- [49] SCIKIT-LEARN: *sklearn.decomposition.TruncatedSVD*. <https://scikit-learn.org/stable/modules/generated/sklearn.decomposition.TruncatedSVD.html>
- [50] SESTERHENN, Jörn ; SHAHIRPOUR, Amir: *A Characteristic Dynamic Mode Decomposition*. 2016. – arXiv:1603.02539 [physics.flu-dyn]

- [51] TU, J. H. ; ROWLEY, C. W. ; KUTZ, J. N. ; SHANG, J. K.: Spectral analysis of fluid flows using sub-Nyquist rate PIV data. In: *Experiments in Fluids* 55 (2014), Nr. 9, S. 1–13
- [52] UMNOVA, Olga ; TURO, Diego: Time domain formulation of the equivalent fluid model for rigid porous media. In: *The Journal of the Acoustical Society of America* 125 (2009), Nr. 4, S. 1860–1863. <http://dx.doi.org/10.1121/1.3082123>. – DOI 10.1121/1.3082123
- [53] VAN DER EERDEN, F.J.M. ; DE BREE, H.E. ; TIJDENMAN, H.: Experiments with a new acoustic particle velocity sensor in an impedance tube. In: *Sensors and actuators. A: Physical* 69 (1998), Nr. 2, S. 126–133. [http://dx.doi.org/10.1016/S0924-4247\(98\)00070-3](http://dx.doi.org/10.1016/S0924-4247(98)00070-3). – DOI 10.1016/S0924-4247(98)00070-3. – ISSN 0924–4247
- [54] VORONINA, N.: Acoustic Properties of Synthetic Films. In: *Applied Acoustics* 49 (1996), Nr. 2, S. 127–140
- [55] WILSON, D. K. ; COLLIER, Sandra L. ; OSTASHEV, Vladimir E. ; ALDRIDGE, David F. ; SYMONS, Neill P. ; MARLIN, David H.: Time-Domain Modeling of the Acoustic Impedance of Porous Surfaces. In: *Acta Acustica United With Acustica* 92 (2006), S. 965–975
- [56] ZHAO, Jing ; BAO, Ming ; WANG, Xiaolin ; LEE, Hyojin ; SAKAMOTO, Shinichi: An equivalent fluid model based finite-difference time-domain algorithm for sound propagation in porous material with rigid frame. In: *The Journal of the Acoustical Society of America* 143 (2018), Nr. 1, S. 130–138. <http://dx.doi.org/10.1121/1.5020268>. – DOI 10.1121/1.5020268
- [57] ZIENKIEWICZ, O.C. ; TAYLOR, R. ; FOX, D.: The Finite Element Method for Solid and Structural Mechanics. (2005), S. 85617–85634
- [58] ZIENKIEWICZ, O.C. ; TAYLOR, R.L. ; NITHIARASU, P.: *The Finite Element Method for Fluid Dynamics*. 7. Oxford : Butterworth-Heinemann, 2014. <http://dx.doi.org/10.1016/B978-1-85617-635-4.00018-2>. – ISBN 978-1-85617-635-4